DOCTORAL DISSERTATION

THE EVOLUTION OF GALAXIES AND THE LARGE-SCALE STRUCTURE IN THE EARLY UNIVERSE TRACED BY DAMPED LYα ABSORPTION SYSTEMS

KAZUYUKI OGURA

GRADUATE SCHOOL OF SCIENCE AND ENGINEERING
EHIME UNIVERSITY

2017

ABSTRACT

The formation and evolution of galaxies are important topics in the modern astrophysics. Especially, the process that cold gas is converted to stars in galaxies is important to understand the complete picture of the galaxy evolution. For this purpose, we focus on strong Lyα absorbers ($\log N_{\rm HI} \geq 20.0$ cm^{-2}) such as damped Lyα absorption systems (DLAs). The DLA is a key population to understand the early phase of the galaxy evolution in the following respects: (1) DLAs provide a powerful tool to investigate the nature of the cold gas at high-z since they trace the intervening gas along the sightline to quasars and can be detected as a strong Lyα absorption line on quasar spectra regardless of the luminosity of their stellar component, and (2) DLAs dominate the neutral-gas content in a wide redshift range and they are thought to be gas reservoirs for the star-formation in the high-z Universe. Although the DLA is such an important population, their nature is still under debate. This is because galaxy counterparts of DLAs are difficult to observe due to their faintness. To date only 13 galaxy counterparts of DLAs at $z > 2$ have been spectroscopically identified. Even at $z < 1$, the number of identified DLA counterparts are less than 100. Therefore the statistical study to investigate the nature of DLAs is incomplete, and accordingly the relationship between DLAs and galaxies is still unclear. The identifications of DLA counterparts are gradually progressing thanks to recent observations using 8–10 m class telescopes, such as the Subaru telescope. In this dissertation, we report the study for the relationship between DLAs and young galaxies to understand the early phase of the galaxy evolution.

To investigate the physical relationship between DLAs and young star-forming galaxies at high redshift such as Lyα emitters (LAEs), we focus on the region where multiple DLAs distribute within a narrow area. Using a catalog of Lyα absorbers with $\log N_{\rm HI} \geq 20.0$ cm^{-2} based on the Baryon Oscillation Spectroscopic Survey (BOSS), we found six fields where three or more absorbers are concentrated within a (50 Mpc)^3 cubic box in the comoving scale. Among them, we focus on the J1230+34 field, where 2 DLAs and 2 sub-DLAs at $z \sim 2.3$ present. We have conducted narrow-band imaging observations of LAEs in this field with Subaru/Suprime-Cam using a custom-made filter, $NB400$ ($\lambda_{\rm c} = 4003$ Å and FWHM$= 92$ Å). These observations yield a sample of 149 LAEs in the J1230+34 field. Based on this sample, we investigate physical properties of LAEs. In the entire target field with the scale of $\sim$50 Mpc, we have found no differences between the obtained Lyα luminosity function and those in the blank fields at similar redshifts. We also compare the frequency distribution of the Lyα rest-frame equivalent width (EW_0) in the target field and other fields at similar redshift including both overdensity

region and blank field, but find no differences. On the other hand, in the small scale ($\sim$10 Mpc), we have found a possible overdensity of LAEs around a DLA with the highest H I column density ($\log N_{\rm HI} = 21.08$ cm^{-2}) in the target field while there are no density excess around the other absorbers with a lower $N_{\rm HI}$. Based on these results, we propose two possible scenarios for the absorber-concentrated regions as follows. (1) The J1230+34 field harbors many young galaxies intrinsically. The reason why we have not found overdensity of LAEs around three among four absorbers in the J1230+34 field is that the Lyα emission is suppressed by the resonant scattering since this region harbors a large amount of the neutral gas. (2) There are not so many galaxies in the J1230+34 field. Since the neutral gas is not converted to stars but goes through H_2 molecules, a large fraction of gas in the J1230+34 field may not have been converted to stars. Both of these two scenarios suggest that the absorber-concentrated region may correspond to the birthplace of galaxies and thus the J1230+34 field is a good target for coming deep surveys to investigate the early phase of the galaxy evolution.

Thanks to the large sample of BOSS DLAs and large telescopes such as the Subaru telescope, we are gradually understanding the relation between DLAs and galaxies. Ongoing and incoming spectroscopic surveys such as extended BOSS and surveys with Prime Focus Spectrograph on the Subaru telescope, will dramatically increase the number of high-z quasars. This will enable us to search for absorber-concentrated regions, important regions to understand the early stage of galaxy evolution, more effectively. This dissertation work provides useful methods and interesting target fields for such future observation.

CONTENTS

CHAPTER 1

GENERAL INTRODUCTION

Investigating the formation and evolution of galaxies is one of the hottest topics in the modern astrophysics. Now we know that galaxies do not distribute uniformly but the distribution of galaxies shows various structures at various spatial scales. For example, in the present-day Universe, there are galaxy clusters where many galaxies concentrate and also voids where no galaxies exist. So far, N-body simulations have been revealed the formation of such a large-scale structure (LLS) of the Universe caused by the gravitational effect. The structure formation is led by dark matters (DMs) through the gravitational interactions and galaxies evolve in halos of DMs. On the other hand, the baryonic evolution of galaxies has not been well understood. In particular, we do not know much about the very early stage of the evolution of galaxies, in which gas is being converted to stars. This is because we have to access the very distant (high redshift) Universe where galaxies are extremely faint, that prevents us from investigating the early stage of the galaxy evolution. Recently, 8–10 m class telescopes, such as the Subaru telescope, enable us to access the early Universe. In this chapter, we review the early stage of the structure formation of Universe and the galaxy evolution. Especially, we focus on gas-rich young systems, the damped Lyα absorption system (DLA) and the Lyα emitter (LAE), that are key populations to understand the early phase of the baryonic evolution of galaxies.

1.1 The evolution of galaxies and the structure formation of the Universe

Since the galaxy is the basic component of the Universe, it is crucially important to study the formation and evolution of galaxies for understanding the Universe. Galaxies consist of DMs and baryons (stars and gas). A number of theoretical studies have revealed the formation of the LSS and now the Λ cold dark matter (ΛCDM) model becomes the standard model of cosmology (e.g., Ostriker & Steinhardt, 1995; Im et al., 1997; Schmidt et al., 1998; Perlmutter et al., 1999; Eisenstein et al., 2005; Frenk & White, 2012). According to the ΛCDM cosmology, galaxies form and evolve in the gravitational field of the CDM. The density fluctuations in the early Universe mature into DM halos. Baryons are gathered into DM halos through gravitational processes and then collapse to form galaxies as the result of the radiation cooling. Springel et al.

(2005) simulated the structure formation and showed the growth process of the DM structure (see also Gao et al., 2005; Springel et al., 2006; Boylan-Kolchin et al., 2009; Ishiyama et al., 2015). As for the observational study, Massey et al. (2007) revealed the three-dimensional distribution of DMs in the COSMOS field by analyzing the gravitational lensing effects for galaxies (see also Simon et al., 2009; Amara et al., 2012; Van Waerbeke et al., 2013; Natarajan et al., 2017). The observed distribution of DMs shows the filamentary structure and consistent with predictions of theoretical studies. Since accurate measurements of redshift and analysis of gravitational lensing effect are required to obtain such 3D maps of DMs, it is still not so easy to compare spatial distributions of galaxies and DMs. On the other hand, the two-point correlation function (autocorrelation of galaxies) is often used to investigate the relation between galaxies and DMs (e.g., Totsuji & Kihara, 1969; Peebles, 1980; Hawkins et al., 2003; Adelberger et al., 2005; Zehavi et al., 2011; Beutler et al., 2013; Sołtan & Chodorowski, 2015). Based on the two-point correlation function, the strength of clustering of galaxies can be investigated and the mass of DM halos hosting various populations of galaxies can be restricted.

To understand the baryonic evolution of galaxies, the star-formation history in the cosmological timescale has been studied. Steidel et al. (1995) constructed the selection method of galaxies at high redshift based on the observed colors of galaxies (see also Steidel & Hamilton, 1992). Steidel et al. (1995) focused on the break feature in the spectral energy distribution (SED) of galaxies. Specifically, in the wavelength range shorter than the Lyman limit (912 Å in the rest frame), photons are almost completely absorbed by neutral hydrogen. Thus the flux of the continuum emission from galaxies reaches to zero at $\lambda_{\rm rest} \leq$912 Å. Furthermore, radiation in the wavelength range of $912 \leq \lambda_{\rm rest} \leq 1216$ Å is also absorbed by intervening absorbers such as Lyα forests. Therefore high-z galaxies are undetectable in the rest frame wavelength range of $\lambda_{\rm rest} \leq$1216 Å. For example, galaxies at $z = 3$ is detected in the g-band while they "dropout" in the u-band (see Figure 1.1). This selection method is called the Lyman break technique, and galaxies selected by this techniqu are called Lyman break galaxies (LBGs). The Lyman break technic is used to select star-forming galaxies in a wide redshift range of $3 \lesssim z \lesssim 9$. On the other hand, galaxies at ~ 2 show no break features in the optical wavelength range (see Figure 1.1). Steidel et al. (2004) constructed the selection method of $z \sim$2 galaxies without any breaks, so-called the BMBX selection, by utilizing a $U - G$ versus $G - R$ color-color diagram. In addition to these selections based on the spectral features of continuum emission, lines such as the $Ly\alpha$ emission are also useful to select high-z galaxies (see Section 1.4 for more details about the Lyα emitters [LAEs]). Since photometric observations can reach to significant depth with the shorter time exposure compared to spectroscopic observations, the photometric selection is useful to construct a large sample of star-forming galaxies over a wide redshift range. Indeed various surveys for star-forming galaxies have been conducted over a wide redshift range (e.g., Madau et al., 1996; Steidel et al., 2003; Giavalisco et al., 2004; Hopkins & Beacom, 2006; Bouwens et al., 2011, 2015; Madau & Dickinson, 2014). Based on such samples, we can investigate the cosmic star-formation history by measuring star formation rate (SFR) of galaxies at each redshift.

Here the SFR is inferred by utilizing the radiation from massive stars, such as O or B

type stars, in galaxies (e.g., Kennicutt, 1998; Kennicutt & Evans, 2012). Since O-stars stably emit the ultra violet (UV) light, the UV luminosity is a good tracer for the SFR. When dusts in galaxies absorb the UV radiation, they re-radiate the infrared (IR) light. Then, the IR luminosity is also a good tracer. The recombination lines of hydrogen (e.g., Hα, Lyα) and forbidden lines (e.g., [O II]λ3727, [O III]λ5007) are also used for estimating the SFR because the UV radiation from O or B stars ionizes the gas. The SFRs inferred by the UV continuum, IR, Hα emission-line, and [O II] emission-line are quantitatively derived through the following equations (Kennicutt, 1998):

$$SFR\ (M_\odot\ \mathrm{yr}^{-1}) = 1.4\times10^{-28} L_{\mathrm{UV}}(\mathrm{erg\ s}^{-1}\ \mathrm{Hz}^{-1}) \tag{1.1}$$

$$SFR\ (M_\odot\ \mathrm{yr}^{-1}) = 4.5\times10^{-44} L_{\mathrm{IR}}(\mathrm{erg\ s}^{-1}) \tag{1.2}$$

$$SFR\ (M_\odot\ \mathrm{yr}^{-1}) = 7.9\times10^{-42} L_{\mathrm{H}\alpha}(\mathrm{erg\ s}^{-1}) \tag{1.3}$$

$$SFR\ (M_\odot\ \mathrm{yr}^{-1}) = 1.4\times10^{-41} L_{[\mathrm{OII}]}(\mathrm{erg\ s}^{-1}). \tag{1.4}$$

The redshift evolution of the cosmic star-formation rate density (SFRD; SFR per unit volume) has been inferred by rest-frame far-UV (FUV) and IR surveys. The SFRD against the redshift, $\psi(z)$, is fitted by

$$\psi(z) = 0.015\frac{(1+z)^{2.7}}{1+[(1+z)/2.9]^{5.6}}\ M_\odot\ \mathrm{yr}^{-1}\ \mathrm{Mpc}^{-3} \tag{1.5}$$

(Madau & Dickinson, 2014). From $z\sim8$ to $z\sim7$, the SFRD rises as $\psi(z)\propto(1+z)^{-2.9}$ and reaches the peak at ~2. Then, it gradually declines as $\psi(z)\propto(1+z)^{2.7}$ from $z\sim2$ to $z\sim0$ (Madau & Dickinson, 2014).

On the other hand, the evolution of the gas is less understood relative to the stellar component and DMs. Since stars form from molecular clouds which are dominated by molecular hydrogen, H_2, it is important to understand the evolution of H_2 in galaxies. Note that, the cold neutral gas, which is the precursor of molecular clouds, is also important for understanding the early phase of the galaxy evolution. We describe more details ofthe neutral gas in Section 1.3 by focusing on the quasar absorption-line systems. To trace the molecular gas, the carbon monoxide (CO), the second most abundant molecular, is generally used because H_2 is difficult to observe in emission. The H_2 column density (N_{H_2}) and the mass of the molecular gas (M_{mol}) are then estimated by assuming the "CO-to-H_2 conversion factor" (e.g., Bolatto et al., 2013) as follow:

$$N_{\mathrm{H}_2}\ (\mathrm{cm}^{-2}) = X_{\mathrm{CO}} W(^{12}\mathrm{C}^{16}\mathrm{O}J=1\rightarrow0) \tag{1.6}$$

$$M_{\mathrm{mol}}\ (M_\odot) = \alpha_{\mathrm{CO}} L_{\mathrm{CO}}, \tag{1.7}$$

where $W(^{12}\mathrm{C}^{16}\mathrm{O}J=1\rightarrow0)$ (K km s^{-1}) is the integrated line intensity and L_{CO} (K km s^{-1} pc^2) is the CO luminosity, respectively. Both of X_{CO} and α_{CO} are the conversion factors. In the case of $X_{\mathrm{CO}} = 2\times10^{20}$ cm^{-2}(km s^{-1})$^{-1}$, the value of α_{CO} is 4.3 $M_\odot$ (K km s^{-1})$^{-1}$. Given the integrated flux density, $S_{\mathrm{CO}}\Delta v$, L_{CO} (Jy km s^{-1}) is denoted by

$$L_{\mathrm{CO}} = 2453\frac{S_{\mathrm{CO}}\Delta v\ d_{\mathrm{L}}^2}{1+z}, \tag{1.8}$$

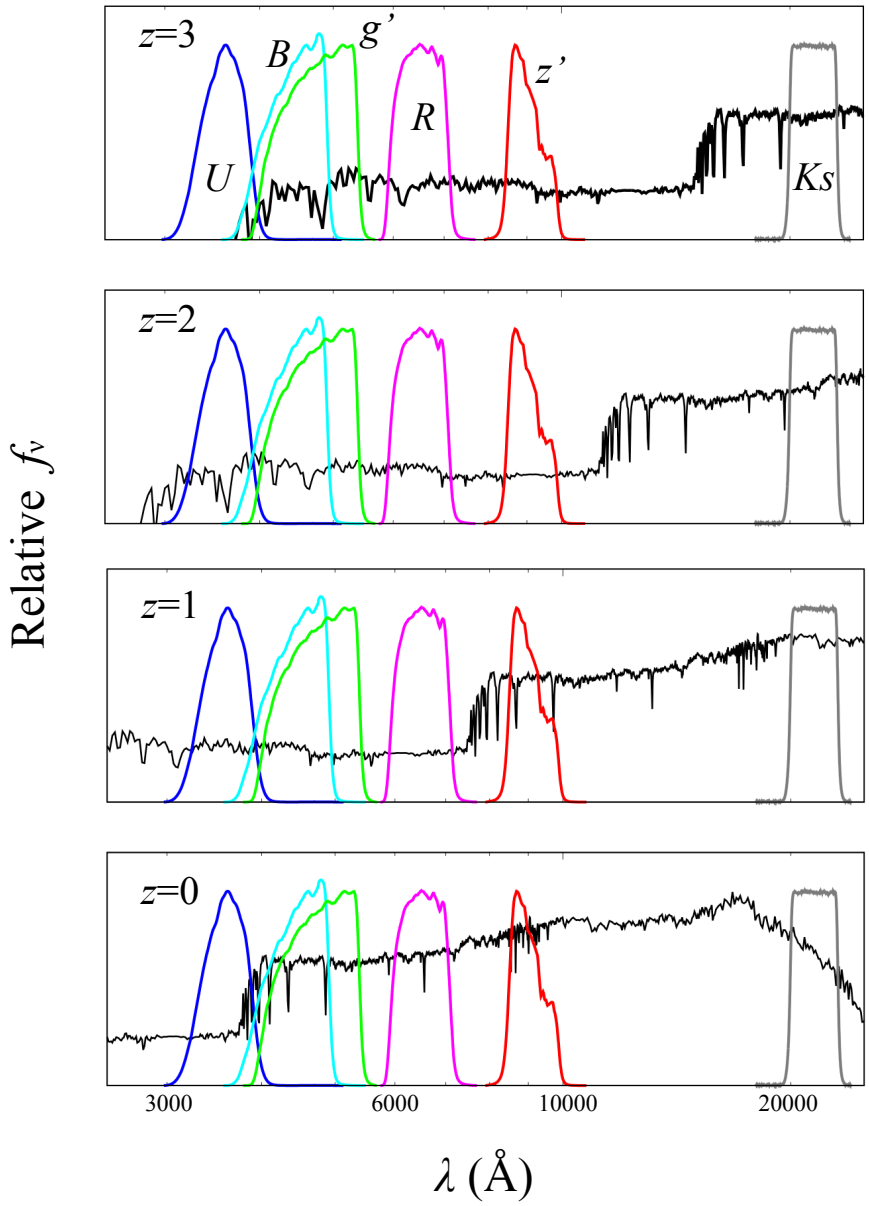

Fig. 1.1: The model SED of the star-forming galaxy at various redshift. The SED is calculated using the model by Bruzual & Charlot (2003) assuming a constant-SFR model with the Salpeter IMF, $SFR = 1\ M_\odot\ \mathrm{yr}^{-1}$ and the solar metallicity. We show some filters of various instrument on the Subaru telescope used for selecting galaxies: the U-band of the Faint Object Camera and Spectrograph (FOCAS; Kashikawa et al., 2000; Yoshida et al., 2000), B, g', R, and z'-bands of Suprime-Cam (Miyazaki et al., 2002), and the Ks-band of Multi-Object InfraRed Camera and Spectrograph (MOIRCS; Ichikawa et al., 2006; Suzuki et al., 2008).

where $d_{\rm L}$ (Mpc) is the luminosity distance. Thus Equation 1.6 can be written by using $X_{\rm CO}$ as follows,

$$M_{\rm mol} = 1.05 \times 10^4 \left(\frac{X_{\rm CO}}{2 \times 10^{20} \frac{\rm cm^{-2}}{\rm K\ km\ s^{-1}}} \right) \frac{S_{\rm CO} \Delta v\ d_{\rm L}^2}{(1+z)}. \quad 1.9$$

The value of $X_{\rm CO}$ is different depending on environments. For example, $X_{\rm CO} = 2 \times 10^{20}$ cm^{-2} (km s^{-1})$^{-1}$ has been suggested for the Milky Way disk (see Bolatto et al., 2013, in detail). Based on the radio observations of CO line, the gas fractions, $f_{\rm gas} = M_{\rm gas}/M_{\rm star}$, in galaxies at high-$z$ have been studied (e.g., Daddi et al., 2010; Tacconi et al., 2010; Riechers et al., 2010; Magnelli et al., 2012; Troncoso et al., 2014). Although the scatter is large, it is suggested that the gas fraction is larger at higher redshifts (e.g., Popping et al., 2012, 2015; Carilli & Walter, 2013). At $z \sim 0$, the mean value of $f_{\rm gas}$ is ~ 0.1 and increase to ~ 1 at $z > 1.5$. This trend can be fitted by $f_{\rm gas} \sim 0.1 \times (1+z)^2$ (e.g., Geach et al., 2011; Magdis et al., 2012). It is important to investigate the connection of stellar and cold gaseous components in high-z galaxies to understand the early phase of the galaxy evolution.

1.2 Galaxy protoclusters

As described in Section 1.1, DMs play important roles in the galaxy formation. Since galaxies tend to concentrate to density peaks of DMs, galaxy clusters are fundamental component of the LSS and thus they are good tracers to study the LSS. Indeed, galaxy clusters in the local Universe are located at the intersections of filament structures which correspond to densest density peaks of DMs (e.g., de Lapparent et al., 1986). To understand the early phase of the galaxy evolution and the structure formation of the Universe, it is important to investigate various properties of high-z galaxies as a function of the environment.

Progenitors of present-day galaxy clusters are sometimes called "protoclusters" or "overdensity regions". Currently, the definition of the protocluster is not well established, and the adopted definition depends on researchers. A simple and straightforward definition of the protocluster is that the structures that will collapse into clusters with $M \geq 10^{14}\ M_\odot$ (i.e., virialized systems) at $z \geq 0$ (Overzier, 2016). As for the size of protocluster, Muldrew et al. (2015) show that $\sim$90% of the mass in protoclusters extent within ~ 50 Mpc in the comoving scale at $z \sim 2$ based on the combination of the Millennium Simulation (Springel, 2005) and a semi-analytic model. This is consistent with the observed size of protclusters at $z > 2$ (e.g, Hayashino et al., 2004; Prescott et al., 2008; Chiang et al., 2013; Lee et al., 2014; Franck & McGaugh, 2016a,b).

Properties of galaxies in galaxy clusters have been well studied in the local Universe. Now it is known that galaxies in clusters have different properties from field galaxies. Specifically, galaxies in clusters at low-z tend to have lower SFR, red color, and early-type morphologies compared to field galaxies (e.g., Dressler, 1980; Butcher & Oemler, 1984; Balogh et al., 1998; Kauffmann et al., 2004). At higher redshift ($z > 1$), some studies show that galaxies in high-density environments show higher SFR than galaxies in the blank fields (e.g., Tran et al., 2010;

Popesso et al., 2011; Brodwin et al., 2013). At $z > 2$, young star-forming galaxies seem to be dominant in the most overdensity regions (e.g., Toshikawa et al., 2016). Thus star-forming galaxies such as LBGs and LAEs are used to search for high-z overdensity regions (e.g., Steidel et al., 1998; Kurk et al., 2000; Shimasaku et al., 2003; Miley et al., 2004; Ouchi et al., 2005; Overzier et al., 2006; Prescott et al., 2008; Utsumi et al., 2010; Kuiper et al., 2011; Toshikawa et al., 2012, 2016). To search for high-z overdensity regions, massive objects such as radio galaxies or quasars have been regarded as good tracers since they are thought to be laid in massive DM halos. In fact, various searches for high-z protocluster by focusing on radio galaxies and quasars as tracers have been successful (e.g., Miley et al., 2004; Venemans et al., 2007; Kashikawa et al., 2007; Mawatari et al., 2012; Wylezalek et al., 2013; Adams et al., 2015; Hennawi et al., 2015; Onoue et al., 2017, but see also Uchiyama et al., 2017).

A problem in high-z protocluster studies is that protoclusters around radio galaxies and quasars may be biased. Due to the strong radiation from quasars or strong jet from radio galaxies, star-formation in galaxies may be suppressed (e.g., Barkana & Loeb, 1999; Kashikawa et al., 2007). On the other hand, some protoclusters without radio galaxies and quasars have been also found (e.g., Steidel et al., 1998; Shimasaku et al., 2003; Ouchi et al., 2005; Lemaux et al., 2009). These protoclusters have been discovered serendipitously in random fields (fields without any tracers) through wide-field surveys. Recently, systematic surveys of protoclusters have been conducted in random fields (e.g., Toshikawa et al., 2012, 2016; Franck & McGaugh, 2016a,b; Uchiyama et al., 2017; Lemaux et al., 2017). In many cases of protocluster surveys, wide-field imaging surveys are conducted to investigate the spatial distribution of galaxies at first. Then candidates of protocluters are selected and confirmed by spectroscopic follow-up observations. Uchiyama et al. (2017) reported that only few quasars out to $>$150 quasars reside in protoclusters found in the recent survey with Subaru/Hyper Suprime-Cam (HSC), suggesting that quasars are not good tracers for protoclusters (see also Bañados et al., 2013; Mazzucchelli et al., 2017). Furthermore, it should be noted that such high-z over-density regions have been identified through the stellar emission from galaxies or the line emission from gas ionized by massive stars in galaxies. This means that we need a plenty amount of stars for recognizing such protoclusters. However, especially in the high-z Universe, not all galaxies necessarily have enough stars that make the galaxies observable for us. As described in Section 1.1, a large fraction of baryons in galaxies could be in the gas-phase at high-z Universe, simply because stars had not yet been formed from gas. We are possibly missing high-z protoclusters if the most of baryons in those systems are still in the gas-phase. Thus we have to focus also on gas-rich systems to understand the early stage of the evolution of galaxies and the LSS.

1.3 Damped Lyα absorption systems

To investigate systems which have large amount of gas, the quasar absorption-line system is a powerful tool. Quasar absorption-line systems are intervening gas along the line-of-sight to quasars. Since they are recognized as absorption lines on quasar spectra regardless of their luminosity of the stellar emission, we can investigate the nature of gas even in high-z galaxies

without enough amount of stars by focusing on the absorbers. Figure 1.2 shows a schematic picture of quasar absorption-line systems. An example of a quasar spectrum with a DLA is shown in Figure 1.3. Note that, not only quasars but also gamma-ray burst (e.g., Jensen et al., 2001; Hjorth et al., 2003; Jakobsson et al., 2004; Vreeswijk et al., 2004; Watson et al., 2006; Toy et al., 2016) and galaxies (e.g., Cooke & O'Meara, 2015; Mawatari et al., 2016) could be also background sources of such absorber.

Lyα absorbers are classified to three classes based on the H I column density as follows,

- $N_{\rm HI} < 10^{17}$ cm^{-2}: Lyα forests
- $10^{17} < N_{\rm HI} < 2 \times 10^{20}$ cm^{-2}: Lyman limit systems (LLSs)
- $N_{\rm HI} > 2 \times 10^{20}$ cm^{-2}: DLAs

In addition to these classes, Péroux et al. (2003) defined the sub-DLA as the absorber with $10^{19} < N_{\rm HI} < 2 \times 10^{20}$ cm^{-2}. The H I column of $N_{\rm HI} = 10^{17}$ cm^{-2} corresponds to the unity optical depth at the Lyman limit. Thus, the Lyα forest is optically thin while other three classes are optically thick at their Lyman limit. The most significant difference between DLAs and LLSs is the neutrality of the H I content in these systems (e.g., Wolfe et al., 2005). Hydrogen is mainly neutral in the DLAs, while it is mostly ionized in LLSs and Lyα forests. Since stars form from cold molecular gas, the systems with large amount of neutral gas (i.e. DLAs) are crucially important to understand the early stage of the galaxy evolution. Note that, DLAs dominate the neutral-gas content of the Universe in a wide redshift range (e.g., Storrie-Lombardi & Wolfe, 2000; Wolfire et al., 2003; O'Meara et al., 2007), and thus they are thought to be gas reservoirs for the star-formation in the high-z Universe.

DLAs are characterized by their absorption-line profile. Generally the absorption profile is naturally broadened since the lifetime of the upper energy state of the corresponding transition is limited. In addition, the absorption profile is also broadened by the Doppler effect due to the random motion of atoms. Convoluting these broadening effect, the profile of the absorption line is described by the Voigt profile (e.g., Mihalas, 1978). In the case of the Doppler broadening, the profile falls off from the central frequency, ν_0, as $\exp[-(\Delta\nu/\Delta\nu_{\rm D})^{-2}]$. Here $\Delta\nu = |\nu - \nu_0|$ and $\Delta\nu_{\rm D} = \sqrt{2}\sigma_\nu \nu_0/c$, where σ_ν is the velocity dispersion of atoms when we assume the Gaussian velocity distribution. As for the case of the natural broadening, the profile falls off as $\Delta\nu^{-2}$. The naturally broadened profile is also called as the "damped" profile. If the $\Delta\nu$ is sufficiently large, the probability for the damped profile exceeds that for the Doppler profile. The frequency (or wavelength) range where the damped profile dominates the Doppler profile is called as the "damped wing". When the H I column density is sufficiently high ($N_{\rm H\,I} > 10^{19}$ cm^{-2}), the optical depth of Lyα becomes unity in the damped wing. The threshold of $N_{\rm H\,I}$ for

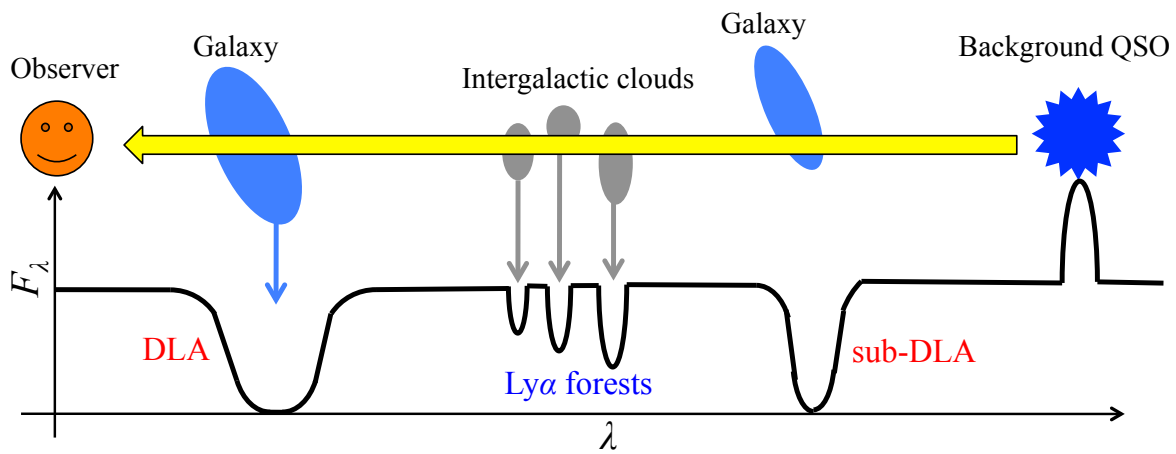

Fig. 1.2: The schematic picture of quasar absorption systems. The foreground gas absorbs the light from background quasars and make absorption lines. Lyα forests are optically thin absorbers such as intergalactic clouds. Although the origin of DLAs and sub-DLAs are still under the debate, their high $N_{\rm HI}$ is comparable to that of disk galaxies.

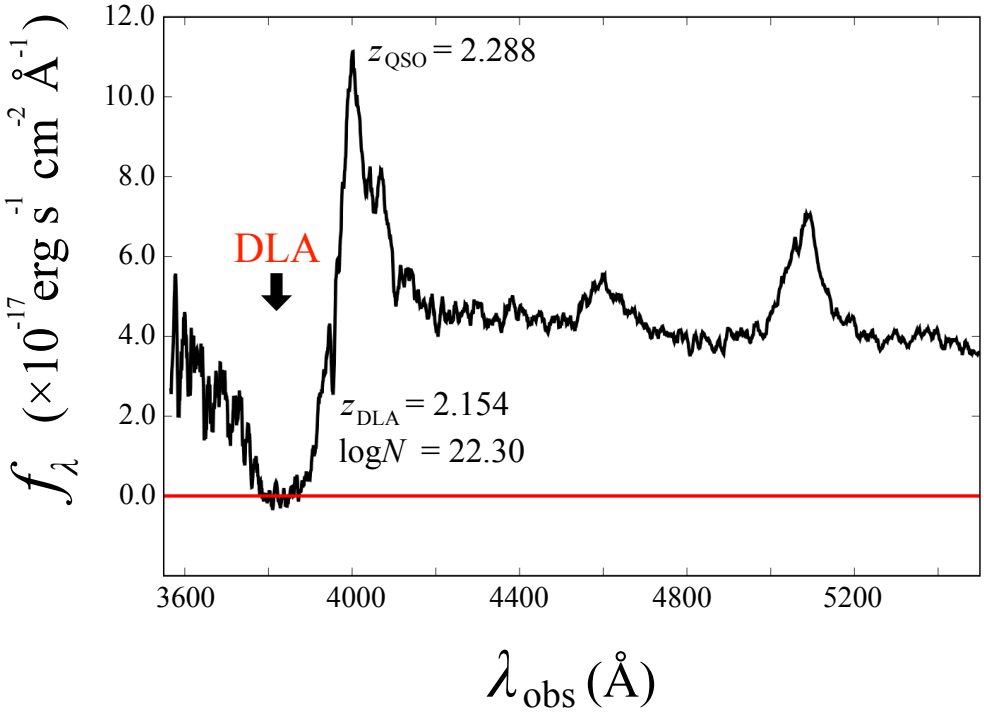

Fig. 1.3: An example of a quasar spectrum with a DLA, the SDSS J134508.82+365214.8, at $z = 2.288$, obtained by the Baryon Oscillation Spectroscopic Survey (BOSS; Dawson et al., 2013). This spectrum shows a DLA with $\log N_{\rm HI} = 22.30$ cm^{-2} at $z = 2.154$. The horizontal red line corresponds to $f_\lambda = 0$.

DLAs ($N_{\rm HI} > 2 \times 10^{20}$ cm^{-2}) is defined based on $N_{\rm H\,I}$ of local spiral galaxies (Wolfe et al., 1986). This historical threshold is optimal for physical reasons too. Hydrogen is likely to be neutral at $N_{\rm HI} > 2 \times 10^{20}$ cm^{-2} while it is likely to be ionized blow the threshold for the DLA (e.g., Viegas & Friaca, 1995; Prochaska & Wolfe, 1996). At $z \sim 2$, almost all ($\sim$90%) H I content of the Universe is dominated by DLAs. On the other hand, the H I mass dominated by DLAs is only $\sim$55% at at $z > 3.5$ (e.g., Storrie-Lombardi & Wolfe, 2000; Wolfire et al., 2003; O'Meara et al., 2007). Remaining $\sim$45% is in the sub-DLAs at $z > 3.5$ (Péroux et al., 2003). Therefore not only DLAs but also sub-DLAs are important as gas reservoirs for star-formation.

Though the DLA is such an important population, their nature is still under the debate. It has been suggested that DLAs are progenitors of present-day disk galaxies (e.g., Prochaska & Wolfe, 1997, 1998). However, there are some other ideas for the origin of DLAs such as outflows (e.g., Taniguchi & Shioya, 2000, 2001), tidal tails (Kacprzak et al., 2010), low surface brightness galaxies (Impey & Bothun, 1989; Jimenez et al., 1998, 1999), dwarf galaxies (Matteucci et al., 1997; Lanfranchi & Friaça, 2003), galactic building blocks (Haehnelt et al., 1998), and so on. To discriminate these scenarios for the DLA origin, systematic studies of the properties of optical counterparts of DLAs are required. Though the optical identification of high-z DLAs had been extremely challenging due to their faintness, recent observations using 8–10 m-class telescopes and high sensitivity cameras are gradually identifying the DLA counterparts even at $z > 2$ (Fynbo et al., 2010, 2011, 2013; Péroux et al., 2011, 2012; Bouché et al., 2013; Krogager et al., 2012, 2013; Kashikawa et al., 2014; Srianand et al., 2016; Sommer-Larsen & Fynbo, 2017, and references therein; see also Table 1.1).

A number of observations to identify DLA counterparts have been conducted at both of high and low redshift. A difficulty for identifying high-z DLA counterparts is caused by the faintness of them. Of course, the faintness of DLAs is a less serious problem when we focus on low-z DLAs. On the other hand, since redshifted Lyα absorption of DLAs at $z < 1.7$[1] is in the UV wavelength range, we can not confirm the presence of DLAs based on the ground-based optical spectroscopy. Therefore, low-z DLAs are confirmed by measuring $N_{\rm HI}$ through UV spectroscopy using space telescopes such as Hubble Space Telescope (HST). It is known that Mg IIλ2796 absorption, which can be observed at lower-z than Lyα, is a good tracer for DLAs since DLAs tend to show Mg II absorption with rest-frame equivalent widths of $EW_0 >$ 0.6 Å (e.g., Churchill et al., 2000; Rao & Turnshek, 2000; Rao et al., 2006). Since galaxy counterparts of low-z DLAs traced by Mg II can be observed easier than those of high-z DLAs, various studies investigating properties of DLA counterparts at low-z have been performed.

Most DLA counterparts at low-z show low-metallicities (e.g., Pettini et al., 1999; Jimenez et al., 1999), suggesting that the origin of low-z DLAs is metal-poor dwarf galaxies (Jimenez et al., 1999) or low-surface brightness galaxies (Jimenez et al., 1999). Kacprzak et al. (2010) studied a well-known DLA, DLA 1127–145, at $z = 0.313$ based on the HST images and long-slit spectroscopy with Ultraviolet and Visual Echelle Spectrograph (UVES) on the Very Large Telescope (VLT). They found that this DLA is in the group environment where there are 8

[1] In fact, due to low sensitivity in the shorter wavelength range in optical, confirming $z < 2$ DLAs is challenging.

galaxies in the impact parameter (the projected distance between the quasar sightline and a galaxy, denoted by b) range of $17 < b < 241$ kpc. They claimed that the origin of this DLA is tidal tails that are result of the interaction of galaxies. Rao et al. (2011) identified counterparts of 80 absorbers (including DLAs, sub-DLAs, and LLSs) at $z < 1$ based on imaging observations. Identified counterparts have impact parameters to the quasar sightline up to 100 kpc. Then they suggested that outflows or tidal tails may contribute to DLAs. Since the nature of optical counterparts of DLAs examined so far is highly heterogeneous, the nature of DLAs is still unclear even at low redshift. This is mainly due to the small number of confirmed DLAs as described above. So far the number of DLAs at $z < 1.7$ which are spectroscopically confirmed by HST observations is less than 200 (e.g., Rao et al., 1995; Rao & Turnshek, 2000; Rao et al., 2006; Turnshek et al., 2015), which is much smaller than $z > 2$ DLAs (see Section 1.5). Among such low-z DLAs, $\sim$100 optical counterparts (including candidates whose redshift measurements are uncertain) have been identified. More confirmations of $N_{\rm HI}$ of absorbers and certain identification of counterparts are required to understand the nature of DLAs at $z < 1$.

As described in Section 1.1, the SFRD peaks at $z \sim 2$ and the gas fraction in galaxies become higher at higher redshift. Therefore the DLA at $z > 2$ is highly interesting to investigate the early phase of the galaxy evolution, where the gas fraction of young galaxies is expected to be very high. Although the distance toward such high-z DLAs makes it difficult to observe faint DLA counterparts, the measurement of $N_{\rm HI}$ is much easier than low-z DLAs. Now we know $>$10,000 DLAs based on the spectroscopic survey of Sloan Digital Sky Surveys (SDSS; York et al., 2000) as described in Section 1.5. The first identification of DLA counterparts at $z > 2$ is the DLA at $z = 3.150$ toward a quasar, Q2233+131 (Djorgovski et al., 1996). The counterpart seems to be a young disk galaxy and supports the idea that DLAs correspond to the progenitors of disk galaxies proposed by Prochaska & Wolfe (1996, 1997). Although the success rate is low ($\sim$10%), counterparts of $z > 2$ DLAs have been gradually identified (Table 1.1). Most of counterparts are detected with the Lyα emission. Since the Lyα emission of them often shows extended morphology, it is suggested that outflows may contribute to the origin of high-z DLAs (e.g., Krogager et al., 2013; Kashikawa et al., 2014). So far, to identify DLA counterparts, high-metallicity DLAs are mainly focused on because counterparts of such a DLA tend to show higher luminosity ("luminosity–metallicity relation" of DLAs; Møller et al., 2004). Therefore, the current sample of DLA counterparts is possibly biased toward more chemically matured, i.e., evolved systems. To understand the nature of high-z DLAs including chemically young objects, more identifications of counterparts based on unbiased samples are needed.

1.4 Lyα emitters

Another well known population of young galaxies at high-z is the LAE (Cowie & Hu, 1998). The strong Lyα emission observed for LAEs is produced through the photoionization by young stars in the LAEs. Therefore, we can recognize young galaxies at high redshift through the Lyα emission line, in addition to the DLA as described in Section 1.3. For discovering LAEs, a number of imaging surveys using narrow-band filter(s) have been carried out so far (e.g.,

Table 1.1: DLA counterparts at $z > 2$ identified spectroscopically.

Quasar	$z_{\rm QSO}$	$z_{\rm DLA}$	$\log N_{\rm HI}$ ($\rm cm^{-2}$)	θ^* ($''$)	$b^\dagger$ (kpc)	reference
Q2233+131	3.298	3.150	20.00	2.51	18.52	Djorgovski et al. (1996)
Q2206–1958	2.559	1.920	20.65	0.99	8.09	Møller et al. (2002)
PKS 0458–02	2.286	2.040	21.65	0.31	2.44	Møller et al. (2004)
Q2222–0946	2.926	2.354	20.65	0.80	6.67	Fynbo et al. (2010)
J0918+1636	3.086	2.583	20.96	1.98	16.20	Fynbo et al. (2011)
						Sommer-Larsen & Fynbo (2017)
J1135-0010	2.888	2.207	22.10	0.1	0.9	Noterdaeme et al. (2012b)
J0338–0005	3.068	2.220	21.05	0.49	4.12	Krogager et al. (2012)
HE 2243-6031	3.01	2.329	20.62	3.1	26	Bouché et al. (2013)
J0918+1636	3.086	2.412	21.26	$<$0.25	$<$2.0	Fynbo et al. (2013)
J0310+0055	3.782	3.115	20.05	3.80	28.0	Kashikawa et al. (2014)
J2358+0149	3.255	2.979	21.69	1.5	21	Srianand et al. (2016)
J0817+1351	4.398	4.260	21.30	6.2	42	Neeleman et al. (2017)
J1201+2117	4.579	3.798	21.35	2.5	18	Neeleman et al. (2017)

Notes.
* The impact parameter between quasar LoS and the counterpart in arcsec.
† The impact parameter between quasar LoS and the counterpart in kpc in the physical scale.

Rhoads et al., 2000; Malhotra & Rhoads, 2002; Taniguchi et al., 2005; Kashikawa et al., 2006; Gawiser et al., 2006, 2007; Nilsson et al., 2007, 2009; Ouchi et al., 2008; Ono et al., 2010a,b, 2012; Hayes et al., 2014). Typical LAEs have the stellar mass of $10^8 - 10^9\ M_\odot$, the age of 5–100 Myr, and the star-formation rate (SFR) of $SFR \sim 1 - 10\ M_\odot\ \mathrm{yr}^{-1}$. Note that there are some LAEs with more evolved stellar populations with stellar masses of $10^{10} - 10^{11}\ M_\odot$, and ages of ∼0.3–2 Gyr (Taniguchi et al., 2015). However since such a evolved LAE is very rare (0.2–0.6% of star-forming galaxies), we can investigate properties of young galaxies in the early Universe by focusing on LAEs.

One of the most basic statistics to understand the nature and evolution of any populations of galaxies is the luminosity function (LF). The LF is the number density of galaxies per unit luminosity and usually fitted by the Schechter function (Schechter, 1976), that is described as follows:

$$\phi = \frac{dn}{dL} = \frac{\phi_*}{L_*} e^{-L/L*} (\frac{L}{L_*})^\alpha, \tag{1.10}$$

where α is the index of the LF slope in the faint side, L_* is the characteristic luminosity, and ϕ_* is the characteristic number density (i.e., the number density at the characteristic luminosity). When we describe the luminosity in the magnitude, the Schechter function is written as follows,

$$\phi(M) = (0.4\ln 10)\phi_* \exp\{-10^{0.4(M-M_*)}\} 10^{-0.4(\alpha+1)(M-M_*)}, \tag{1.11}$$

where M_* is the characteristic magnitude. Note that, in the case of LAEs, the L could be either the Lyα luminosity or the rest-frame UV continuum luminosity and therefore one should be careful to discuss the LF of LAEs. So far, a number of study for the Lyα LF of LAEs have been conducted in a wide redshift range of $z \sim 0 - 7$ (e.g., Rhoads & Malhotra, 2001; Ajiki et al., 2003; Kashikawa et al., 2006; Gronwall et al., 2007; Ouchi et al., 2008, 2010; Cowie et al., 2010, 2011; Zheng et al., 2013; Matthee et al., 2015; Konno et al., 2014, 2016). The Lyα LF of LAEs shows strong evolution below $z \sim 2$. More specifically, the Lyα LF of LAEs decreases significantly from $z \sim 2$ toward $z \sim 0$. The Lyα LF at $z > 6$ also decreases with decreasing redshift. On the other hand, at $z \sim 3 - 6$, the Lyα LF dose not show significant evolution.

Another important statistics of LAEs is the EW. The EW is the ratio of the Lyα line flux ($F_{\mathrm{Ly}\alpha}$) to the UV continuum flux density (f_{cont}) defined as

$$EW = \frac{F_{\mathrm{Ly}\alpha}}{f_{\mathrm{cont}}}. \tag{1.12}$$

In many case, the threshold of rest-frame Lyα EW (EW_0) for selecting LAEs is set to be EW_0 >20 Å. It is known that the younger LAEs tend to show the larger Lyα EW_0 (e.g., Malhotra & Rhoads, 2002; Nagao et al., 2007). In the previous studies, the frequency distribution of Lyα EW_0 is often investigated to discuss the properties of LAEs. For a quantitative comparison of the Lyα EW_0, the following analytic formula has been sometimes adopted,

$$N = C \times e^{-EW_0/w_0} \tag{1.13}$$

(e.g., Gronwall et al., 2007; Mawatari et al., 2012), where w_0 is the e-folding length. A higher value of w_0 indicates that the fraction of LAEs with a larger EW_0 is relatively high. In Table 1.2, we show the previously reported w_0 at various redshifts. Figure 1.4 shows the observed w_0 at various redshifts (see also Table 1.2). Zheng et al. (2014) fit the redshift evolution of w_0 with an analytic function,

$$w_0(z) = A \times (1+z)^{\xi} \tag{1.14}$$

and obtain $A = 7.3^{+1.5}_{-1.3}$ Å and $\xi = 1.7 \pm 0.2$ (the blue solid curve in Figure 1.4). Note that, the values of w_0 in Table 1.2 and Figure 1.4 are not corrected for the IGM absorption. After applying the IGM correction, Zheng et al. (2014) obtain $A = 14^{+2.8}_{-2.3}$ Å and $\xi = 1.1 \pm 0.1$ (the black dotted curve in Figure 1.4). Zheng et al. (2014) conclude that the e-folding length of the Lyα EW_0 distribution of LAEs shows possible redshift evolution (see also Nilsson et al., 2009). This trend indicates that LAEs at lower redshift may be more evolved than those at higher redshift. However, the evolution of the Lyα EW is difficult to explain with a simple model (e.g., Nilsson et al., 2009; Mawatari et al., 2012). Shibuya et al. (2017) also reported possible evolution of the Lyα EW distribution. They pointed out that w_0 strongly depends on the depth of observations and the Lyα EW_0 threshold for LAEs. More sample at various redshifts and careful analysis are required to understand the evolution of the Lyα EW_0.

1.5 DLA sample based on the Baryon Oscillation Spectroscopic Survey

To study DLAs, we need enough number of background sources (mostly quasars, but could be also gamma-ray bursts or bright galaxies, as described in Section 1.3) since we cannot find DLAs without them. Now a new catalog listing a large number of DLAs based on the Baryon Oscillation Spectroscopic Survey (BOSS; Dawson et al., 2013) is available. The BOSS is a legacy project of the SDSS aiming to measure the scale of the baryon acoustic oscillation in Lyα forests. For this purpose, spectra of $\sim$297,301 quasars have been taken Pâris et al. (2012). Noterdaeme et al. (2012a) construct the DLA catalog including 12,801 absorbers with $N_{\rm HI} > 10^{20.0}$ cm^{-2} based on the quasar catalog provided by (Pâris et al., 2012). The quasar catalog constructed by Pâris et al. (2012) is based on the ninth data release (DR9) of SDSS and including 87,822 quasars in the field of $\sim$3,275 deg^2. Note that the previous DLA catalog based on the SDSS DR7 includes only 1,426 absorbers (937 of them are DLAs) at $2.15 < z < 5.2$ (Noterdaeme et al., 2009). Therefore the number of DLAs in the DR9 is $\sim$9 times as many as that in the DR7, enabling us to work on the statistical studies based on the large sample of DLAs. Note that there are updated versions of BOSS DLA catalog[2] based on the SDSS DR10 and the DR12. Although these updated catalogs include much more DLAs over a wider area than DR9 catalog, the selection criteria in the newer catalogs (DR10 and DR12) are so loose that a significant fraction of objects listed in those catalogs are likely contaminations (non-DLAs). Therefore, we used the DR9 catalog including plausible sample of absorbers with $N_{\rm HI} \geq 10^{20.0}$ cm^{-2}.

[2] `http://www2.iap.fr/users/noterdae/DLA/DLA.html`

Table 1.2: *e*-folding length of the distribution of the Lyα EW_0, w_0, at various redshifts

z	w_0	reference
0.3	22 ± 9	Cowie et al. (2010)
2.1	50^{+9}_{-6}	Ciardullo et al. (2012)
2.3	53.5 ± 4.7	Ogura et al. (2017)
2.3	48.5 ± 1.7	Nilsson et al. (2009)
2.4	43.7 ± 0.4	Mawatari et al. (2012)
3.1	70^{+7}_{-5}	Ciardullo et al. (2012)
5.7	108 ± 20	Kashikawa et al. (2011)
5.7	123^{+61}_{-23}	Hu et al. (2010)
6.5	79 ± 19	Kashikawa et al. (2011)
6.5	178^{+433}_{-26}	Hu et al. (2010)

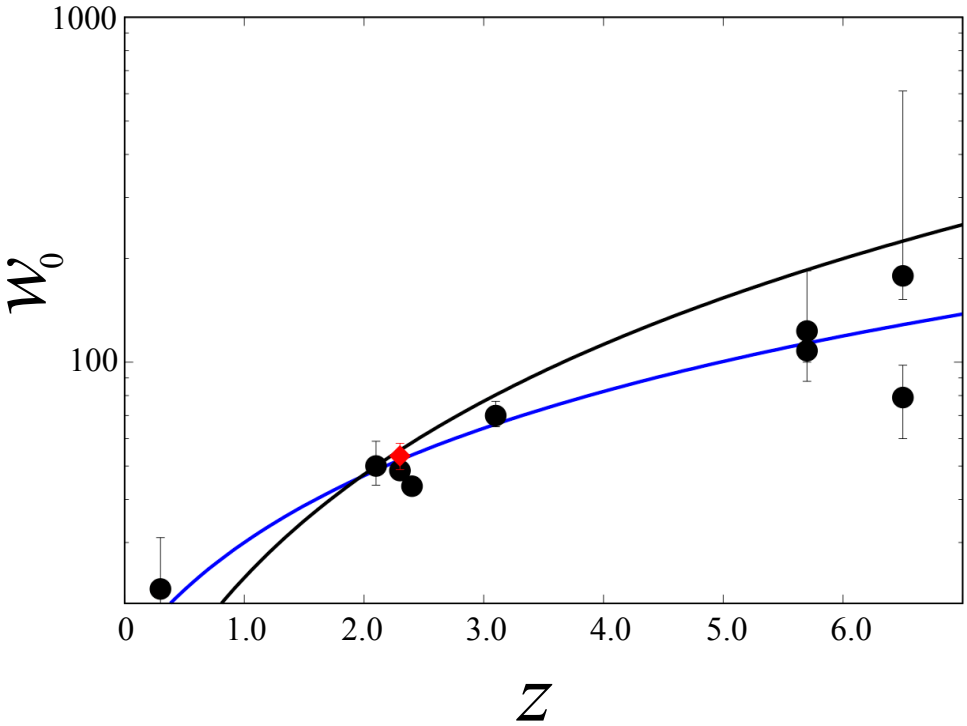

Fig. 1.4: The redshift evolution of w_0. The red diamond and black filled circles denote the w_0 of Ogura et al. (2017) and those at various redshifts obtained by some previous works, without the IGM correction (see Table 1.2). The blue solid curve shows the analytic function fit to w_0 by Zheng et al. (2014). The black solid curve shows the analytic function fit after the IGM correction (Zheng et al., 2014).

1.6 The purpose of this dissertation

To understand the complete picture of the galaxy evolution, the process that the cold gas is converted to stars is a fundamental issue. Though the DM is one important ingredient of galaxies, the evolution of dark matters is well studied by the CDM cosmology as described in Section 1.1. The stellar component is also well studied by focusing on the star-forming galaxies at high-z Universe. Compared with those two components, the evolution of the gas component is less understood. Therefore, in this dissertation we are focusing on the quasar absorption-line systems to investigate the properties of the gaseous component in young gas-rich galaxies at high redshift. Especially, strong Lyα absorbers, such as DLAs, are important systems. So far, despite of the greats effort to understand the nature of DLAs, it is still under the debate.

Although only a small number of DLA counterparts have been identified, a large fraction of them show the Lyα emission. General properties of LAEs, i.e., young and relatively low SFR, imply a possible close relation between LAEs and DLAs. For investigating the relationship between DLAs and LAEs, we focus on regions where some DLAs are distributed within a narrow area because we can effectively investigate the properties of galaxies and search for the galaxies associated with DLAs in such regions. Then, we carried out deep and wide narrow-band imaging observations. This is the first trial to study properties of galaxies in the concentrated region of strong Lyα absorbers such as DLAs. The combination of the large sample of DLAs provided by Noterdaeme et al. (2012b) and the wide field-of-view (FoV) of Subaru/Suprime-Cam (Miyazaki et al., 2002) enables us to study the galaxy properties in absorber-concentrated regions. Based on the obtained data we select the LAEs using color-magnitude diagram and derive the statistics including the spatial distribution of LAEs against the positions of DLAs, the Lyα LF, and the frequency distribution of the Lyα EW_0. These properties are compared with those in different environment at similar redshift, including blank fields and overdensity regions of LAEs. We then search for LAEs which are located at very close to DLAs and identifying possible counterparts of DLAs and characterize galaxies associate with DLAs[3].

This dissertation is organized as follows. We describe the properties of LAEs in the concentrated region of Lyα absorbers such as DLAs in Chapter 2. We then give our conclusion in Chapter 3. In Appendix B, we report our preparatory work toward systematic identifications of high-z DLA counterparts by utilizing wide-field deep optical imaging survey data. We use a Λ CDM cosmology with $H_0 = 70$ km s^{-1} Mpc^{-1}, $\Omega_M = 0.3$, and $\Omega_\Lambda = 0.7$, throughout this paper. Magnitudes are all given in the AB system.

[3]This study has been published in PASJ (Ogura et al., 2017, PASJ, 69, 51).

CHAPTER 2

A SEARCH FOR LYα EMITTERS AROUND A CONCENTRATED REGION OF STRONG LYα ABSORBERS AT $z = 2.3$[1]

In order to investigate the physical relationship between strong Lyα absorbers ($\log N_{\rm HI} \geq 20.0$ cm^{-2}) such as damped Lyα absorption systems (DLAs) and young star-forming galaxies at high redshift, we have conducted narrow-band observations of Lyα emitters (LAEs) in a concentrated region of strong Lyα absorbers at $z = 2.3$, the J1230+34 field. Using a catalog of Lyα absorbers with $\log N_{\rm HI} \geq 20.0$ cm^{-2} based on the Baryon Oscillation Spectroscopic Survey (BOSS), we found six fields where three or more absorbers are concentrated within a (50 Mpc)^3 cubic box in the comoving scale. Among them, we focus on the J1230+34 field, where 2 DLAs and 2 sub-DLAs present. Our narrow-band imaging observations with Subaru/Suprime-Cam using a custom-made filter, *NB*400 ($\lambda_{\rm c} = 4003$ Å and FWHM= 92 Å) yield a sample of 149 LAEs in this field. In the large scale ($\sim$50 Mpc), we have found no differences between the obtained Lyα luminosity function and those in the blank fields at similar redshifts. We also compare the frequency distribution of the Lyα rest-frame equivalent width (EW_0) in the target field and other fields including both overdensity region and blank field, but find no differences. On the other hand, in the small scale ($\sim$10 Mpc), we have found a possible overdensity of LAEs around a DLA with the highest H I column density ($\log N_{\rm HI} = 21.08$ cm^{-2}) in the target field while there are no density excess around the other absorbers with a lower $N_{\rm HI}$.

2.1 Introduction

Investigating the formation and evolution of galaxies is one of the important topics in the modern astrophysics. In particular, it is interesting to study how cold gas is converted to stars in galaxies at the very early phase of evolution. To investigate the very early phase of the galaxy

[1]Contents in this chapter has been published in PASJ (Ogura et al., 2017)

evolution, we focus on two populations that are thought to be gas-rich young systems, damped Lyα absorption systems (DLAs) and Lyα emitters (LAEs).

The DLA is a class of quasar absorption-line systems, which has a column density of $N_{\rm HI} \geq 10^{20.3}$ cm^{-2} (Wolfe et al., 2005). The DLA provides a powerful tool to investigate the nature of the cold gas at high-z because they trace the intervening gas along the line-of-sight to quasars and can be detected as a strong Lyα absorption line on quasar spectra regardless of the luminosity of their stellar component. Since DLAs dominate the neutral-gas content in a wide redshift range (Storrie-Lombardi & Wolfe, 2000), they are thought to be gas reservoirs for the star-formation in the high-z Universe. Though the DLA is such an important population, their nature is still under the debate (Prochaska & Wolfe, 1997; Taniguchi & Shioya, 2000, 2001; Kacprzak et al., 2010) because it is often difficult to identify their optical counterparts due to their faintness, especially at high redshift (see for recent identifications at $z > 2$, Fynbo et al., 2010, 2011, 2013; Péroux et al., 2011, 2012; Bouché et al., 2013; Krogager et al., 2012, 2013; Kashikawa et al., 2014; Srianand et al., 2016; Sommer-Larsen & Fynbo, 2017, and references therein). In many cases, counterparts of high-z DLAs have been found as LAEs. This is consistent with the idea that the nature of DLAs is young gas-rich galaxy.

The LAE is a population of galaxies selected by their strong Lyα emission. Since typical LAEs show faint UV continuum and large Lyα equivalent width (EW), it is considered that they are young galaxies (e.g., Malhotra & Rhoads, 2002; Taniguchi et al., 2005; Kashikawa et al., 2006; Gawiser et al., 2007; Nilsson et al., 2007; Ono et al., 2010a,b, 2012). So far, various researches to understand properties of LAEs have been conducted and found that their typical stellar mass is $10^8 - 10^9$ $M_\odot$ and the age is in order of 100 Myr (e.g., Gawiser et al., 2006, 2007; Nilsson et al., 2009; Ono et al., 2012). Note that recently, some LAEs with more evolved stellar populations have been found (e.g., Ono et al., 2010b; Taniguchi et al., 2015). In addition, some sensitive radio observations of CO molecular lines in high-z galaxies suggest that the gas fraction is larger at higher redshifts, and sometimes the gas mass fraction reaches up to $\sim$0.5 or even more (e.g., Carilli & Walter, 2013; Troncoso et al., 2014). Therefore the LAE as well as the DLA at high z is a key population to understand the early phase of the galaxy evolution. However, the relation between these two populations is still unclear. As we mention above, although most of DLA counterparts at high z show the Lyα emission, only few counterparts of high-z DLAs have been identified so far. Given the idea that DLAs are neutral gas reservoir for the star formation, the relation of the DLAs and young galaxies (i.e., LAEs) is interesting.

It should be noted that DLAs can be recognized only when they have a background quasar (BGQSO). The number density of such quasars had been too low to investigate grouping or clustering properties of DLAs. However, such a situation has been recently changed after the data release of Baryon Oscillation Spectroscopic Survey (BOSS; Eisenstein et al., 2011; Dawson et al., 2013). The quasar catalog based on the BOSS data from Data Release 9 of the Sloan Digital Sky Survey (SDSS DR9; Ahn et al., 2012) includes 87,822 quasars mainly at $2 < z < 4$ (Pâris et al., 2012). By utilizing the BOSS quasar sample, Noterdaeme et al. (2012a) found 12,801 absorbers with $N_{\rm HI} > 10^{20.0}$cm^{-2} (partly including sub-DLAs which are

absorption-line systems with $10^{19.0}\mathrm{cm}^{-2} < N_{\mathrm{HI}} < 10^{20.3}\mathrm{cm}^{-2}$; Péroux et al., 2003). This new and large absorber sample enables us to study the spatial distribution of DLAs.

Here, we focus on regions where some absorbers with a narrow redshift range are concentrated in a narrow area. Such a region is interesting for following two reasons. (1) Such a region may harbor large amount of neutral gas and thus it may correspond to the region where galaxies are rapidly evolving, and (2) to observe such a region, we can effectively search for counterparts of absorbers. By observing LAEs around such a region, we can investigate the relation of gas-rich systems and young galaxies. For this purpose, wide-field narrow-band (NB) observations are very useful. By combining NB filters and imaging instruments with a wide FoV, we can effectively observe LAEs in a wide area.

In this chapter, we report our observational trial for studying properties of LAEs around a concentrated region of strong Lyα absorbers to investigate very early stage of the galaxy evolution based on the NB imaging observations. This paper is organized as follows. In Section 2.2, we present the target field selection. The evaluation of the rarity of absorber-concentrated regions are also described in Section 2.2. Imaging observations of LAEs and data reduction processes are shown in Section 2.3. The results are given in Section 2.4. The Lyα luminosity function of detected LAEs and the frequency distribution of Lyα EW are our main results. We discuss interpretations of the absorber concentrated region in Section 2.5. Finally we present our conclusion of this chapter in Section 2.6.

2.2 Target field selection

2.2.1 The target field

In this study, we focus on the J1230+34 field, where there are 2 DLAs and 2 sub-DLAs at $z \sim 2.3$ within a cubic region of $(\sim 50\mathrm{Mpc})^3$. Table 2.1 shows the basic data of four absorbers, and Figure 2.1 shows the sky distribution of the absorbers and quasars in the J1230+34 field. The BOSS spectra of quasars with a strong absorption in the target field are shown in Figure 2.2. We selected this region from the catalog of strong ($N_{\mathrm{HI}} > 10^{20.0}\mathrm{cm}^{-2}$) Ly$\alpha$ absorbers based on the BOSS quasars (Noterdaeme et al., 2012a).

Here, we describe the selection process of the target field. First, we define the sample of absorbers and their BGQSOs. The redshift distribution of the absorbers in the BOSS DLA catalog shows its peak at $z \sim$2.2 (Figure 2.3). Fortunately, there is a suitable narrow-band (NB) filter of Suprime-Cam (Miyazaki et al., 2002) on the 8.2 m Subaru telescope, *NB*400, to observe the Lyα emission from objects around that redshift. Note that, although there are some NB filters of Suprime-Cam which cover the redshift range of $z \sim 2-3$ (see Table 2.2 and Figure 2.4), *NB*400 is the most suitable one since it covers larger number of absorbers than other NB filters as shown in Table 2.2. *NB*400 is a custom-made NB filter whose central wavelength and width in full width at half maximum (FWHM) are 4003 Å and 92 Å, respectively. This wavelength coverage corresponds to the redshift range of $2.255 < z < 2.330$ for

Table 2.1: The information of absorbers in the J1230+34 field

No.	Quasar Name	R.A. (deg.)	Dec. (deg.)	$z_{\rm QSO}$	$z_{\rm DLA}$	$\log N_{\rm HI}$ (cm^{-2})	Class
1	SDSS J122940.83+340132.3	187.4201	34.0256	2.353	2.303	20.15	sub-DLA
2	SDSS J122942.74+342202.1	187.4281	34.3673	2.966	2.268	21.08	DLA
3	SDSS J122955.14+341123.7	187.4798	34.1899	2.436	2.304	20.24	sub-DLA
4	SDSS J123143.46+341727.6	187.9311	34.2910	2.976	2.262	20.48	DLA

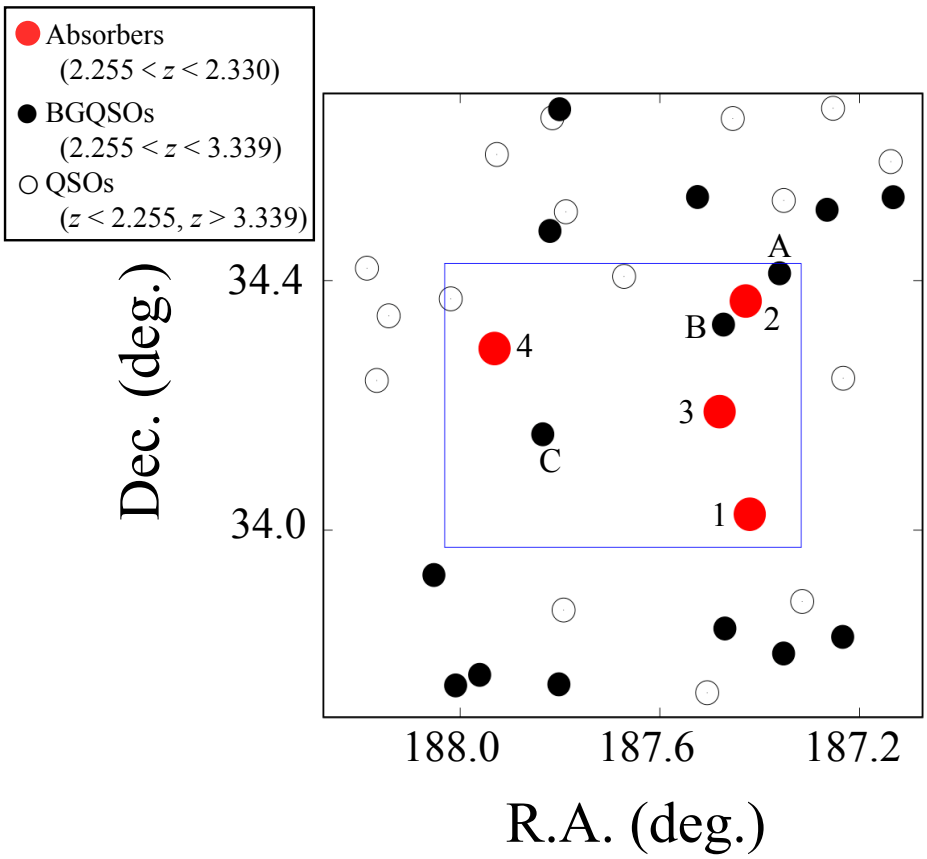

Fig. 2.1: The sky distribution of absorbers in the J1230+34 field ($1^\circ \times 1^\circ$). The blue box shows the FoV of Suprime-Cam ($34' \times 27'$) in our observation. Filled circles show line-of-sights (LoSs) to background quasars (BGQSOs). Red and black filled circles show those with absorber and without absorbers at $2.255 < z < 2.330$. IDs for the absorbers (filled red circles) are same as in Table 2.1. Open circles show LoSs to BOSS quasars that do not satisfy the criteria for BGQSOs ($z < 2.255$ or $z > 3.339$).

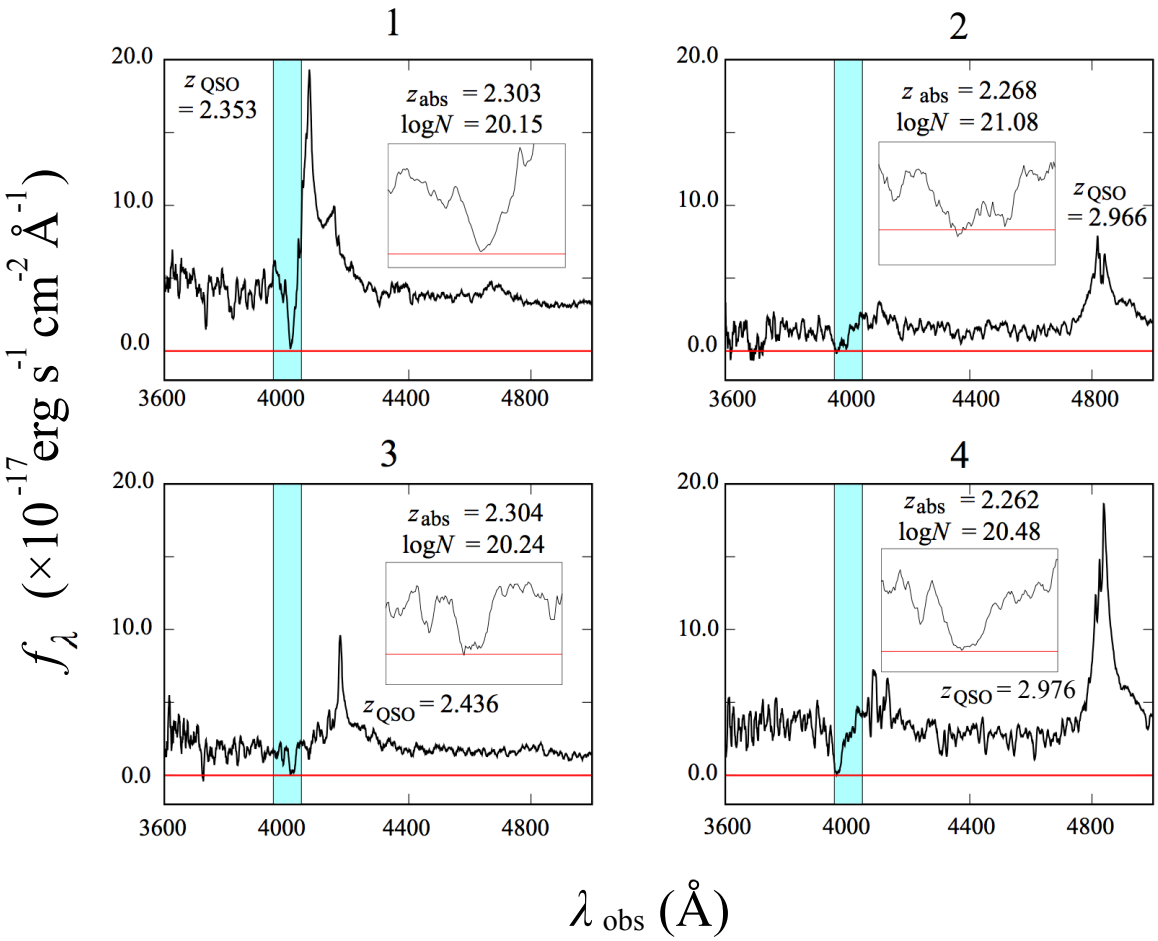

Fig. 2.2: BOSS spectrum of quasars showing a strong intervening Lyα absorption line at $2.255 < z < 2.330$ in the J1230+34 field. Cyan shadowed region in each panel shows the wavelength coverage of *NB*400. Horizontal red lines correspond to $f_\lambda = 0$. Inserted panels show the magnified view around the absorbing feature.

the Lyα emission (1216 Å in the rest frame). Therefore, throughout this paper, we define the absorber sample as those at $2.255 < z < 2.330$. As for the BGQSOs, we set their redshift range to $2.255 < z < 3.339$. The lower limit of the redshift range for BGQSOs is the same as that for absorbers, taking also into account of proximity DLAs (PDLAs; Prochaska et al., 2008). The PDLA is a population of DLAs at a velocity separation of $< 3{,}000$ km s^{-1} from the BGQSO (PDLAs; Prochaska et al., 2008). We determine the upper limit of the redshift of BGQSOs by considering the Lyman limit of BGQSOs. Since the signal-to-noise (S/N) ratio of a quasar spectrum is very low at the wavelength range shorter than the Lyman limit (912 Å in the rest frame), it is difficult to find absorbers at this wavelength range. Therefore we focus only on quasars at the redshift where their Lyman limit locates at shorter wavelength than the *NB*400 coverage. We remove quasars with the balnicity index (BI; Weymann et al., 1991) $>1{,}000$ km s^{-1} from the BGQSO sample, because it is hard to distinguish Lyα absorbers from broad absorption lines (BALs) in the intrinsic spectra of such BAL quasars (Noterdaeme et al., 2012a). Among the BOSS quasar sample (87,822 quasars at the time of DR9), we regard 47,376 quasars as BGQSOs for absorbers at $2.255 < z < 2.330$. The number of absorbers at $2.255 < z < 2.330$ whose BGQSOs satisfy the criteria is 824.

Then we search for the concentrated region of strong Lyα absorbers based on this sample. Here, we define the concentrated region as the region where there are three or more absorbers within a cubic space of $(50\ \mathrm{Mpc})^3$. This definition is based on the typical size of galaxy protoclusters. Overzier (2016) shows the redshift distribution of galaxies in several protoclusters which are confirmed spectroscopically. The width of redshift distribution of galaxies in protoclusters at $z \sim 2$ are typically $\Delta z \sim 0.02 - 0.06$ (corresponding to $\sim 26 - 76$ Mpc in the comoving scale). Chiang et al. (2013) also summarized properties of observed protoclusters and most of them show $\Delta z \sim 0.03 - 0.06$ (corresponding to $\sim 38 - 76$ Mpc in the comoving scale). As for the spatial extent of protoclusters, it is known that they could be extended up to dozens of Mpc (e.g., Hayashino et al., 2004; Prescott et al., 2008; Lee et al., 2014). Recently, Franck & McGaugh (2016a,b) search for clusters and protoclusters over a wide redshift range ($2.7 < z < 3.7$), showing that almost all members of a cluster are covered with the circular region whose radius is $\sim$20 Mpc in the comoving scale. In addition, Muldrew et al. (2015) studied to define the high-z protoclusters and found that 90% of a protocluster mass is extended across 50 comoving Mpc at $z \sim 2$. Taking considerations given above into account, we decide the search scale of $(50\ \mathrm{Mpc})^3$ in this work, and define the concentrated regions of strong Lyα absorbers as one with three or more absorbers within $(50\ \mathrm{Mpc})^3$.

As a result, we found 6 absorber-concentrated regions in which there are at least 3 strong Lyα absorbers. Table 2.3 shows the basic data of absorbers in each region and Figure 2.5 shows the sky distribution of absorbers. Note that, 1 of 4 absorbers in the J1230+34 field (No. 4 in Table 2.1) is out of a $(50\mathrm{Mpc})^3$ cube (in the direction along the line of sight). However, this absorber is located at very close to the other 3 absorbers. The comoving distance along the line of sight from absorber No. 4 to the nearest absorber (No. 2) is only 7.7 Mpc and that between No. 4 and farthest absorber (No. 1) is 53.5 Mpc. If considering also this absorber, there are more absorbers in the J1230+34 field than the other 5 fields, and thus this J1230+34 field is

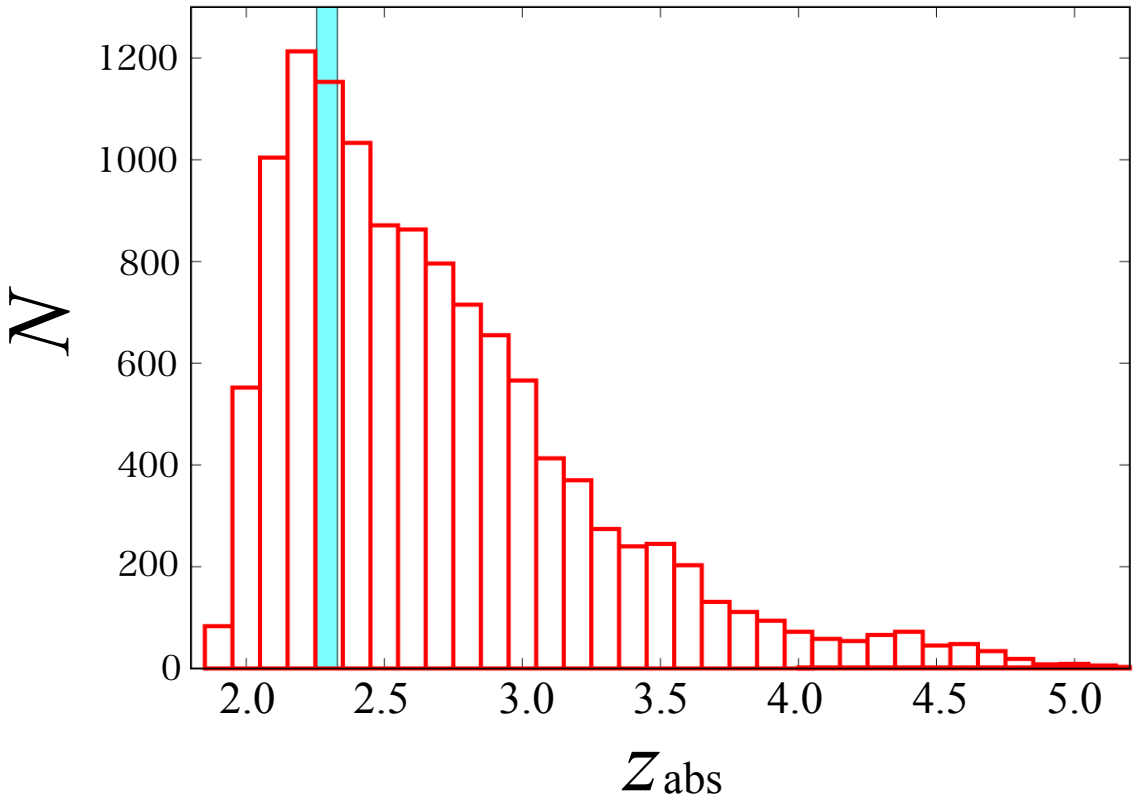

Fig. 2.3: The redshift distribution of absorbers with $N_{\rm HI} > 10^{20.0}$ cm^{-2} in the catalog based on the BOSS (Noterdaeme et al. 2012). Cyan shadow region shows the redshift coverage of *NB*400 ($2.255 < z < 2.330$).

Table 2.2: Numbers of absorbers which can be observed with NB filters of Suprime-Cam whose coverage corresponds to the redshift range of $z \sim 2-3$

filter	λ_c (Å)	FWHM (Å)	redshift coverage	N_{abs}*	N_{pair}†	references
*NB*359	3590	150	$1.920 < z < 2.019$	154	8	Iwata et al. (2009)
*NB*387	3870	94	$2.145 < z < 2.222$	861	120	Nakajima et al. (2012)
*NB*400	4003	92	$2.255 < z < 2.330$	880	177	This work
*NB*413	4140	84	$2.373 < z < 2.438$	723	120	Mawatari et al. (2012)
*NB*428	4297	84	$2.500 < z < 2.568$	646	83	Shimakawa et al. (2017b)
*NB*503	5020	100	$3.109 < z < 3.166$	253	19	Ouchi et al. (2008)

Notes.
* The number of absorbers whose Lyα can be covered by each NB filter.
† The number of pairs of absorbers, where two absorbers exist within 1 FoV of Suprime-Cam at the redshift range covered by each NB.

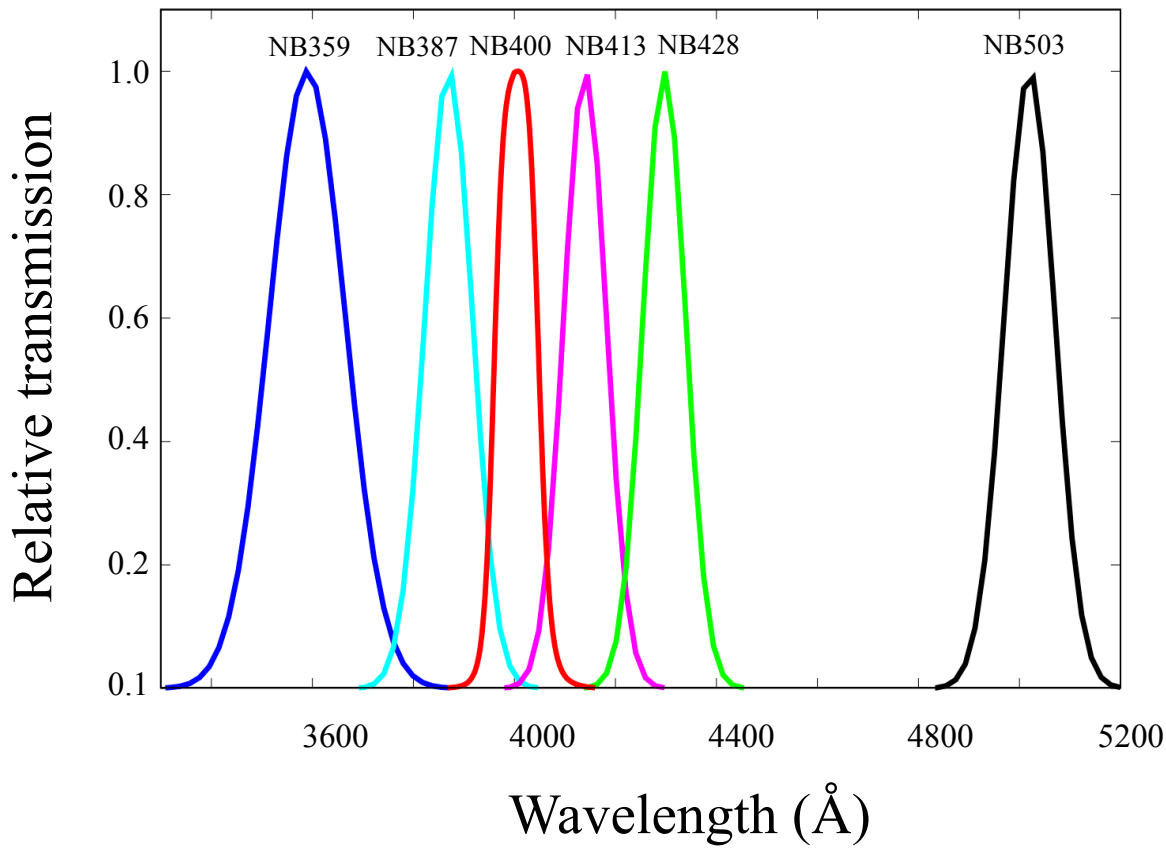

Fig. 2.4: Filter transmission curves of Suprime-Cam NB filters whose coverage corresponds to the redshift range of $z \sim 2-3$. Curves for $NB400$ and $NB428$ are experimentally measured one, while those for remaining four NB filters are shown by assuming the Gaussian profile adopting the central wavelength and width (FWHM) given in Table 2.2. Note that transmission curves in this figure are normalized to have peak transmission of unity.

more interesting as an absorber-concentrated region than the other fields. The rarity of this field is shown in Section 2.2.2. Seven quasars in this region satisfy the criteria for BGQSOs, and 3 (A, B, and C in Figure 2.1) among them do not have absorbers at $2.255 < z < 2.330$. Figure 2.6 shows BOSS spectrum of these BGQSOs. We describe our NB observations of this field in Section 2.4.

2.2.2 *The rarity of the target field*

Here, we show how rare the target region (the J1230+34 field) is. As we described in Section 2.2.1, we define the concentrated region as a region with 3 or more absorbers within the cubic space of (50 Mpc)^3 in the comoving scale. To investigate the rarity of the target field, we examine the selection outcomes by applying some different sizes. In Table 2.4, we show numbers of selected field when we apply various criteria. Regions harboring 4 or more absorbers are extremely rare. The J1230+34 field is the only field harboring 4 absorbers even if we adopt a larger size of (60 Mpc)^3, and only 2 regions are selected even in the case of (70 Mpc)^3. Based on this, we conclude that the J1230+34 field is extremely rare and interesting region. As we described in Section 2.2.1, there are 824 absorbers at $2.255 < z < 2.330$ among line-of-sights to 47,376 BGQSOs. Based on this, the incidence of absorbers at $2.255 < z < 2.330$ is less than 2%.

2.2.3 *The surface number density distribution of absorbers at* $2.255 < z < 2.330$ *and BGQSOs*

Since a quasar absorption-line system can be found only when it has a BGQSO, the sky distribution of BGQSOs is particularly important to discuss that of absorbers. In a region where the surface number density of BGQSOs is relatively high, it is expected that the apparent number of observable absorbers is accordingly higher than regions with a lower surface number density of BGQSOs. Here, we investigate the surface number densities of both absorbers and BGQSOs in each absorber concentrated region to examine whether or not the spatial distribution of BGQSOs influences that of absorbers.

Figure 2.7 shows the average surface number density of absorbers and BGQSOs in all the 6 absorber-concentrated regions, as a function of the radius adopted to calculate the surface density. Here, we set the center of the circular region for the density calculation at the center of the position of absorbers. For calculating the density, we simply divide the number of absorbers at $2.255 < z < 2.330$ by the area to calculate the surface number density. As shown in Figure 2.7, the surface number density of absorbers rapidly decreases with increasing radius while that of BGQSOs appears to be much flatter. The average surface number density of absorbers rapidly approaches to the average of surface number densities calculated for the entire BOSS field (6.99×10^{-5} arcmin^{-2}; the black line in Figure 2.7). The surface number density of absorbers exceeds 3 times the average absorber density for the whole BOSS field at $r \sim 75'$

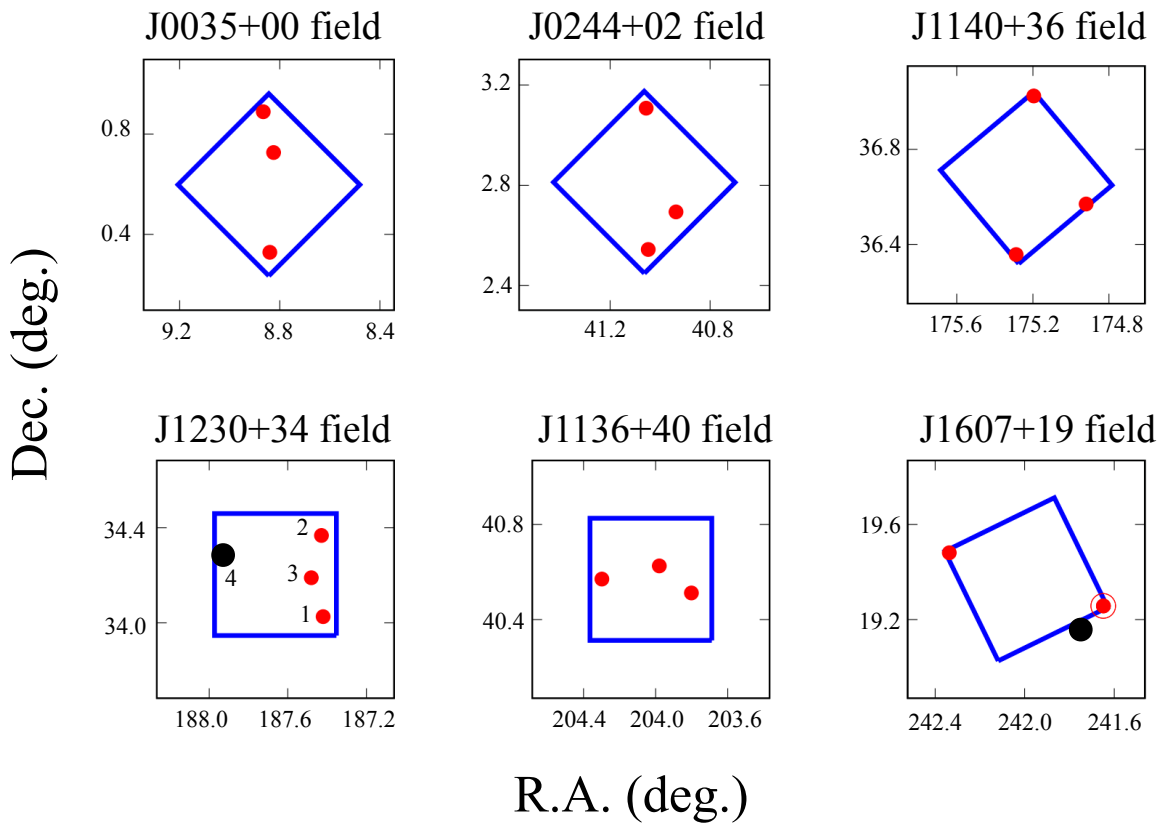

Fig. 2.5: The sky distribution of absorbers in each absorber-concentrated region. Red filled circles show absorbers. Blue boxes show square regions with 50 Mpc (in the comoving scale at $z = 2.3$) on a side. The red filled circle with open red circle in the J1607+19 field denote the quasar sight line with 2 absorbers within the concentrated region. Black filled circles in the J1230+34 field and the J1607+19 field show absorbers at $2.255 < z < 2.330$ out of the $(50\ \mathrm{Mpc})^3$ region. IDs for absorbers in the J1230+34 field are same as in Table 2.1 and Figure 2.1.

Table 2.3: Basic data of the absorber-concentrated regions

Field	R.A. (deg.)	Dec. (deg.)	$z_{\rm QSO}$	$z_{\rm abs}$	$\log N_{\rm HI}$ (cm^{-2})
J0035+00 field	8.8248	0.7260	2.925	2.304	20.40
	8.8400	0.3280	2.360	2.311	20.70
	8.8653	0.8892	2.460	2.282	20.14
J0244+02 field	40.9367	2.6943	2.806	2.264	20.16
	41.0469	2.5439	2.668	2.257	20.78
	41.0558	3.1079	2.289	2.267	20.07
J1140+36 field	174.9200	36.5705	2.904	2.279	20.56
	175.2880	36.3572	2.274	2.271	20.07
	175.1960	37.0252	2.837	2.303	20.15
J1230+34 field	187.4201	34.0256	2.353	2.303	20.15
	187.4281	34.3673	2.966	2.268	21.08
	187.4798	34.1899	2.436	2.304	20.24
J1336+40 field	203.8010	40.5116	2.832	2.268	20.63
	204.2980	40.5707	2.655	2.291	20.03
	203.9800	40.6252	2.288	2.266	20.11
J1606+19 field	241.6490*	19.2572	2.528	2.282	20.00
	241.6490*	19.2572	2.528	2.320	21.40
	242.3370	19.4813	2.844	2.297	21.40

Notes.
* These two absorbers are in the LoS to the same quasar.

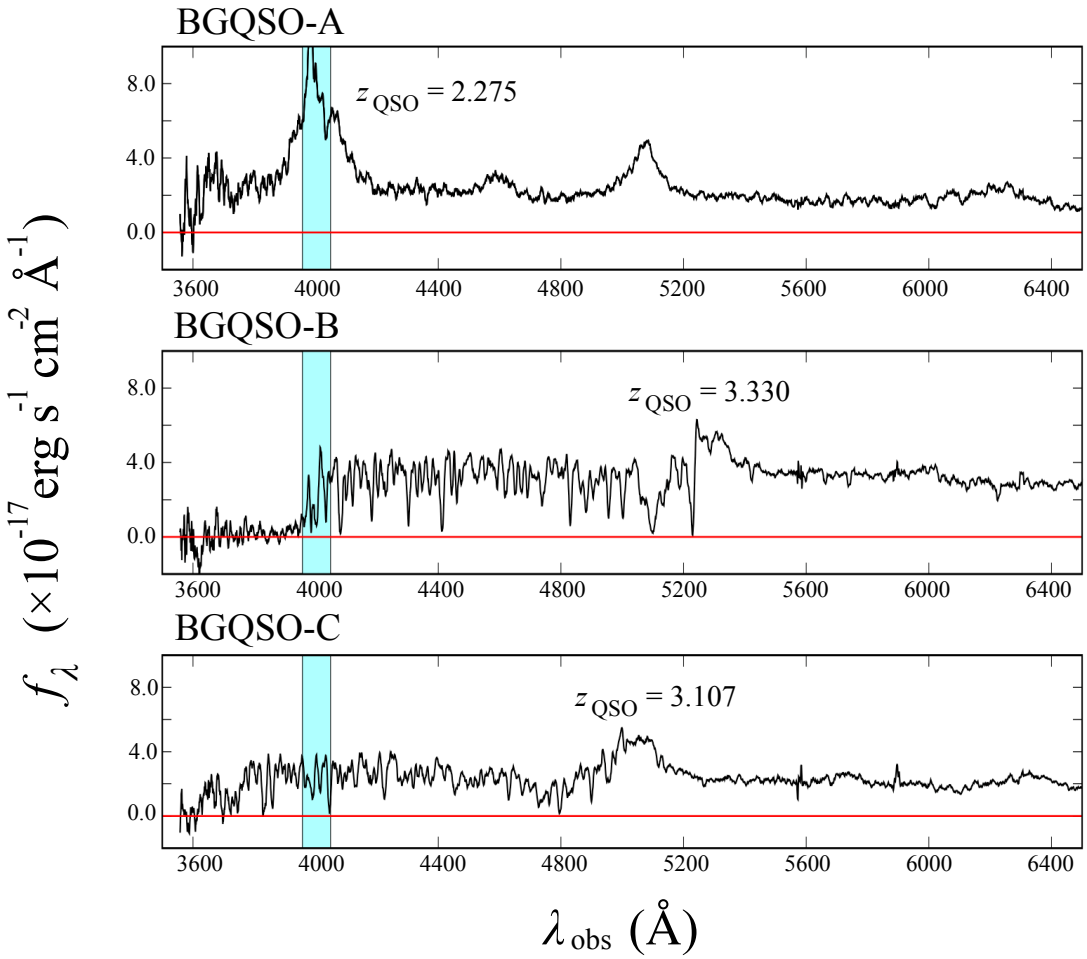

Fig. 2.6: BOSS spectrum of quasars not showing strong intervening Lyα absorption-line at $2.255 < z < 2.330$ in the J1230+34 field. Cyan shadowed regions in each panel show the wavelength coverage of *NB*400. Horizontal red lines correspond to $f_\lambda = 0$. Although BGQSO-A at $z = 2.275$ is a member of objects at $z \sim 2.3$, it satisfies the criteria for BGQSO since we determine the criteria taking PDLAs into account. Note that, BGQSO-A is detected as a LAE in our observation (see Section 2.4.3).

Table 2.4: Numbers of absorber concentrated regions in various volumes

Volume (Mpc^3)	$N_{abs} \geq 3^*$	$N_{abs} \geq 4^\dagger$
30^3	0	0
40^3	3	0
50^3	6	0
60^3	15	1
70^3	27	2

Notes.
* The number of the concentrated region with 3 or more absorbers.
† The number of the concentrated region with 4 ore more absorbers. Note that there are no fields with 5 or more absorbers.

(corresponding to $\sim$120 Mpc in the comoving scale at $z = 2.3$) and reach to the average density at $r \sim 250'$ ($\sim$400 Mpc in the comoving scale at $z = 2.3$). Since the profile of the surface number density is systematically different between absorbers and BGQSOs, we conclude that absorbers are intrinsically clustered, independent of the sky distribution of BGQSOs in each field of absorber concentrated regions.

2.3 Observations and data reduction

2.3.1 Observations

We carried out a wide imaging observations to search for LAEs in the J1230+34 field on the 16th and 17th April 2015 (UT) using Suprime-Cam (Figure 2.8) on the 8.2 m Subaru Telescope (Figure 2.9). Table 2.5 summarizes general information of Suprime-Cam. In our observations, we used both of the NB filter *NB*400 and g'-band filter ($\lambda_{\rm eff} = 4809$ Å and FWHM $= 1163$ Å; Miyazaki et al., 2002). Figure 2.10 shows filter transmission curves of filters used in this study. The NB400 filter can probe the Lyα emission of LAEs at $2.255 < z < 2.330$. During our observing run, the typical seeing sizes (in FWHM) were $0''.7 - 1''.3$ for *NB*400 and $0''.6 - 1''.0$ for g'-band. The total on-source integration time for *NB*400 and g' are 4.6 hrs (300 sec exposure $\times$ 55 shots) and 1.0 hr (120 sec exposure $\times$ 30 shots), respectively.

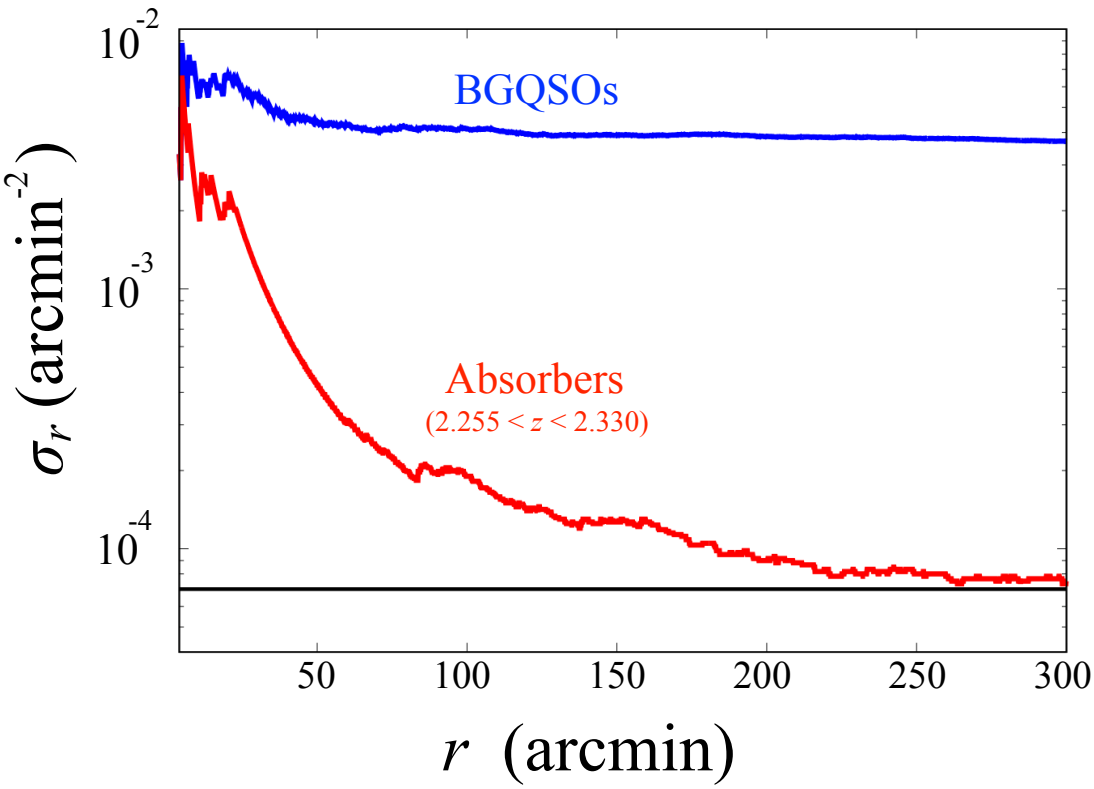

Fig. 2.7: The average surface number density of all 6 absorber concentrated regions, as a function of the radius (r). The vertical axis indicates the surface number density of absorbers and BGQSOs within a circular regions with a radius of r. The red and blue lines show the surface number density of absorbers and BGQSOs, respectively. The black line indicates the average of absorber density calculated for the entire BOSS field.

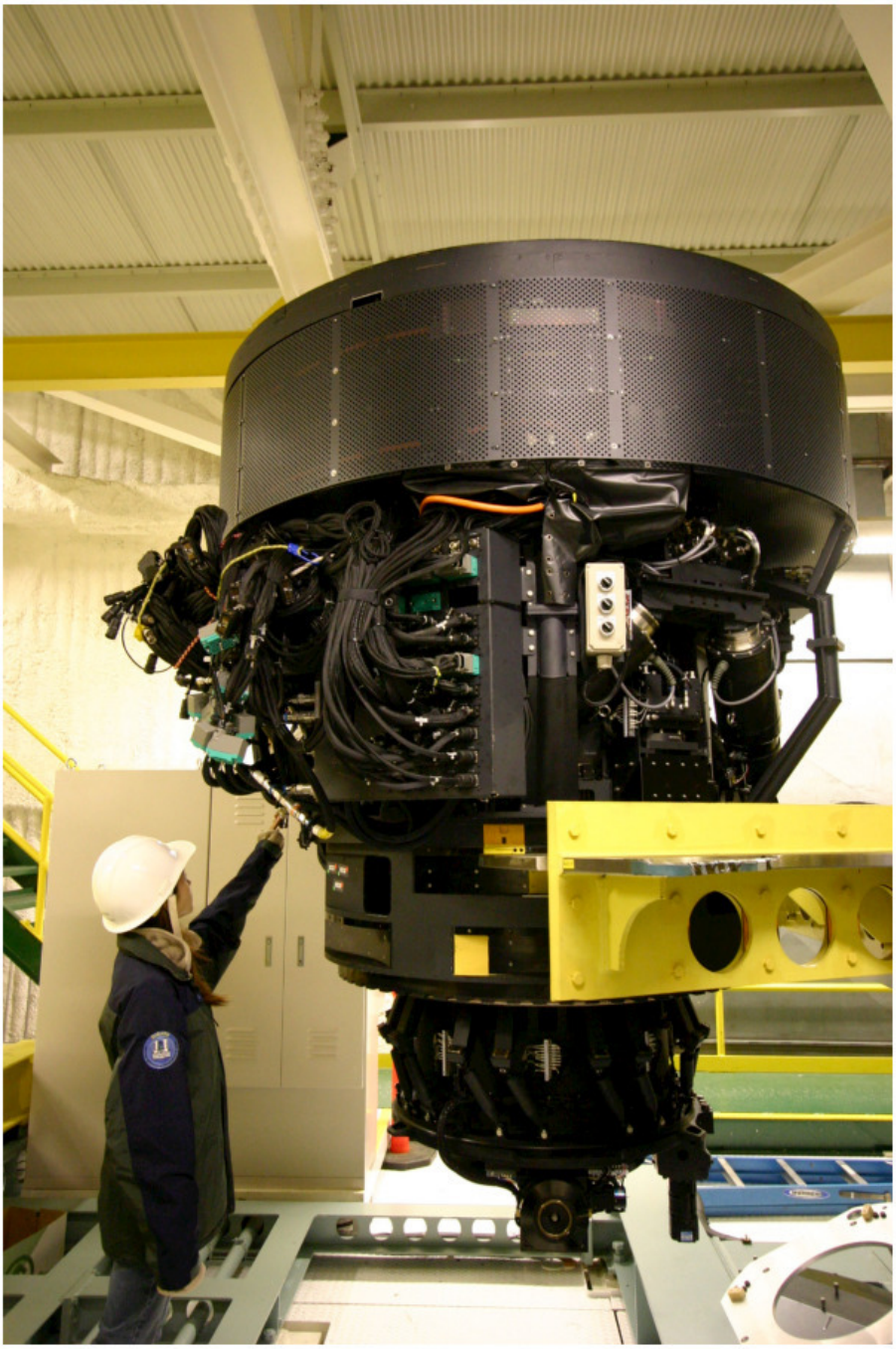

Fig. 2.8: Suprime-Cam on the Subaru telescope (©NAOJ[2]).

[2] https://www.subarutelescope.org/Gallery/j_instrument.html

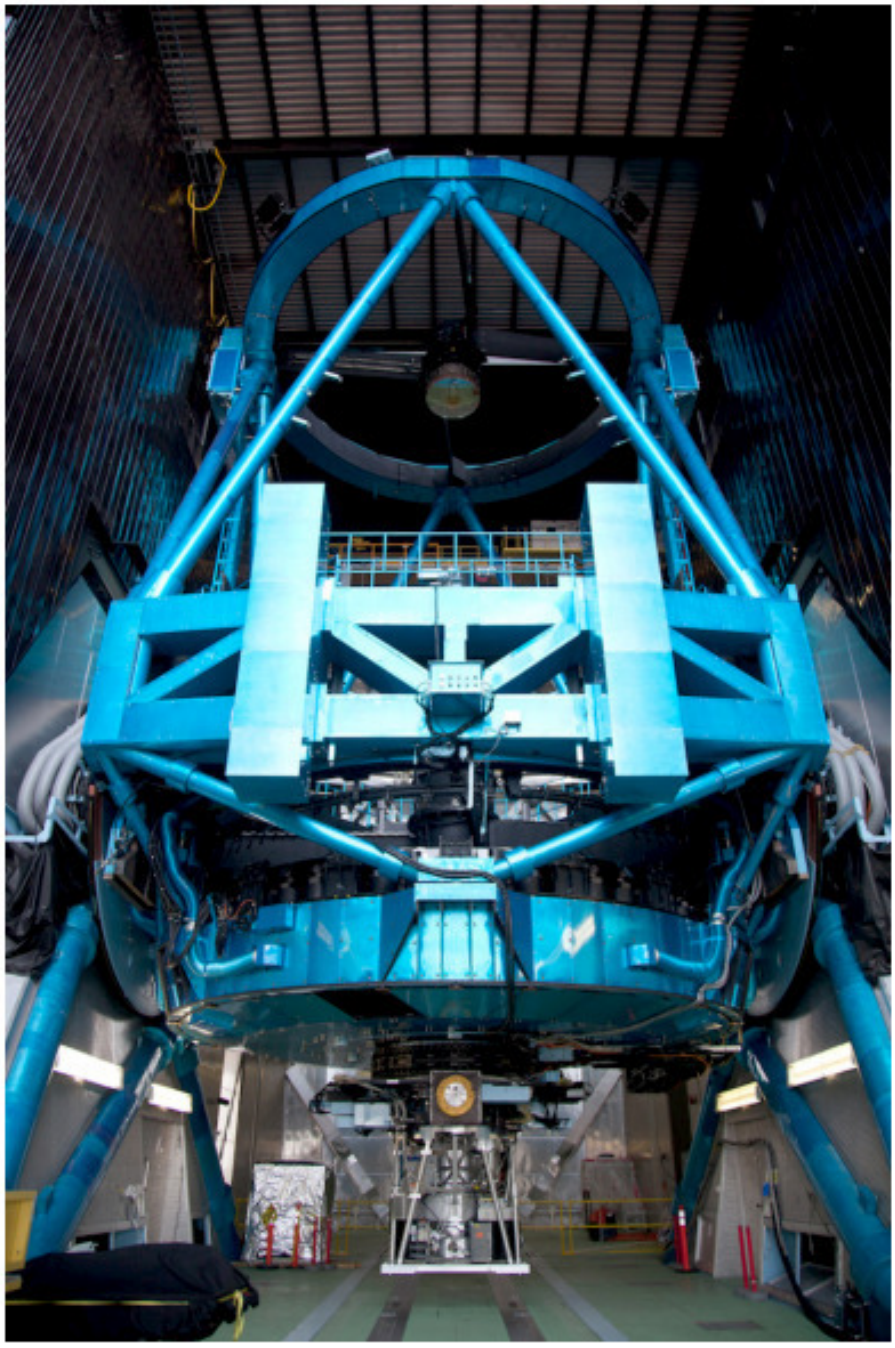

Fig. 2.9: The Subaru telescope (©NAOJ[3]).

[3] https://www.subarutelescope.org/Gallery/j_tele_dome.html

Table 2.5: General information of Subaru/Suprime-Cam

Detectors	Hamamatsu Photonics KK 2048×4096 (S10892-01)
Number of CCDs	10
Pixel size	15 μm
Pixel scale	$0.''20$
Field-of-view	$\sim 34' \times 27'$
Gain	∼2.5-3.7 e^-/ADU
Readout noise	∼10 e^-

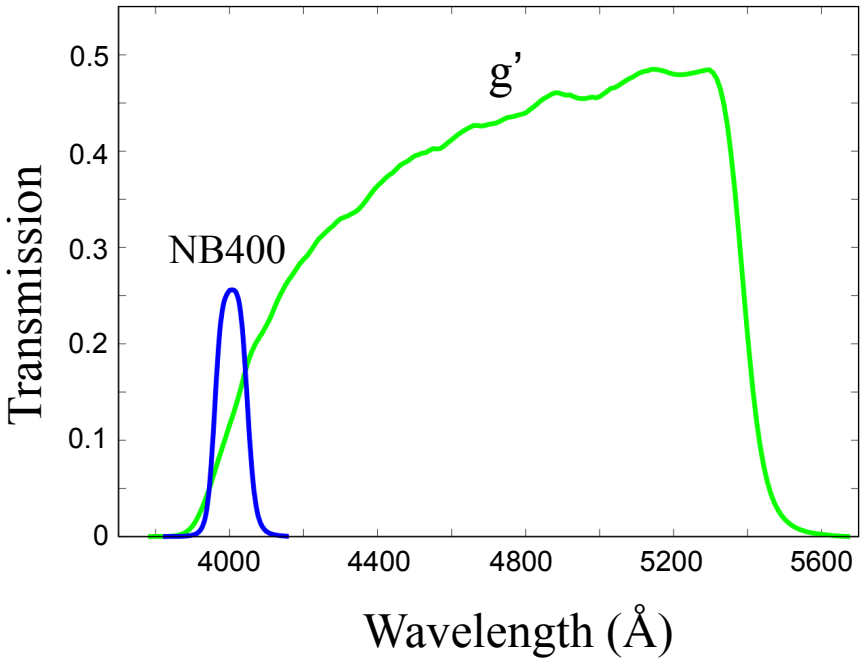

Fig. 2.10: Filter response curves of *NB*400 (blue) g'-band (green). These response curves include not only the filter transmission but also the quantum efficiency of the CCD, reflectivity of the prime mirror of the telescope, transmission of the prime focus corrector, and the transparency of atmosphere assuming sec(z)=1.2 (z is the zenith distance).

Table 2.6: Summary of our observations

Date (UT)	Filter	Individual exposure (sec.)	Number of exposures	Total exposure (hr)	Seeing	5σ limit
2015.4.16-17	$NB400$	300	55	$\sim$4.6	$0.''7 - 1.''3$	25.34
2015.4.16	g'	120	30	$\sim$1.0	$0.''6 - 1.''0$	26.79

2.3.2 *Data reduction*

Subaru/Suprime-Cam is a mosaic CCD camera. This camera has ten CCD chips with 2048 $\times$ 4096 pixels (Figure 2.11). For the data reduction, we mainly used SDFRED2 (Ouchi et al., 2004). In this subsection, we describe the data reduction process with SDFRED2. We followed the standard reduction process that is described in the manual for SDFRED2[4].

Overscan subtraction

First, we subtracted bias and trimmed overscan regions from the obtained frames using a script in SDFRED2, overscansub.csh. In this process, the median value of the overscan region in each line is subtracted as bias. Then the overscan region is trimmed from frames. Figure 2.12 shows an example of frames before and after the subtraction.

Flat fielding

Next, we applied the flat-fielding using "self-flat"[5] frames for both of *NB*400 and g' images. To make flat frames, we use mask_mkflat_HA.csh. The difference in sensitivities between pixels in a flame is corrected by this script. The flat frames are made by taking the median value of each shot and the values in each pixel are normalized to be around unity. Here we set the acceptable normalized value in each pixel for the flat frames to be 0.4 – 1.3, following the recommendation described in the SDFRED2 manual.

Although we took not only the self-flat but also twilight and dome-flat flames (see Figure 2.13), we decide to use the self-flat since twilight and dome flat show some problems. For the twilight-flat images, the readout noise dominate because photon counts are not enough. The value of sky background in the twilight flat flame is $\sim$ 50 ADU. Assuming the gain of $\sim$3.5 e^-/ADU (see Table 2.5), the sky noise is $\sim$13 e^-. Since the readout noise of Suprime-Cam is $\sim$ 10 e^-. and comparable to the sky noise, the readout noise is dominant in our twilight flat flame. In such case, the bias on the images is enhanced and thus it can not be used for the flat-fielding. The twilight flat that we took is not useful also due to the large gradient. In Figure 2.14, we compare *NB*400 mosaic images after the flat-fielding using the twilight-flat frame with that corrected by the self-flat. The image applying the flat fielding using the twilight frat clearly shows irregular background. As for the dome flat, due to the characteristic of the flat lamp of the Subaru telescope, it is known that the flat flame shows some irregular patterns in the short wavelength range ($\lambda < 4000$ Å). Although our dome flat image look a uniform (Figure 2.13) at a glance, we decided not to use it for safety. By considering all of these facts,we make the self-flat frames by stacking the science frames without any shifts. Figure 2.15 shows examples of

[4] `http://subarutelescope.org/Observing/Instruments/SCam/sdfred/v2.0/sdfred2_2p1ae.pdf`

[5] The flat flame made by stacking all the science frames without any shifts (i.e., astronomical objects should disappear in the finally created self-flat image).

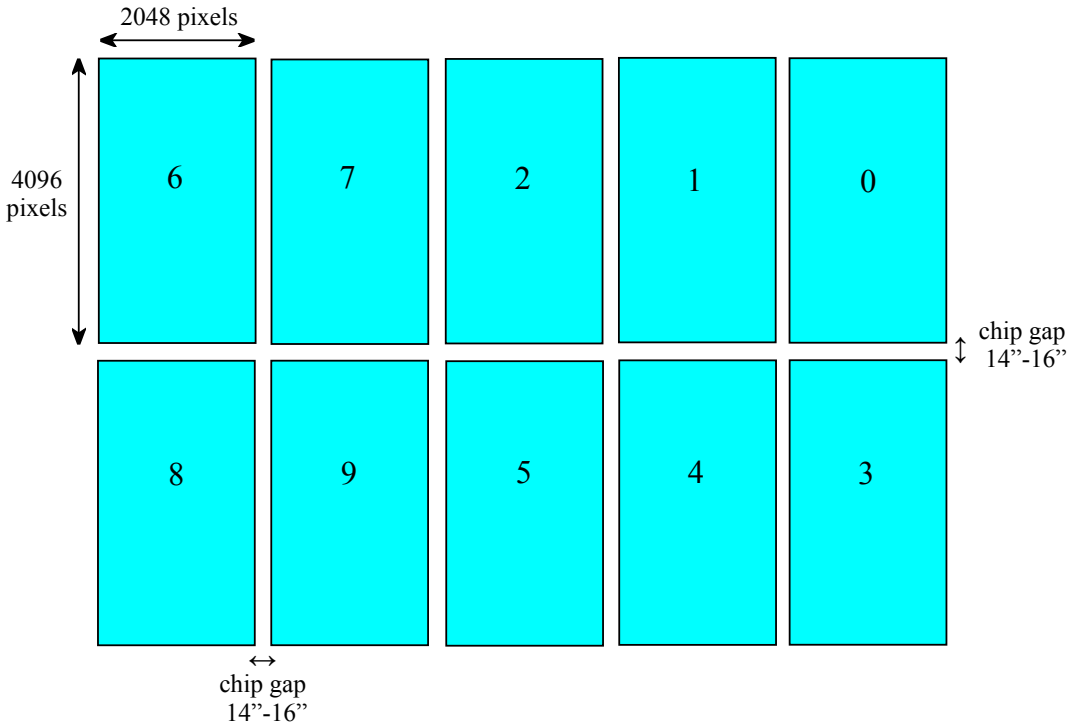

Fig. 2.11: Arrangement of ten CCD chips of Subaru/Suprime-Cam. Each chip has four readout channels.

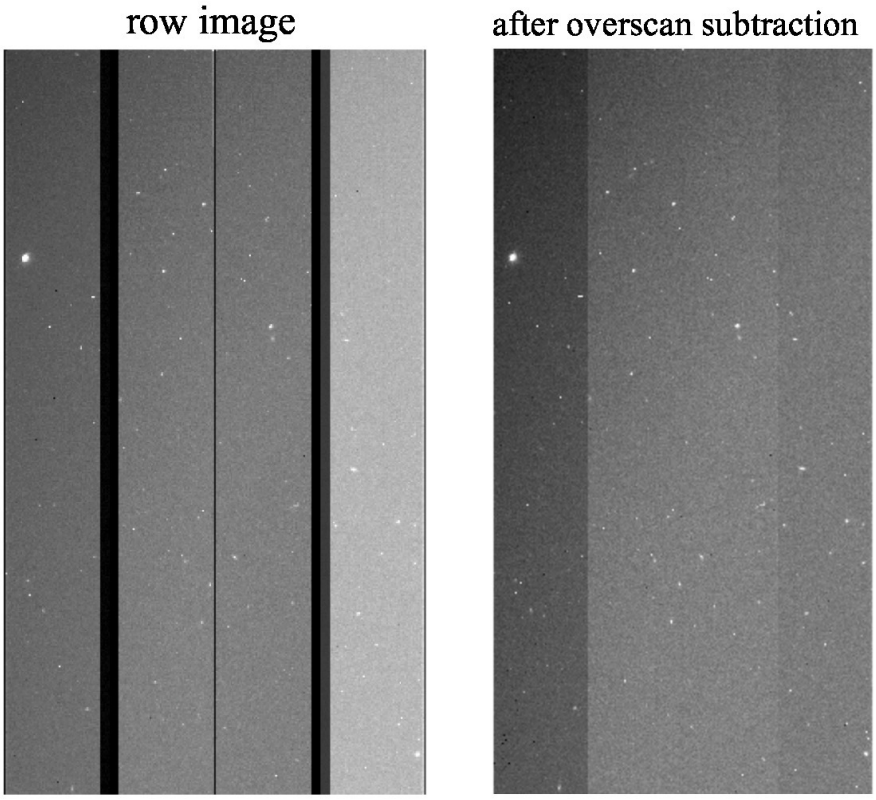

Fig. 2.12: An example of the row image (left) and the frame after the bias subtraction and the overscan trimming (right).

self-flat frames that we use. Although some bright stars do not disappear in the created flames, it is not a problem since we mask such regions in the later process. To apply the flat-fielding, we used ffield.csh in SDFRED2.

Removing cosmic rays

After the flat-fielding, we removed cosmic rays. Generally, cosmic rays disappear after stacking enough number of frames. However, in the case of our *NB*400 images, we can not stack and match frames without removing cosmic rays. This is because of the following two reasons, (1) significant number of cosmic rays are in the *NB*400 images due to relatively long exposure time, and (2) since the wavelength range of *NB*400 is narrow, signals from astronomical objects are faint and difficult to distinguish from cosmic rays. We used a publicly-available script, the L.A.Cosmic (van Dokkum, 2001) to remove cosmic rays.

Corrections for the distortion and the atmospheric dispersion

Due to the telescope optics and the differential atmospheric dispersion, images are distorted. The distortion is significant specially in the case of the observations with Suprime-Cam because of its wide FoV. We corrected such a distortion with distcorr.csh. Figure 2.16 shows an example of flames before and after applying the distortion correction.

The PSF size measurement

With fwhmpsf_batch.cs, we measured the PSF size of stellar objects in each chip in each frame. Here we measured the PSF size of 50 point sources per each chip in each shot. Figures 2.17 and 2.18 show the frequency distribution of the average PSF size in each chip. Based on the PSF measurement, we discarded some frames due to the bad seeing. Specifically, we remove 14 shots with PSF $> 1.0''$ and two shots with PSF $> 0.7''$ from *NB*400 and g' images, respectively. Consequently, we used 41 frames (corresponding to $\sim$3.4 hrs) and 28 frames ($\sim$0.9 hrs) of *NB*400 and g'-band images for making the stacked images.

The sky background subtraction

We then subtracted the sky background with skysb.sch. Here mesh size for determining the background count is a free parameter. To determine the mesh size, we visually checked the sky subtracted images by applying three mesh sizes. In Figures 2.19 and 2.20, we show the mosaic images after applying various values (32, 64, 100 pixels for *NB*400 and 32, 64, and 128 pixels for g') for sky mesh. We check the sky subtracted images by eye. In the case that we apply the mesh size of 32 pixels, both of *NB*400 and g' images show irregular background. On the other hand, the images adopting the largest sky mesh (100 pixels for *NB*400 and 128 pixels for

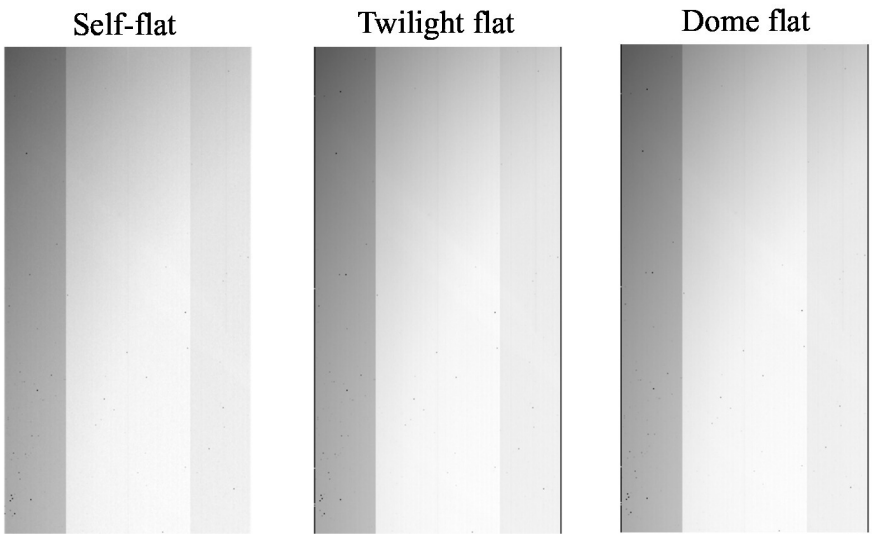

Fig. 2.13: Example of the self, twilight, and dome flat frames (g'-band, chip 6 chihiro).

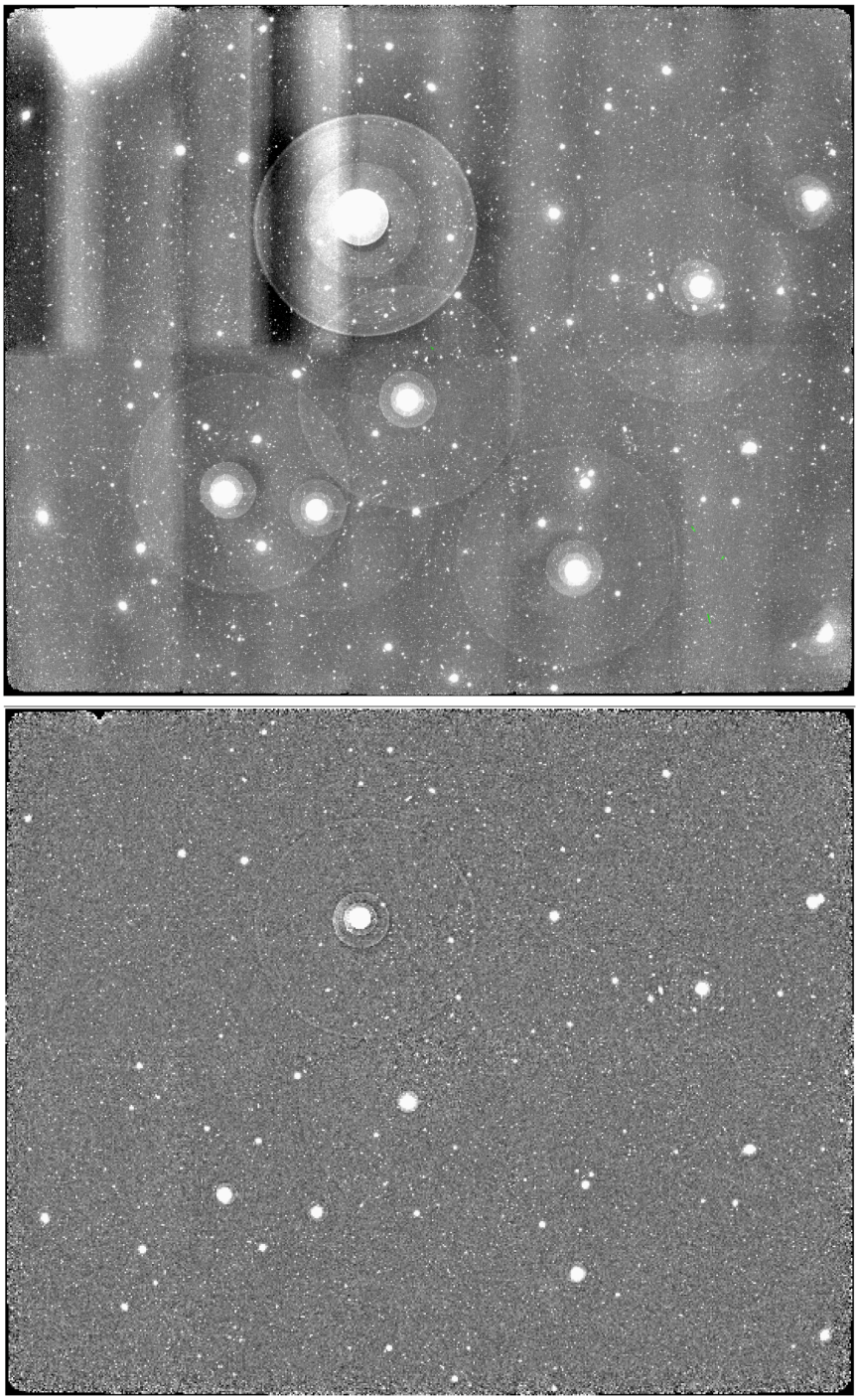

Fig. 2.14: *NB*400 mosaic images after applying the flat-fielding by using the twilight-flat frame (the upper image) and self-flat (the lower image). The background in the image corrected by the twilight-flat shows irregular bumps clearly.

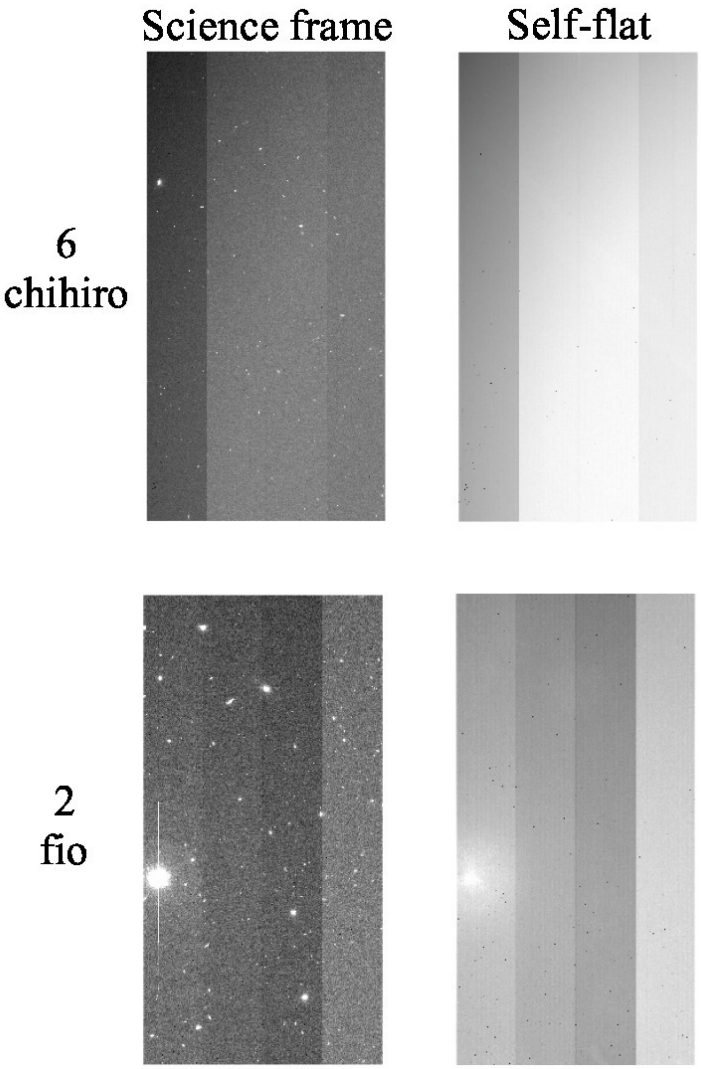

Fig. 2.15: Examples of self-flat frames (g'-band, chip 6 chihiro and chip 2 fio). Left images are science flames used to make flat frames and images in the right side are flat frames. As shown in the flat frame of chip 2 fio, a remarkable feature caused by a bright star does not completely disappear in the flat image.

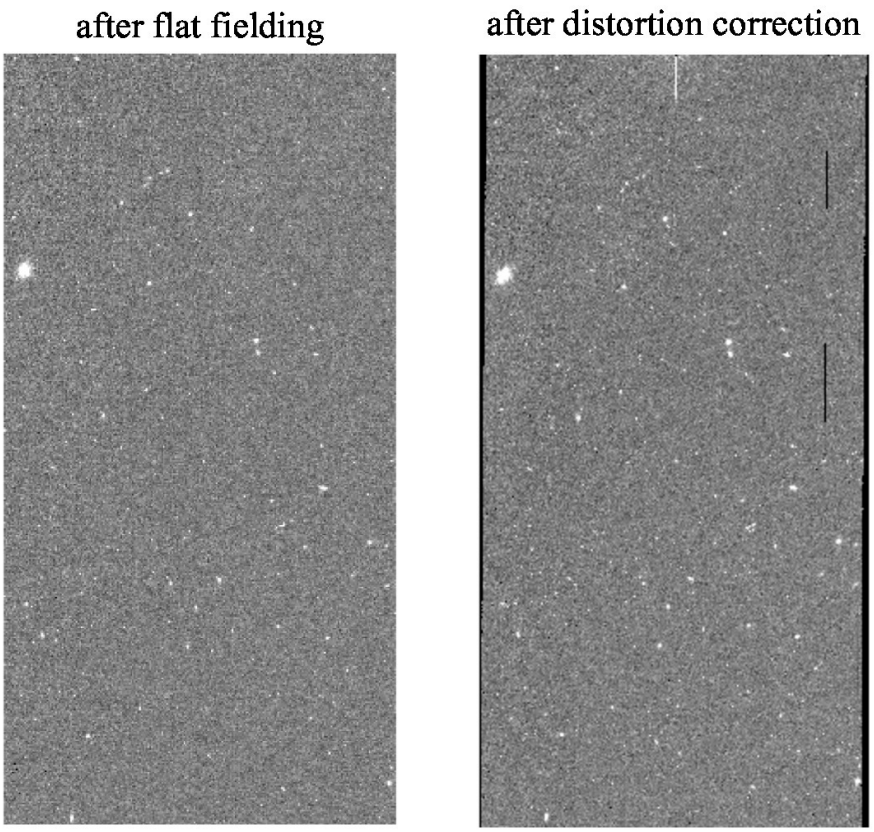

Fig. 2.16: An example of distortion corrected images (Right). The left image is before the distortion correction (i.e., after removing cosmic rays). The corrected image is distorted several pixels. This is remarkable around edges of the image.

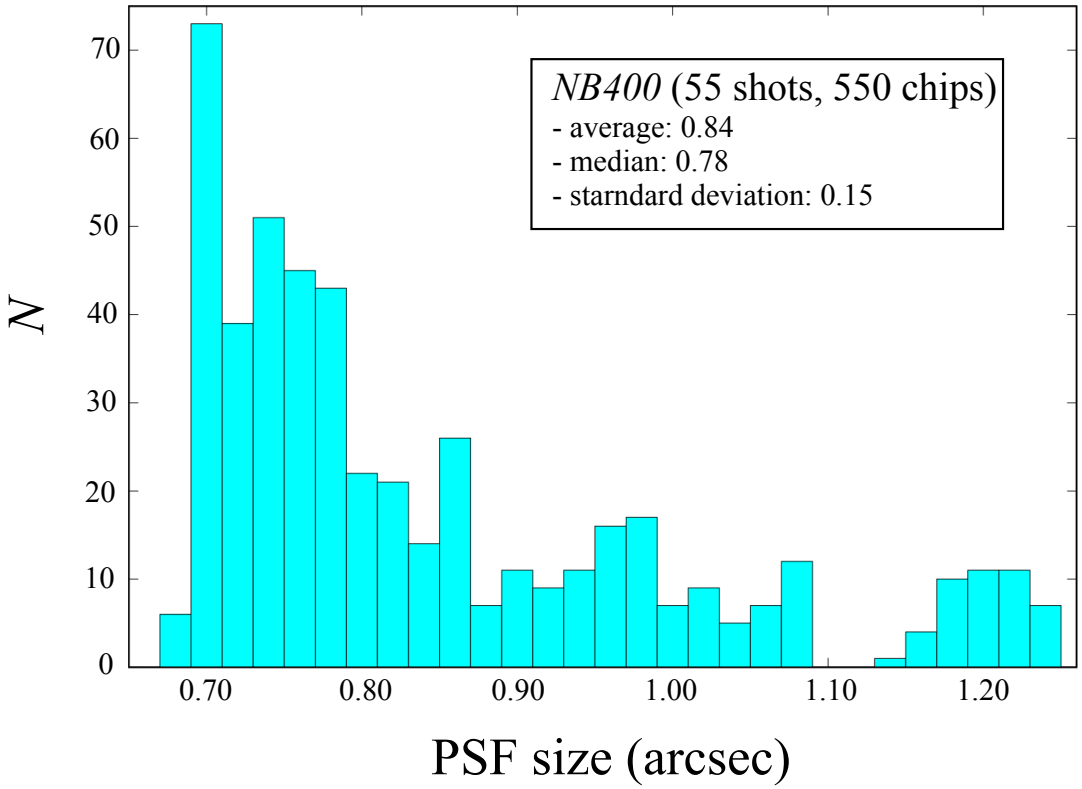

Fig. 2.17: Frequency distribution of the average PSF size in each chip of the *NB*400 image. We took 55 shots of *NB*400 frames and each frame has 10 chips. We measure the PSF size of stellar object in 550 chips in total.

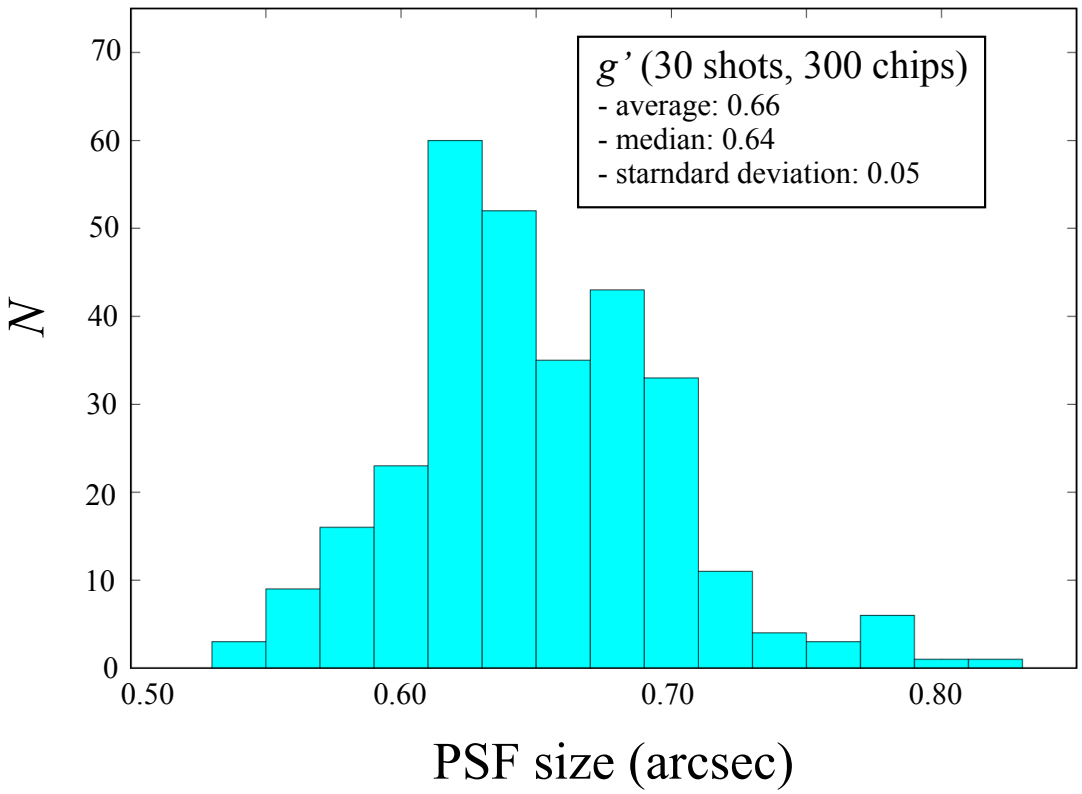

Fig. 2.18: Frequency distribution of average PSF size in each chip of the g'-band image. We took 30 shots of g'-band frames and each frame has 10 chips. We measure the PSF size of stellar object in 300 chips in total.

g') show larger and clearer halos around bright stars. Therefore we adopt 64 pixels for both of $NB400$ and g' images.

Making mosaic images

After subtracting the sky background, we made the mosaic images. The script used for estimating alignment and flux scaling between different flames is makemos.csh. This script determines the shifts, rotations, and flux scales, by comparing stellar objects common to different images. Then we made mosaic images with imcio2a by calculating the median values. After generating the mosaic images, we masked some regions affected by bright stars in either the $NB400$ or the g' images (see Figures 2.22 and 2.23) using blank.csh and circular_blank.csh.

The astrometry, position matching, and the PSF matching

For the astrometry, we calibrated the coordinate in the J1230+34 field based on the USNO-B1 catalog (Monet et al., 2003). Here, we use SExtractor (Bertin & Arnouts, 1996) version 2.5.0 and WCSTools (Mink, 2002) version 3.9.5. After detecting objects with SExtractor, detected objects are matched to objects in the USNO-B1 catalog and the coordinate is corrected with imwcs in WCSTools. 200 objects are used for the matching. Then we matched the position between the $NB400$ and g' image using some tasks of IRAF[6]. The matching process is as follows. (1) with xyxymatch, we match positions of stellar object in each image, (2) estimating how much we should shift the image with geomap, and (3) shifting g' image to match the $NB400$ image with geotran. The position matching is necessary to detect objects and to make photometry in the same position both in $NB400$ and g'-band images. After the position matching, we smoothed the g'-band image so that the PSF size of stars was matched to that of $NB400$ image with a IRAF task, psfmatch. The stellar PSF size of the smoothed image is $\sim 0''.9$.

The flux calibration

For the flux calibration, we used SDSS (DR12) spectroscopic stars within the observed field. We convolved transmission curves of $NB400$ and g' filters and spectra of 5 SDSS stars (Table 2.7) to estimate the photometric zero point. We measured the photometric zero point based on synthetic magnitudes ($NB400_{\rm syn}$ and $g'_{\rm syn}$ in Table 2.7) of those SDSS stars. For the calibration, we used the average of zero points measured using those 5 SDSS stars. The zero point magnitudes per 1 second exposure in $NB400$ and g' are 29.77 and 32.44, respectively. Figure 2.21 shows the specta of SDSS stars used for the flux calibration.

[6]The IRAF is distributed by the National Optical Astronomy Observatories, operated by the Association of Universities of Research in Astronomy, Inc., under contract to the National Science Foundation of the United States.

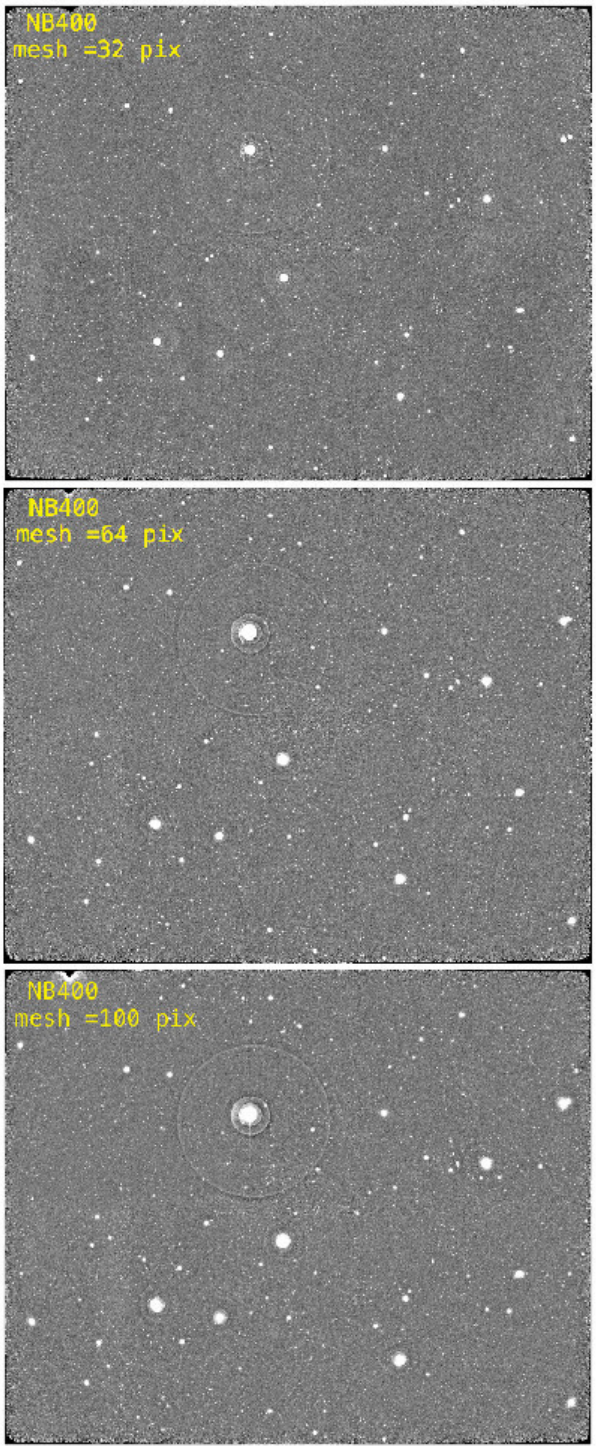

Fig. 2.19: Mosaic images of *NB*400 when we apply the mesh size for the sky subtraction of 32, 64, 100 pixels, from top to bottom. Note that, in the case with 128 pixels mesh, the matching failed.

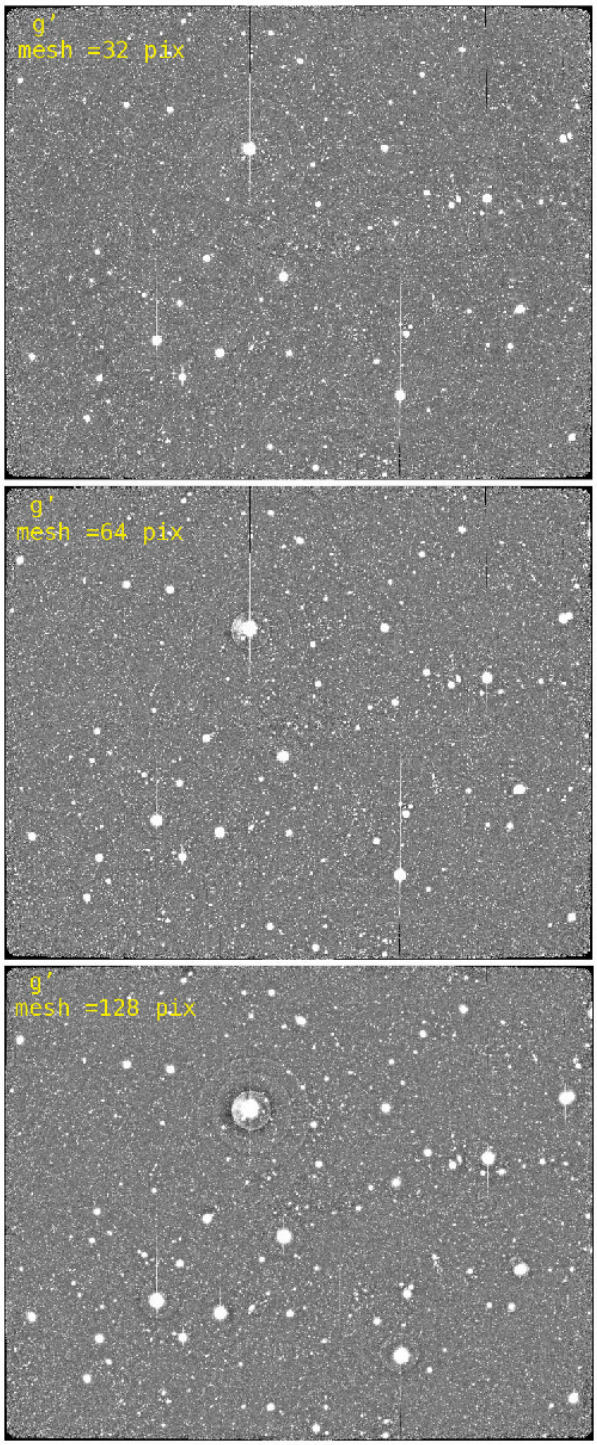

Fig. 2.20: Mosaic images of g' when we apply he mesh size for the sky subtraction of 32, 64, 128 pixels, from top to bottom.

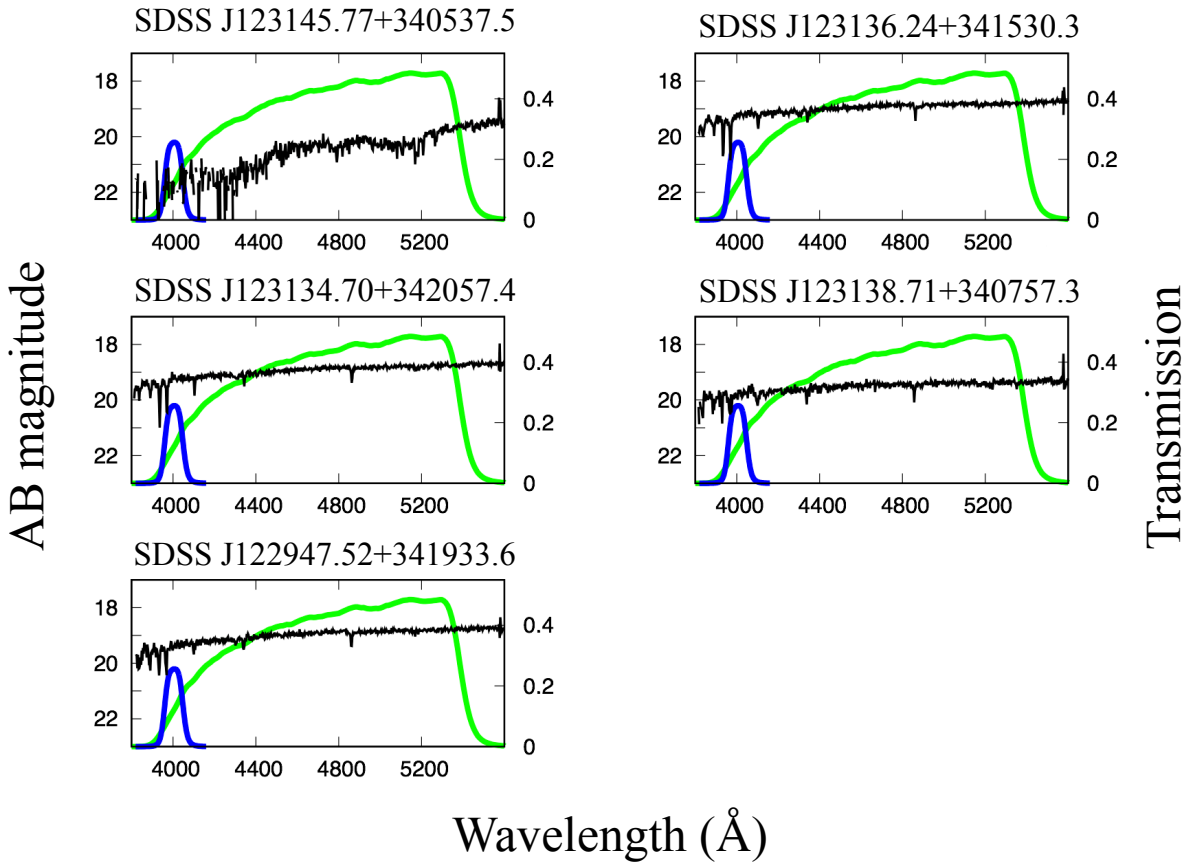

Fig. 2.21: SDSS spectra of the stars used for the flux calibration. Blue and green curves show the filter transmission of $NB400$ and g'-band, respectively.

Table 2.7: The SDSS stars used for the flux calibration

Name	g'_{model} *	g'_{syn} †	$NB400_{\mathrm{syn}}$
SDSS J123145.77+340537.5	20.44	20.36	21.91
SDSS J123136.24+341530.3	18.93	18.93	19.33
SDSS J123134.70+342057.4	18.92	18.90	19.31
SDSS J123138.71+340757.3	19.54	19.48	19.84
SDSS J122947.52+341933.6	18.97	18.95	19.43

Notes.
* g'_{model} is the model magnitude measured in SDSS.
† g'_{syn} and $NB400_{\mathrm{syn}}$ are the synthetic magnitudes determined by convoluting the filter response curves and spectra of each star.

The final images

We show the final images of $NB400$ and g'-band in Figures 2.22 and 2.23, respectively. The FoV of the reduced image is $\sim 34'.12 \times 26'.33$, which is roughly corresponding to ~ 55 Mpc $\times$ 43 Mpc in the comoving scale at $z = 2.3$. The area of the final image except for the masked regions is ~ 754 arcmin^2. The width of the NB400 wavelength coverage corresponds to $\sim$95 Mpc, and thus the surveyed volume is $\sim 1.9 \times 10^5$ Mpc^3 in the comoving scale at $z = 2.3$.

The photometry and the object detection

We used SExtractor (version 2.5.0) for the source detection and the photometry. We made the object detection and photometry in the double-image mode. Objects are detected on the $NB400$ image adopting the criterion that astronomical objects had to be 12 or more continuous pixels above the 3σ background fluctuation. Then we made the photometry in each image by employing a circular aperture with a diameter of $2''$, centered on the positions of the objects detected in the $NB400$ image. The 5σ detection limits in the $2''$ aperture for the $NB400$ and g' images are 25.34 and 26.79, respectively.

2.4 Results

2.4.1 Color selection of LAEs

We select LAEs at $z = 2.3$ based on the color-magnitude diagram, $g' - NB400$ vs. g' (Figure 2.24). The adopted color criteria are as follows:

1. $g' - NB400 \geq 0.52$,
2. $NB400 \leq 25.34$
3. $g' - NB400 \geq -0.23 + 3\sigma(NB400 - g')$

The first criterion corresponds to the rest-frame equivalent width EW_0 of 20 Å at $z = 2.3$. The second one is the 5σ limiting magnitude for $NB400$. The offset of -0.23 in the third criterion corresponds to the median color of the detected objects in the magnitude range of $24.0 < NB400 < 25.0$ except for the LAE candidates. This offset is needed because $NB400$ covers very shorter wavelength side in the wavelength coverage of g'-band as shown in Figure 2.10. The offset corresponds to the slope of the spectral energy distributions of objects without Lyα emissions ($EW_0 > 20$ Å). The color error, $3\sigma(NB400 - g')$ is determined as

$$3\sigma(NB400 - g') = -2.5\log[1 - \sqrt{(f^2_{3\sigma,NB400} + f^2_{3\sigma,g'})}/f_{3\sigma,NB}] \tag{2.1}$$

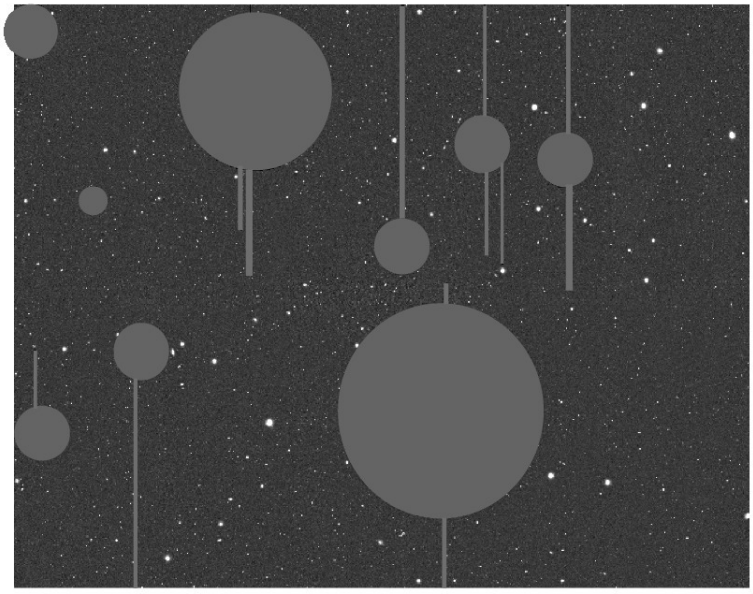

Fig. 2.22: The reduced image of the J1230+34 field in *NB*400 (north is up). Gray filled circles and connected thin bars show masked regions.

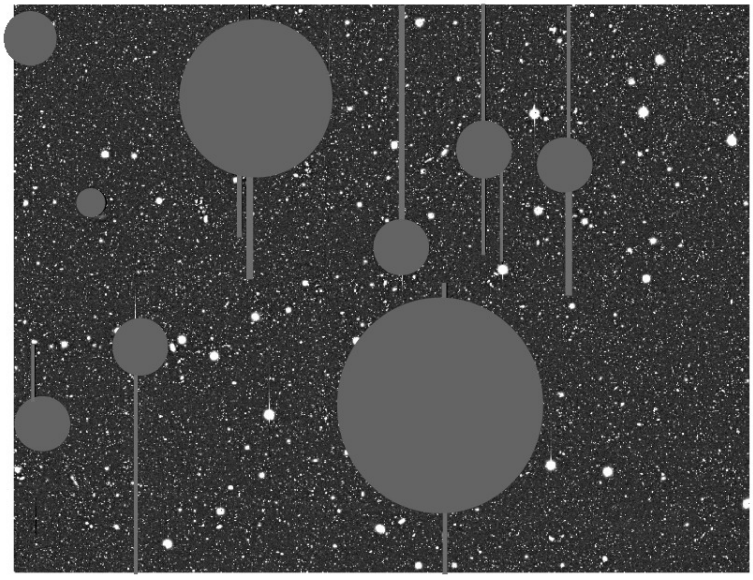

Fig. 2.23: The reduced image of the J1230+34 field in g'-band (north is up). Gray filled circles and connected thin bars show masked regions.

(e.g., Shioya et al., 2008). Then, we have selected 154 objects as LAE candidates at $z = 2.3$. After the visual inspection, the final sample consists of 149 LAE candidates. Since we are focusing on the very short wavelength range ($\sim$ 4000 Å) in optical, our sample is free from the contamination by [O III] emitters which could often be interlopers for high-z LAEs. The possible contaminants in our sample are [O II]-emitting galaxies at $z \sim 0.07$, but such contamination is expected to be negligibly small based on the following considerations. Given the 5σ detection limit of the $NB400$ image and the NB-excess criterion for EW_0 ($g' - NB400 \geq 0.52$), the limiting [O II] luminosity at $z \sim 0.07$ is $\sim 1.6 \times 10^{38}$ erg s^{-1}. The surveyed volume is 550 Mpc^3 in the comoving scale at $z \sim 0.07$. From the luminosity function (LF) of [O II] emitters reported in Ciardullo et al. (2013), we obtain an expected number, $\sim$30 [O II] emitters. Ciardullo et al. (2013) also reported that the distribution of EW_0 of [O II] emitters at $z < 0.2$ shows its peak around 5 Å, and rapidly decreases with the e-folding length of $w_0 = 8$ Å. We set the criterion of EW_0 for LAEs at $z \sim 2.3$ as $EW_0 = 20$ Å. This corresponds to $EW_0 \sim 60$ Å for [O II] emitters at $z \sim 0.07$. Based on this, the fraction of [O II] emitters with $EW_0 > 60$ Å is only 0.055% and the expected number of [O II] emitters is ~ 0.018. Thus we conclude that the contamination by [O II] emitters is negligible, and we regard these 149 $NB400$-excess objects as LAEs at $2.255 < z < 2.330$. Table 2.8 shows the general properties of all 149 detected LAEs in the J1230+34 field (See Appendix A for the images of detected LAEs). Konno et al. (2016) also estimated the contamination of [O II] emitters at $z \sim 0.04$ for LAEs at $z \sim 2.2$ in their NB survey using Suprime-Cam at a similar wavelength, based on the luminosity function and EW_0 distribution of [O II] emitters from Ciardullo et al. (2013). Their surveyed volume is $\sim 1.22 \times 10^3$ Mpc^3 and the expected number of [O II] emitters at $z \sim 0.04$ is ~ 0.03. Taking the difference of the surveyed volume into account, our conclusion is consistent with that of Konno et al. (2016) in the sense that the contamination of [O II] emitters in Suprime-Cam LAE surveys at $z \sim 2$ is negligible. We show their sky distribution in Figure 2.25.

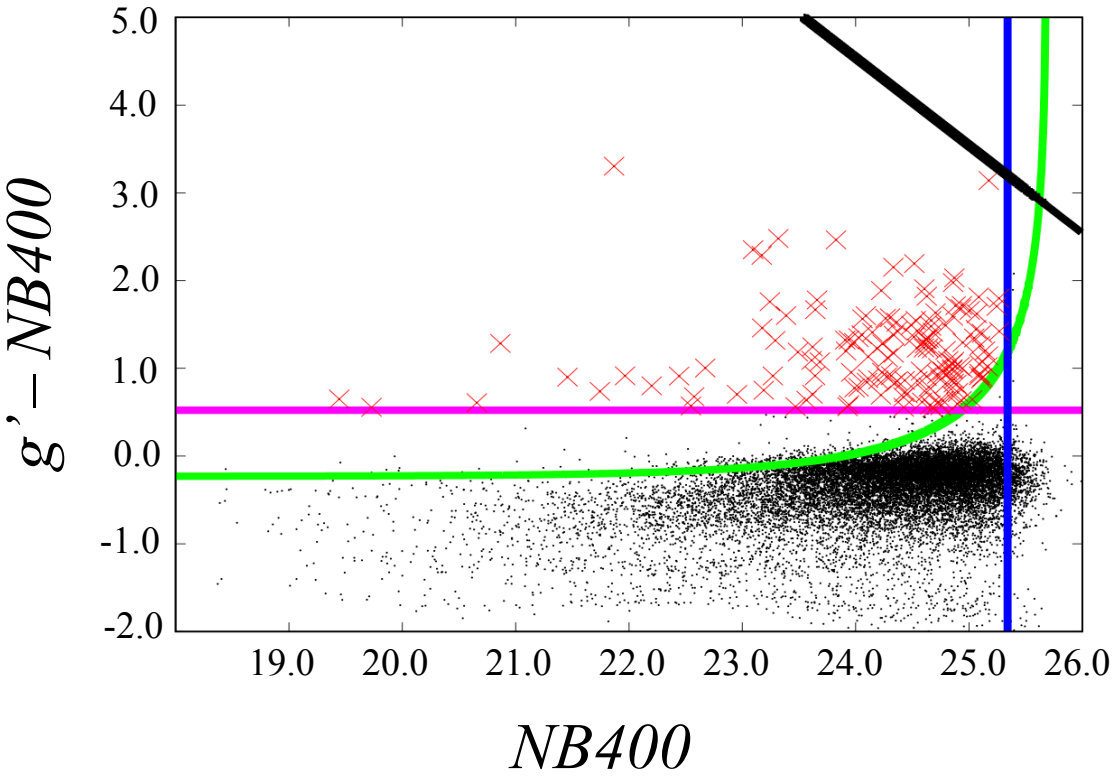

Fig. 2.24: $g' - NB400$ vs. g' color-magnitude diagram. The $g' - NB400$ color is based on the aperture fixed ($2''$) photometry. The horizontal axis indicate $NB400$ magnitude from Kron photometry. The colored lines indicate the selection criteria for LAEs. The magenta line indicates $g' - NB400 = 0.522$ which corresponds to $EW_0 = 20$ Å. The green curve shows the 3σ error in the $g' - NB400$ color. The blue line shows the 5σ limiting magnitude of $NB400$. Red crosses denote the selected LAEs. The black line corresponds to the 1σ limiting magnitude of the g' image.

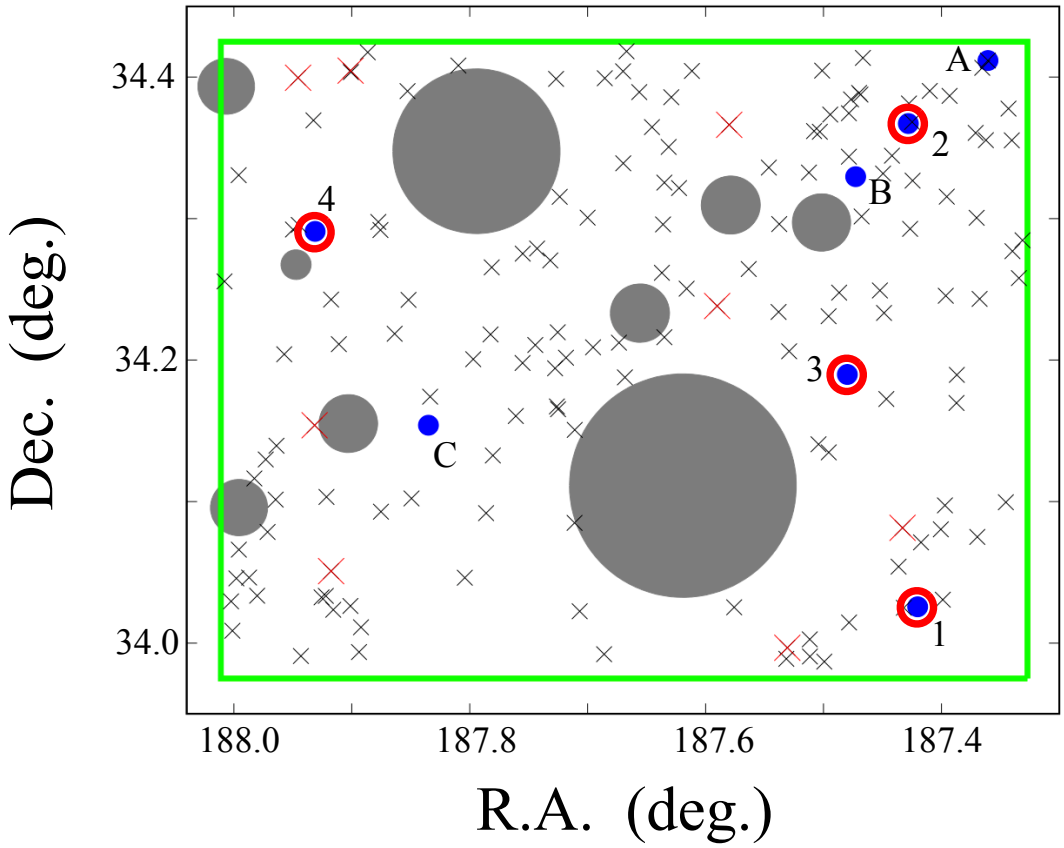

Fig. 2.25: The sky distribution of BGQSOs (blue filled circles) and LAEs (black crosses) in the J1230+34 field. The green box shows the field-of-view of Suprime-Cam ($34' \times 27'$). The BGQSOs with surrounding red circles have absorbers at $2.255 < z < 2.330$. LAEs shown by large red crosses have Lyα $EW_0 > 200$ Å. Masked regions are shown by gray filled circles. IDs for absorbers and BGQSOs are the same as those in Figure 2.1.

Table 2.8: General properties of the detected LAEs

ID	R.A. (deg.)	Dec. (deg.)	$NB400^*$ (ap)	$NB400^\dagger$ (AUTO)	g'^* (ap)	$g'^\dagger$ (AUTO)	EW_0 (Å)	$\log L_{\mathrm{Ly}\alpha}{}^\ddagger$ (erg s^{-1})	$\log L_{\mathrm{cont}}{}^\S$ (erg s^{-1})
1	187.3607	34.4118	19.60	19.44	20.25	20.09	26.4	44.29	45.35
2	187.6670	34.4182	19.89	19.73	20.45	20.29	21.5	44.13	45.27
3	187.9431	33.9908	21.80	20.87	23.09	22.65	76.0	43.98	44.28
4	187.6116	34.4043	21.67	21.46	22.57	22.37	42.2	43.59	44.43
5	187.3623	34.3554	21.93	21.74	22.67	22.51	31.4	43.42	44.38
6	187.9011	34.4046	23.08	21.87	26.39	24.11	1381.4	43.61	43.66
7	187.4766	34.3843	22.63	21.97	23.55	22.71	43.3	43.33	44.30
8	187.7552	34.1980	22.33	22.20	23.13	23.02	35.4	43.26	44.17
9	187.9959	34.3307	22.85	22.44	23.76	23.52	43.0	43.24	43.96
10	187.4993	33.9869	22.66	22.55	23.23	23.12	22.2	43.01	44.13
11	187.9802	34.0335	23.24	22.67	24.24	23.85	50.1	43.17	43.83
12	187.3988	34.0307	23.28	22.95	23.98	23.49	29.5	42.83	43.99
13	187.4330	34.0814	23.20	23.10	25.55	25.37	308.1	43.12	43.15
14	187.4784	34.3745	23.31	23.18	24.77	24.66	97.0	43.02	43.49
15	187.6684	34.1879	23.29	23.19	24.04	23.89	32.2	42.82	43.83
16	187.7550	34.2752	23.71	23.24	25.47	24.08	143.7	42.85	43.75
17	187.8519	34.2426	24.18	23.27	25.09	24.27	43.1	42.89	43.67
18	187.6225	34.3216	23.67	23.29	24.99	24.58	79.8	42.94	43.53
19	187.5902	34.2382	23.54	23.32	26.01	25.84	365.3	43.04	42.93
20	187.9730	34.1298	23.82	23.47	24.39	23.90	21.9	42.54	43.83
21	187.4866	34.2476	23.79	23.49	24.98	24.48	66.0	42.80	43.58
22	187.3654	34.4066	23.87	23.57	24.51	24.14	25.7	42.60	43.73
23	187.5042	34.1405	23.87	23.61	24.96	24.77	57.3	42.79	43.46
24	187.5464	34.3361	23.89	23.62	24.59	24.34	29.6	42.65	43.65
25	187.5011	34.4046	23.93	23.62	25.18	25.00	71.8	42.83	43.36
26	187.7444	34.2107	24.08	23.64	24.99	24.64	43.2	42.74	43.52
27	187.6698	34.3391	23.88	23.64	25.55	25.36	127.8	42.86	43.20

ID	R.A. (deg.)	Dec. (deg.)	$NB400^{*}$ (ap)	$NB400^{\dagger}$ (AUTO)	g'^{*} (ap)	$g'^{\dagger}$ (AUTO)	EW_0 (Å)	$\log L_{\mathrm{Ly}\alpha}{}^{\ddagger}$ (erg s^{-1})	$\log L_{\mathrm{cont}}{}^{\S}$ (erg s^{-1})
28	187.9007	34.4035	24.41	23.66	26.19	26.17	147.4	42.91	42.80
29	187.9450	34.2956	24.30	23.68	25.37	24.93	55.8	42.78	43.39
30	187.5307	33.9967	24.88	23.83	27.35	25.37	357.7	42.77	43.20
31	187.9110	34.2112	24.16	23.91	25.48	25.30	80.2	42.71	43.24
32	187.8752	34.0928	24.13	23.91	25.32	25.19	67.0	42.69	43.29
33	187.7814	34.2656	24.21	23.93	24.77	24.65	21.8	42.53	43.52
34	187.9257	34.0323	24.31	23.94	25.64	25.41	80.5	42.71	43.19
35	187.7184	34.2017	24.80	23.94	25.39	25.06	23.0	42.65	43.35
36	187.5635	34.2644	24.62	23.96	25.58	24.80	46.1	42.56	43.46
37	187.3312	34.2847	24.28	23.99	25.58	25.11	77.2	42.63	43.33
38	187.6861	33.9921	25.05	23.99	25.83	24.54	33.8	42.42	43.57
39	187.9715	34.0785	24.31	24.03	25.66	25.44	83.3	42.67	43.18
40	188.0012	34.0087	24.47	24.03	25.25	24.91	34.3	42.55	43.41
41	187.4266	34.2928	24.82	24.05	26.20	24.36	87.4	42.19	43.64
42	187.5375	34.2962	24.23	24.06	25.79	25.52	111.4	42.66	43.15
43	187.5124	34.3325	24.37	24.09	25.97	25.43	116.7	42.63	43.19
44	187.6700	34.4041	24.40	24.10	25.24	24.98	38.1	42.52	43.38
45	187.4099	34.3902	25.00	24.11	25.88	25.09	41.0	42.55	43.34
46	187.8528	34.3902	24.66	24.11	25.80	25.26	61.0	42.59	43.27
47	187.6350	34.2161	24.31	24.15	25.72	25.53	90.6	42.61	43.15
48	187.6361	34.2959	24.28	24.19	25.51	25.43	70.2	42.57	43.19
49	187.3404	34.3553	24.47	24.20	25.34	25.01	39.9	42.46	43.38
50	187.4419	34.3444	24.70	24.22	25.40	25.24	28.9	42.51	43.28
51	187.7267	34.3988	24.39	24.23	26.28	25.79	169.3	42.61	43.04
52	187.4275	34.3814	24.33	24.23	25.29	25.16	46.2	42.48	43.31
53	187.9499	34.2923	24.47	24.24	25.75	25.63	75.5	42.58	43.11
54	187.8865	34.4176	24.53	24.26	26.10	25.17	112.2	42.46	43.31
55	187.5079	34.3618	24.55	24.27	25.45	25.13	42.3	42.44	43.33
56	187.9157	34.0236	24.58	24.28	25.70	25.48	60.0	42.53	43.17

ID	R.A. (deg.)	Dec. (deg.)	$NB400^{*}$ (ap)	$NB400^{\dagger}$ (AUTO)	g'^{*} (ap)	$g'^{\dagger}$ (AUTO)	EW_0 (Å)	$\log L_{\mathrm{Ly}\alpha}{}^{\ddagger}$ (erg s^{-1})	$\log L_{\mathrm{cont}}{}^{\S}$ (erg s^{-1})
57	187.4486	34.2334	24.61	24.30	26.19	25.95	113.1	42.59	42.97
58	187.4244	34.3269	24.49	24.31	25.41	25.29	43.3	42.46	43.26
59	187.9455	34.3996	24.65	24.33	26.80	25.72	238.0	42.54	43.07
60	187.5030	34.3613	24.65	24.34	25.82	25.77	64.7	42.55	43.05
61	187.3695	34.0751	24.68	24.34	26.05	25.26	86.6	42.44	43.27
62	187.9646	34.1014	24.77	24.35	25.61	25.31	37.9	42.45	43.25
63	187.7000	34.3007	24.95	24.36	26.48	26.59	105.8	42.61	42.67
64	187.7861	34.0918	24.60	24.37	26.03	25.49	92.5	42.48	43.17
65	187.5117	34.0027	24.64	24.37	25.50	25.08	39.0	42.35	43.35
66	187.6370	34.2617	24.85	24.42	25.52	24.91	27.8	42.21	43.42
67	187.3963	34.2455	24.88	24.42	25.44	24.77	21.5	42.08	43.48
68	187.5380	34.2341	24.75	24.43	25.47	25.17	30.6	42.34	43.31
69	187.3344	34.2580	24.76	24.43	25.63	25.53	39.6	42.45	43.16
70	187.7250	34.1653	24.90	24.46	25.61	25.11	29.9	42.29	43.34
71	187.3701	34.3006	25.02	24.49	26.51	25.34	100.9	42.35	43.24
72	187.8493	34.1022	24.97	24.52	26.33	25.11	84.3	42.23	43.34
73	187.9175	34.0508	24.58	24.52	26.77	26.34	250.8	42.52	42.80
74	187.3931	34.3867	24.85	24.53	26.40	26.03	108.8	42.48	42.94
75	187.3954	34.3155	24.68	24.54	25.91	25.21	70.4	42.26	43.30
76	187.4363	34.0541	24.63	24.54	26.06	25.96	92.8	42.46	42.97
77	187.5292	34.2062	24.72	24.54	25.57	25.29	39.3	42.29	43.27
78	187.9214	34.1033	24.98	24.58	25.95	25.26	47.2	42.25	43.28
79	187.8096	34.4083	24.69	24.59	25.31	25.25	24.6	42.24	43.28
80	187.6291	34.3858	24.97	24.60	26.20	25.42	70.6	42.30	43.21
81	188.0023	34.0295	24.91	24.61	26.82	26.75	173.6	42.51	42.61
82	187.3709	34.3606	24.74	24.61	26.02	26.02	75.3	42.43	42.95
83	187.4005	34.0804	24.73	24.62	26.06	25.86	81.1	42.40	43.02
84	187.7260	34.1673	24.97	24.62	25.70	25.43	30.6	42.29	43.21
85	187.8042	34.0462	24.84	24.63	25.75	25.36	42.6	42.26	43.24

ID	R.A. (deg.)	Dec. (deg.)	$NB400^{*}$ (ap)	$NB400^{\dagger}$ (AUTO)	g'^{*} (ap)	$g'^{\dagger}$ (AUTO)	EW_0 (Å)	$\log L_{\mathrm{Ly}\alpha}{}^{\ddagger}$ (erg s^{-1})	$\log L_{\mathrm{cont}}{}^{\S}$ (erg s^{-1})
86	187.7111	34.0849	24.74	24.63	26.56	26.45	155.6	42.48	42.76
87	187.8335	34.1742	24.94	24.63	26.27	25.08	80.8	42.10	43.35
88	187.9011	34.0262	24.95	24.64	26.19	25.67	70.7	42.35	43.11
89	187.8757	34.2920	25.00	24.64	26.34	25.32	82.5	42.23	43.25
90	187.7429	34.2789	24.88	24.65	25.66	25.64	34.5	42.34	43.12
91	187.4943	34.3735	24.72	24.66	25.31	25.21	22.8	42.15	43.30
92	187.3969	34.0973	24.89	24.67	26.37	26.09	99.5	42.41	42.92
93	187.7823	34.2181	24.96	24.67	26.51	26.37	108.6	42.45	42.80
94	187.9573	34.2042	24.95	24.67	26.17	25.88	69.5	42.37	43.01
95	187.7971	34.2007	24.99	24.68	25.54	25.38	21.1	42.22	43.23
96	187.3397	34.2770	24.95	24.68	26.36	26.21	90.7	42.42	42.87
97	187.4677	34.3015	24.89	24.70	26.53	26.04	121.9	42.38	42.95
98	187.5758	34.0253	24.98	24.72	25.92	25.71	44.4	42.30	43.09
99	187.4495	34.3318	25.14	24.73	25.75	25.53	24.7	42.24	43.17
100	187.4957	34.2310	25.03	24.73	26.04	24.84	50.4	41.50	43.46
101	187.6855	34.3993	25.10	24.75	25.98	25.11	40.3	41.97	43.34
102	187.6312	34.3507	24.88	24.77	25.84	25.80	47.2	42.30	43.05
103	187.4955	34.1347	25.10	24.77	25.73	25.16	25.4	41.99	43.32
104	187.7317	34.2704	25.19	24.79	26.01	24.81	36.7	40.79	43.47
105	187.4784	34.3438	25.16	24.79	26.65	26.41	100.7	42.39	42.78
106	187.3676	34.2433	25.18	24.79	26.38	26.09	67.9	42.34	42.93
107	187.4698	34.3888	25.27	24.80	26.26	25.62	48.4	42.22	43.13
108	187.4784	34.0146	24.91	24.82	26.00	25.95	57.2	42.30	42.99
109	187.9325	34.3694	24.95	24.85	25.93	25.81	48.3	42.24	43.05
110	187.9871	34.0463	25.24	24.85	25.93	25.68	28.9	42.20	43.11
111	187.7803	34.1326	25.08	24.85	26.08	25.81	49.5	42.24	43.05
112	187.3872	34.1697	25.12	24.86	26.18	25.93	54.6	42.27	43.00
113	187.7254	34.2196	24.93	24.86	26.53	26.43	115.6	42.36	42.78
114	187.6161	34.2505	25.15	24.86	27.13	26.49	190.0	42.36	42.75

ID	R.A. (deg.)	Dec. (deg.)	$NB400^{*}$ (ap)	$NB400^{\dagger}$ (AUTO)	g'^{*} (ap)	$g'^{\dagger}$ (AUTO)	EW_0 (Å)	$\log L_{\mathrm{Ly}\alpha}{}^{\ddagger}$ (erg s^{-1})	$\log L_{\mathrm{cont}}{}^{\S}$ (erg s^{-1})
115	187.7068	34.0224	25.06	24.87	25.89	25.68	37.5	42.19	43.11
116	187.8922	34.0112	25.12	24.87	26.20	26.15	56.4	42.31	42.90
117	187.9957	34.0661	25.22	24.87	26.10	25.75	40.4	42.22	43.08
118	187.5800	34.3663	25.06	24.87	27.09	26.91	203.5	42.40	42.56
119	187.8939	33.9937	24.97	24.88	26.68	26.58	135.4	42.36	42.71
120	187.4687	34.3877	24.97	24.89	25.79	25.68	36.7	42.17	43.11
121	187.6454	34.3646	24.98	24.90	25.58	25.49	23.5	42.08	43.19
122	187.5316	33.9888	25.27	24.90	26.00	25.83	30.8	42.22	43.04
123	187.9220	34.0334	25.22	24.92	26.24	26.19	51.5	42.29	42.89
124	187.7609	34.1605	25.24	24.93	26.92	26.53	129.6	42.33	42.74
125	187.4521	34.2492	25.10	24.93	25.73	25.57	25.4	42.09	43.16
126	187.6350	34.3254	25.05	24.94	26.77	26.74	135.9	42.35	42.64
127	187.9826	34.1164	25.06	24.94	26.06	25.90	49.7	42.21	43.01
128	187.6954	34.2091	25.03	24.94	26.33	26.06	77.1	42.25	42.95
129	187.6562	34.3894	25.27	25.01	26.93	26.18	126.3	42.23	42.90
130	187.8637	34.2186	25.12	25.03	25.77	25.69	26.1	42.06	43.11
131	187.5115	33.9905	25.28	25.05	26.63	26.36	82.9	42.24	42.82
132	187.3453	34.0996	25.18	25.06	26.63	26.55	94.8	42.26	42.74
133	187.3869	34.1895	25.30	25.07	26.92	26.71	120.2	42.28	42.66
134	187.7110	34.1507	25.14	25.09	26.96	27.00	154.1	42.30	42.53
135	187.4319	34.0250	25.39	25.09	26.31	25.94	43.2	42.12	43.00
136	187.4249	34.3683	25.30	25.09	26.25	25.52	45.2	41.89	43.18
137	187.4467	34.1725	25.31	25.09	26.35	25.95	53.4	42.12	43.00
138	187.9176	34.2427	25.14	25.10	26.40	26.24	73.4	42.19	42.87
139	187.6734	34.2123	25.48	25.11	26.36	25.32	40.7	41.61	43.26
140	187.7237	34.3154	25.15	25.12	26.55	26.35	89.2	42.20	42.83
141	188.0080	34.2556	25.31	25.12	26.39	26.10	56.3	42.14	42.94
142	187.4173	34.0712	25.33	25.12	26.23	26.20	42.0	42.17	42.89
143	187.9639	34.1395	25.29	25.14	26.49	26.41	67.3	42.20	42.80

ID	R.A. (deg.)	Dec. (deg.)	$NB400^{*}$ (ap)	$NB400^{\dagger}$ (AUTO)	g'^{*} (ap)	$g'^{\dagger}$ (AUTO)	EW_0 (Å)	$\log L_{\mathrm{Ly}\alpha}{}^{\ddagger}$ (erg s^{-1})	$\log L_{\mathrm{cont}}{}^{\S}$ (erg s^{-1})
144	187.9979	34.0457	25.40	25.16	26.42	25.83	51.2	42.01	43.05
145	187.4665	34.4136	25.33	25.17	26.47	26.13	61.9	42.12	42.92
146	187.9315	34.1540	25.37	25.17	$>27.35^{\P}$	$-^{\parallel}$	$>1002.7^{**}$	$42.35<^{\dagger\dagger}$	$-^{\ddagger\ddagger}$
147	187.3431	34.3778	25.34	25.24	27.05	26.78	134.2	42.20	42.64
148	187.7276	34.1942	25.35	25.26	27.14	27.25	150.8	42.23	42.43
149	187.8774	34.2977	25.25	25.27	26.67	26.60	92.0	42.16	42.72

Notes.

* $NB400$ and g' magnitudes measured by the fixed-aperture ($2''$) photometry.

† $NB400$ and g' magnitudes measured by the Kron photometry.

‡ The Lyα luminosity based on the Kron photometry.

§ The continuum luminosity based on the Kron photometry.

¶ The 3σ limiting magnitude.

$^{\parallel}$ The measured flux in the g'-band of this object is negative.

** The lower limit of EW_0 calculated from the 3σ limiting fixed-aperture magnitude in the g'-band.

†† The upper limit of $L_{\mathrm{Ly}\alpha}$ calculated by assuming $f_\nu = 0$ in the g'-band.

‡‡ The continuum luminosity of this object can not be calculated because the measured flux in the g'-band of this object is negative value.

2.4.2 *A candidate of a DLA counterpart*

So far, DLA counterparts have been mostly found close to quasar sight-lines with the impact parameter of $b < 25$ kpc (e.g., Fumagalli et al., 2010; Krogager et al., 2012, 2013; Kashikawa et al., 2014). On the other hand, Rao et al. (2011) investigate the distribution of impact parameters at low-z ($0.1 < z < 1$) and show that DLA counterparts could have impact parameters up to $\sim$100 kpc (see also Battisti et al., 2012; Straka et al., 2016). Motivated by this low-z study, we search for counterparts of strong absorbers from our LAE sample within $12''.2$ (corresponding to 100 kpc at $z = 2.3$) from the sightline to quasars showing a strong absorption feature. As a result, we find a LAE near 1 DLA (along the line-of-sight to a quasar, the SDSS J122942.74+342202.1; No.2 in Table 2.1, Figures 2.1, and 2.25) as shown in Figure 2.26, among 4 absorbers in the J1230+34 field. Its impact parameter to the quasar sightline is $\sim$87 kpc (physical scale, that corresponds to $10''.6$). Note that, there are no objects with $g' - NB400 > 0$ closer than $10''.6$ from the quasar sightline. The apparent magnitudes of this candidate are $NB400 = 25.30$ and $g' = 26.25$. We derive the star-formation rate (SFR) of this candidate based on the Lyα flux ($F_{\mathrm{Ly}\alpha}$ = 1.9×10^{-17} erg s^{-1} cm^{-2}, that corresponds to the Lyα luminosity of $L_{\mathrm{Ly}\alpha} = 7.7 \times 10^{41}$ erg s^{-1}) using the Kennicutt (1998) relation. The derived SFR of 0.7 $M_{\odot}$ yr^{-1} is a bit lower than other DLA counterparts at $z > 2$ reported by some previous studies (e.g., Péroux et al., 2012; Bouché et al., 2013; Fynbo et al., 2013; Krogager et al., 2013; Srianand et al., 2016).

To confirm whether or not this LAE is really a DLA counterpart, spectroscopic follow-up observations are required. On the other hand, optical candidates of the counterparts are not found for the remaining 3 absorbers, at least as LAEs. Further NB imaging data with deeper depth are required to explore the candidates for the counterparts of the remaining 3 absorbers. Alternatively, counterparts for those absorbers may be other populations of galaxies such as Lyman break galaxies that cannot be selected through NB observations. In this case, further u-band observations will be useful to identify galaxies through the so-called BMBX selection (Steidel et al., 2004) without relying on the Lyα emission.

2.4.3 *The Lyα luminosity function*

Here, we derive the Lyα luminosity function (LF) of LAEs detected in the J1230+34 field and compare it with some previous results at a similar redshift.

The Lyα flux and luminosity

We calculate the Lyα flux and luminosity of the detected LAEs following the method described in Mawatari et al. (2012). The flux per unit frequency (erg s^{-1} cm^{-2} Hz^{-1}) of the $NB400$ ($f_{\nu NB400}$) and the g'-band ($f_{\nu g'}$) is described as

$$f_{\nu NB400} = f_{\nu \mathrm{C}} + f_{\nu \mathrm{Ly}\alpha}, \tag{2.2}$$

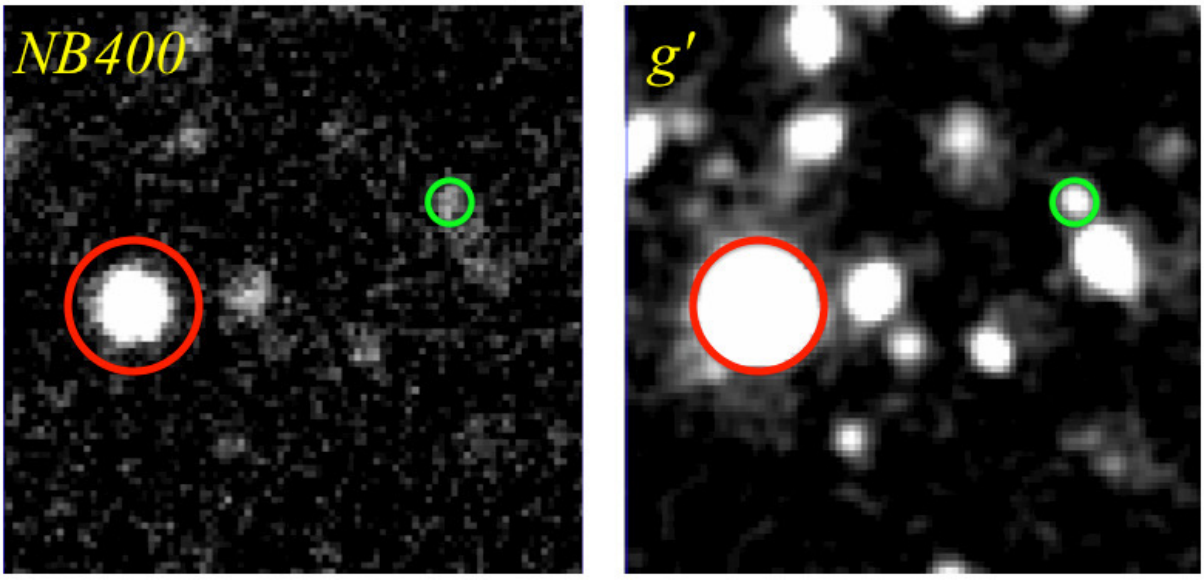

Fig. 2.26: Images of the candidate of the DLA counterpart in $NB400$ (left) and g' (right). The green and the red circles show the candidate of the DLA counterpart and the corresponding BGQSO. The separation of them is $10''.6$, that corresponds to $\sim$87 kpc at $z = 2.3$.

$$f_{\nu g'} = f_{\nu \mathrm{C}} + f_{\nu \mathrm{Ly}\alpha} \times \frac{\int_{\lambda_{min,NB400}}^{\lambda_{max,NB400}} T_{\lambda,g'} d\lambda}{\int_{\lambda_{min,g'}}^{\lambda_{max,g'}} T_{\lambda,g'} d\lambda}, \tag{2.3}$$

where $f_{\nu \mathrm{Ly}\alpha}$ and $f_{\nu \mathrm{C}}$ are the flux per unit frequency of the Lyα and the continuum emission at $\lambda_{\mathrm{obs}} = 4003$ Å, respectively. $T_{\lambda,g'}$ is the response function of g'-band filter. Assuming the flat continuum over the range of the g'-band coverage, we can calculate the Lyα flux and the g' flux. Based on the Lyα flux per unit frequency, we can calculate the integrated flux (erg s^{-1} cm^{-2}) as

$$F_{\mathrm{Ly}\alpha} = f_{\nu \mathrm{Ly}\alpha} \times \Delta\nu_{NB400}, \tag{2.4}$$

where $\Delta\nu_{NB400}$ is the band width in FWHM (Hz) of the *NB*400 filter (1.72×10^{13} Hz). The Lyα luminosity is calculated as

$$L_{\mathrm{Ly}\alpha} = 4\pi d_{\mathrm{L}}^2 F_{\mathrm{Ly}\alpha}, \tag{2.5}$$

where d_{L} is the luminosity distance. For calculating d_{L} of the LAEs in our study, we assume that all of LAEs are at $z = 2.3$ that corresponds to the center of the *NB*400 coverage.

Detection completeness

We estimate the detection completeness for objects in the *NB*400 image using Monte Carlo simulations. The procedure of estimation is as follows: (1) inserting artificial objects randomly in the *NB*400 image except for masked regions, (2) detecting the artificially inserted objects with the same condition as the real detection with SExtractor (see Section 2.3.2), and (3) measuring the fraction of the number of successfully detected artificial objects as a function of the apparent *NB*400 magnitude from *NB*400 = 19.8 to 26.0 in 0.2 mag intervals. Here we assume that distributed objects are point sources with FWHM of $0''.9$, that corresponds to the PSF size of the smoothed *NB*400 image (see Section 2.3.2). Figure 2.27 shows the detection completeness as a function of *NB*400 magnitude. Around the 5σ limit of the *NB*400 magnitude, the estimated detection completeness is $\sim$70%. The completeness decreases quickly beyond the 5σ limiting magnitude.

The Lyα luminosity function

We derive the Lyα LF of LAEs detected in our *NB*400 observation, based on the Lyα luminosity and detection completeness. Note that we do not correct for the selection completeness (i.e., how LAEs are completely selected from the detected objects through the adopted color criteria), since Ouchi et al. (2008) showed that the incompleteness through the color selection is negligible. We divide the completeness-corrected number of LAEs by the surveyed volume following the calculation method of previous NB studies of Lyα LF of LAEs (e.g., Ajiki et al., 2003; Ouchi et al., 2003, 2008; Hu et al., 2004; Malhotra & Rhoads, 2004; Konno et al., 2014, 2016).

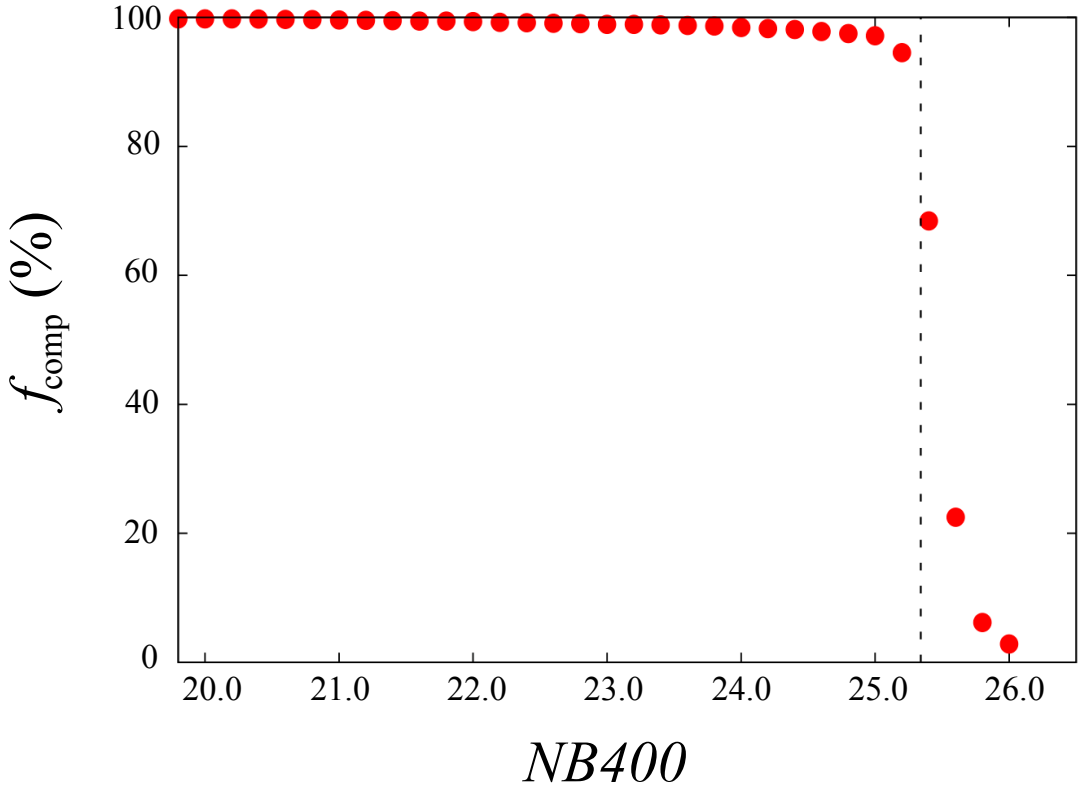

Fig. 2.27: The detection completeness, $f_{\rm comp}$, as a function of the $NB400$ magnitude. The black dotted line shows the 5σ limiting magnitude of $NB400$.

Figure 2.28 shows the derived Lyα LF of our LAE sample. The Lyα LF of LAEs is usually fitted by the Schechter function (Schechter, 1976); i.e., the number density of LAEs tends to decrease exponentially with the Lyα luminosity at the bright side. However, in the high luminosity regime ($L_{\mathrm{Ly}\alpha} > 10^{43.5}$ erg s^{-1}) of our result, the number density of LAEs dose not show the exponential decrease but showing an excess of the number density with respect to the Schechter function. This trend is seen also in some previous LAE studies (e.g., Ouchi et al., 2008; Konno et al., 2016), and it is thought to be due to the contribution of active galactic nuclei (AGNs). As for our case, we confirm that at least one object in the brightest luminosity bin is a quasar included in the BOSS quasar catalog (BGQSO-A, SDSS J122926.53+342441.9; Pâris et al., 2012). In the low-luminosity regime ($L_{\mathrm{Ly}\alpha} < 10^{42.0}$ erg s^{-1}), the correction for the completeness is not enough, due to very low selection completeness owing to relatively large photometric errors of faint objects.

We then compare the derived Lyα LF of LAEs in the J1230+34 field with the Lyα LFs in blank fields. Specifically, we compare our result with the Lyα LF of LAEs at $z = 2.2$ reported by Konno et al. (2016) and Hayes et al. (2010) in Figure 2.28. Due to the contribution of AGNs and the incompleteness we described above, we focus on the luminosity range of $10^{42.0} < L_{\mathrm{Ly}\alpha} < 10^{43.5}$ erg s^{-1} for the comparison. Consequently, as shown in Figure 2.28, no significant difference in the Lyα LF of LAEs in the J1230+34 field relative to blank fields is found.

2.4.4 *The frequency distribution of Lyα EW_0*

In order to characterize properties of LAEs in the J1230+34 field, we study their EW_0 distribution (Figure 2.29). Here, we compare our result with that of LAEs at a similar redshift ($z = 2.4$) in an over-density region of LAEs reported by Mawatari et al. (2012) and in a blank field at $z = 2.25$ reported by Nilsson et al. (2009). For a quantitative comparison of the Lyα EW_0, we adopt the following analytic formula,

$$N = C \times e^{-EW_0/w_0} \tag{2.6}$$

(see Gronwall et al., 2007; Mawatari et al., 2012). We fit the Lyα EW_0 distribution in the EW_0 range of $25 \leq EW_0 \leq 350$ Å. The e-folding lengths, w_0, of this work, Mawatari et al. (2012), and Nilsson et al. (2009) are $w_0 = 53.5 \pm 4.7$ Å, $w_0 = 43.7 \pm 0.4$ Å, and $w_0 = 48.5 \pm 1.7$ Å, respectively. It is thus inferred that w_0 in our study is consistent with those in Mawatari et al. (2012) and Nilsson et al. (2009) at 2σ and 1σ, respectively.

2.4.5 *LAEs with a large EW_0*

In this work, we are focusing on LAEs which are thought to be young population of galaxies. This is because the absorber-concentrated regions are possibly gas-rich regions and thus young galaxies may preferentially exist there. Since the younger LAEs tend to show the larger Lyα

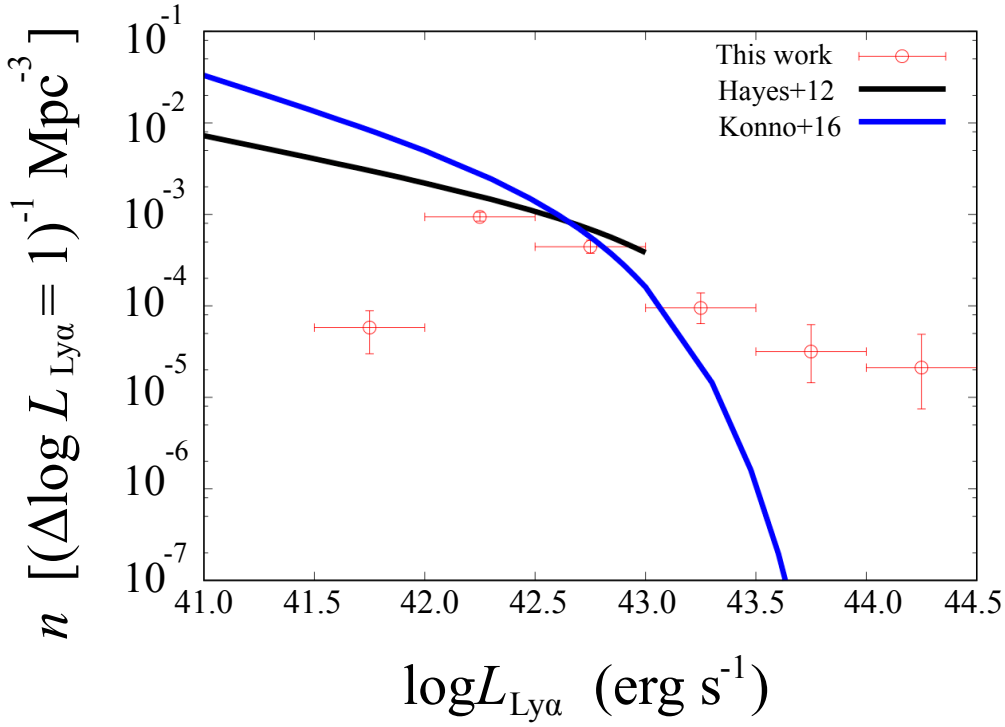

Fig. 2.28: The Lyα luminosity function. Red open circles show our result with a luminosity bin of $\Delta\log L_{\mathrm{Ly}\alpha} = 0.5$. The blue and black curves show the Schechter function fits for LAEs at $z = 2.2$ by Konno et al. (2016) and Hayes et al. (2010), respectively.

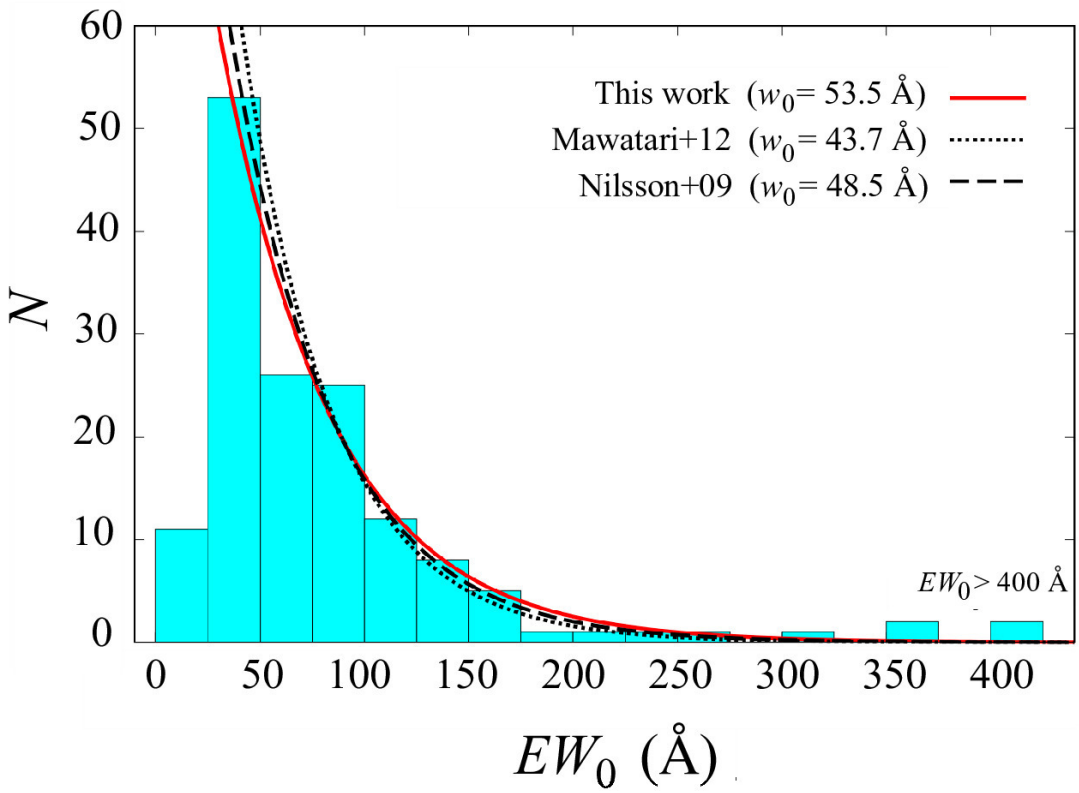

Fig. 2.29: The frequency distribution of the Lyα rest-frame equivalent width. The bin width for EW_0 is 25 Å. The red solid, black dotted, and black dashed lines show the exponential fit for this work, Mawatari et al. (2012) at $z = 2.4$, and Nilsson et al. (2009) at $z = 2.25$, respectively.

EW_0 (e.g., Malhotra & Rhoads, 2002; Nagao et al., 2007), we here focus on LAEs with a large EW_0. In Table 2.9, we show the basic data of LAEs with $EW_0 > 200$ Å. There are 8 LAEs with $EW_0 > 200$ Å in the J1230+34 field. All of their positions are somewhat far from absorbers. The nearest LAE with large EW_0 is 5.5 Mpc (corresponding to $\sim 203''$) away from an absorber. There are no large EW_0 LAEs within 5 Mpc (corresponding to $\sim 185''$) from each absorber.

Table 2.9: General information of LAEs with $EW_0 > 200$ Å

R.A. (deg.)	Dec. (deg.)	$NB400^*$ (ap)	$NB400^\dagger$ (AUTO)	g'^* (ap)	$g'^\dagger$ (AUTO)	EW_0 (Å)	$\log L_{\mathrm{Ly}\alpha}{}^\ddagger$ (erg s^{-1})	$d_{\mathrm{abs-LAE}}{}^\S$ (arcmin)	$d_{\mathrm{abs-LAE}}{}^\S$ (Mpc)	Nearest¶ absorber
187.9011	34.4046	23.08	21.86	26.39	24.11	1381.4	43.61	6.91	11.2	4
187.9315	34.1540	25.37	25.17	$>27.35^\parallel$	-**	$>1002.7^{\dagger\dagger}$	$42.34<^{\ddagger\ddagger}$	8.15	13.2	4
187.5902	34.2382	23.54	23.32	26.01	25.84	365.3	43.04	6.14	10.0	3
187.5307	33.9967	24.88	23.83	27.35	25.37	357.7	42.77	5.71	9.3	3
187.4330	34.0814	23.20	23.10	25.55	25.37	308.1	43.12	3.37	5.5	1
187.9175	34.0508	24.58	24.52	26.77	26.34	250.8	42.52	14.29	23.2	3
187.9455	34.3996	24.65	24.33	26.80	25.72	238.0	42.54	6.49	10.5	4
187.5800	34.3663	25.06	24.87	27.09	26.91	203.5	42.40	7.45	12.1	2

Notes.

* $NB400$ and g' magnitudes measured by the fixed-aperture ($2''$) photometry.

† $NB400$ and g' magnitudes measured by the Kron photometry.

‡ The Lyα luminosity based on the Kron photometry.

§ The distance from the LAE to the nearest absorber.

¶ The ID of the nearest absorber from the LAE. The number corresponds to the No. in Table 2.1, Figures 2.1 and 2.25.

‖ The 3σ limiting magnitude.

** The measured flux in the g'-band of this object is negative.

†† The lower limit of EW_0 calculated from the 3σ limiting fixed-aperture magnitude in the g'-band.

‡‡ The upper limit of $L_{\mathrm{Ly}\alpha}$ calculated by assuming $f_\nu = 0$ in the g'-band.

2.5 Discussion

2.5.1 The properties of LAEs located close to absorbers

As described in Sections 2.4.3 and 2.4.4, the obtained Lyα LF is consistent with those in blank fields at similar redshift. Also, we found no differences in the frequency distribution of the Lyα EW_0 in the target field and those in some other fields including an overdensity region and blank fields. Here we focus on the results of Mawatari et al. (2012). They studied the spatial distribution of LAEs around a radio galaxy at $z \sim 2.4$ (53W002) using Subaru/Suprime-Cam. They found that there is a significantly high density region around the radio galaxy spreading over $\sim 5' \times 4'$ (8.3 Mpc $\times$ 6.6 Mpc in the comoving scale at $z = 2.4$). However, the number density of LAEs in the entire the 53W002 field ($\sim$50 Mpc $\times$ 40 Mpc) is comparable to the average density of LAEs in blank fields at $z \sim 2$. This implies that we may miss the density excess in such Mpc-scale region by focusing only on the average density in the entire field. Therefore, it is worthwhile to study local characteristics of LAEs in the J1230+34 field. Motivated by this, we investigate the surface number density of LAEs around each absorber in the target field. Figure 2.30 shows the surface number density of LAEs as a function of the distance from each absorber in the J1230+34 field. The surface number density of LAEs is calculated by dividing the number of LAEs by the area of a circular region centered on the positions of each absorber. As seen in Figure 2.30, LAEs around the absorber No.2 show the density excess over $\sim$400 arcsec ($\sim$11 Mpc) relative to the average density of LAEs in the entire J1230+34 field (black dotted line in Figure 2.30). Indeed, in Figure 2.25, we can see the possible number excess of LAEs around the absorber No. 2. Interestingly, the absorber No. 2 is the strongest DLA with $\log N_{\rm HI} = 21.08$ cm^{-2} in the J1230+34 field. On the other hand, we found no density excess of LAEs around remaining 3 absorbers, whose H I column densities are smaller than that of absorber No. 2. Here we should mention the BGQSOs around the absorber No.2. The BGQSO A (in Figure 2.25) is a quasar at $z = 2.275$ and thus it is a member of objects in the absorber-concentrated region. Indeed, this BGQSO A is detected as a LAE in our observation (see Section 2.4.3). The projected comoving distance from the BGQSO B to the absorber No.2 is $\sim$6.9 Mpc (255$''$) and the redshift difference (Δz=0.007) between the BGQSO A and the absorber No2 corresponds to $\sim$9.0 comoving Mpc. Since we set the redshift range of the BGQSOs not to miss PDLAs, this quasar satisfy the criteria even its redshift is very similar with those of target absorbers. As for the BGQSO B, although it satisfies the BGQSO criteria, it is difficult to recognize intervening absorbers at $z \sim 2.3$ due to low S/N since its Lyman limit locates very close to the wavelength coverage of $NB400$ as shown in Figure 2.6.

We also examine the frequency distribution of the Lyα EW_0 within 10 Mpc from the absorber No. 2. There are 29 LAEs within 10 Mpc from the absorber No. 2. Figure 2.31 shows the derived frequency distribution of the Lyα EW_0 around the absorber No. 2. By adopting the same fitting formula as in Section 2.4.4 (Equation 2.6), we obtain the exponential length of $w_0 = 34.4 \pm 10.1$. Although the value of w_0 is smaller than that in the entire target field ($w_0 = 53.5 \pm 4.7$), w_0 around absorber No.2 is consistent with that in the entire field within 2σ due to the large error. Here, the fitted EW_0 range is $25 \leq EW_0 \leq 200$ Å. Out of 29 LAEs within

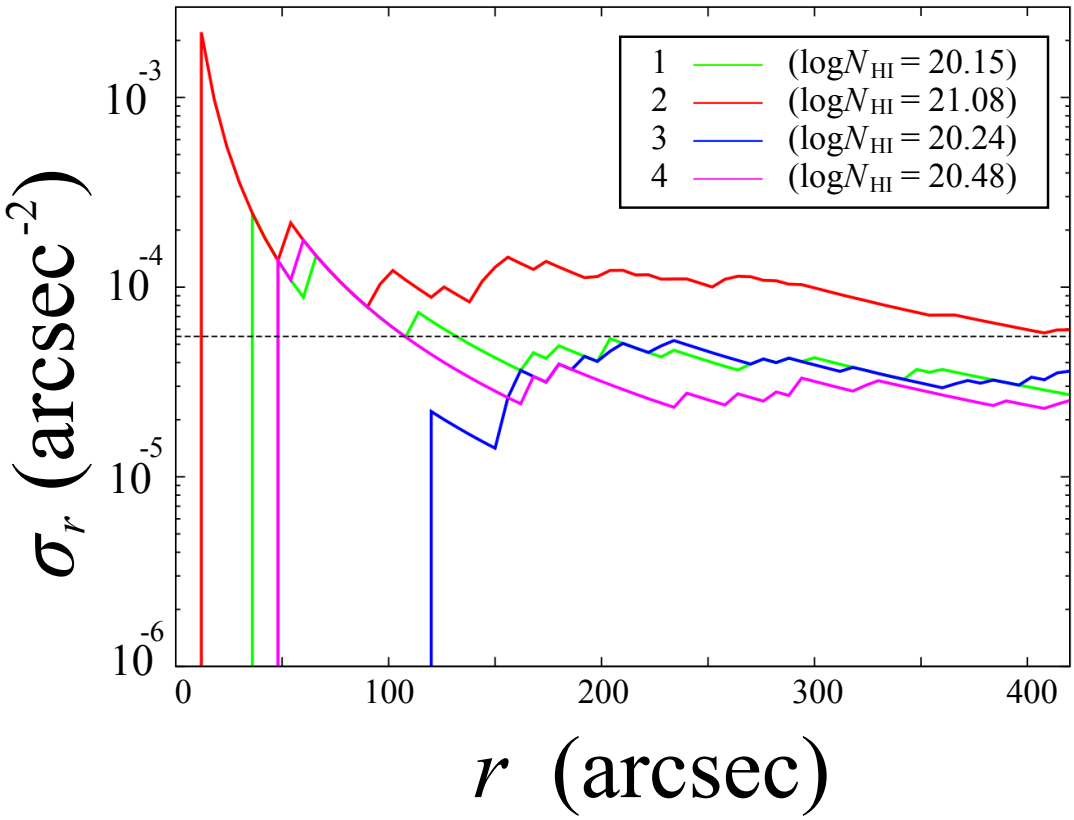

Fig. 2.30: The surface number density of LAEs around each absorber in the J1230+34 field, as a function of the radius (r) adopted to calculate the surface density. The vertical axis indicates the surface number density of LAEs within a circular regions at r. The horizontal axis indicates the radius of circular regions from the position of each absorber. The IDs for the absorbers correspond to those in Table 2.1 and Figure 2.1. The dotted horizontal black line indicates the average of the LAE density calculated for the entire J1230+34 field.

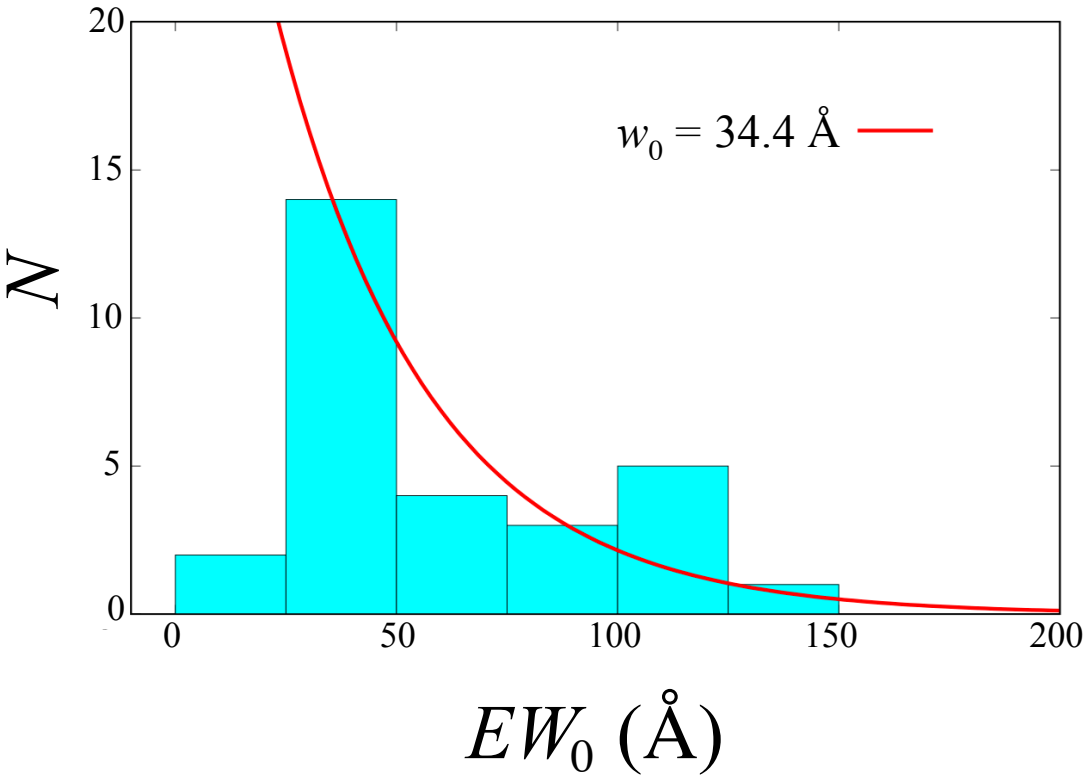

Fig. 2.31: The frequency distribution of the Lyα EW_0 of LAEs within 10 Mpc from the absorber No. 2 (red line) and in the entire target field (black line).

10 Mpc from absorber No. 2, ∼80% of them have $EW_0 < 100$ Å. There are no LAEs with $EW_0 > 150$ Å close to the DLA (see also Table 2.9). There are no difference in the properties of LAEs in the large scale, while we find a possible overdenstiy of LAEs in the small scale of ∼10 Mpc. Based on this finding, we discuss possible scenarios for absorber-concentrated regions in Section 2.5.3.

2.5.2 *A quasar in the possible overdensity region of LAEs around the absorber No.2*

As we report in Section 2.5.1, we find a quasar associate with the possible overdensity of LAEs. It has been thought that the quasar is a good tracer for high-z overdensity regions (e.g., Wylezalek et al., 2013; Adams et al., 2015). However, some recent studies (e.g., Bañados et al., 2013; Mazzucchelli et al., 2017; Uchiyama et al., 2017) show that many quasars do not reside in overdensity environment. Especially, Uchiyama et al. (2017) studied environments of >150 quasars using the wide-field (>100 deg^2) data obtained with Hyper Suprime-Cam (HSC; Miyazaki et al., 2012) on the Subaru telescope. They reported that most quasars in their sample do not reside in overdensity environments but in general environments. These recent works imply that the possible LAE overdensity we found may rather associate with absorber environment and may not be related to the quasar environment.

2.5.3 *Possible scenarios for absorber-concentrated regions*

Here, we discuss why the Lyα LF and the Lyα EW_0 distributions in the J1230+34 field show no difference compared to those in an overdensity region and blank fields. One possible scenario is that the J1230+34 field harbors many young galaxies intrinsically, that are made from plenty of gas suggested by the concentration of strong absorbers. However, since there is a large amount of H I gas around absorbers, the effect of the resonant scattering is serious. Since the Lyα emission is the resonant line and has a large scattering cross section, the optical depth becomes very high even with small amount of gas (e.g., Hayes, 2015). Therefore, Lyα photons experience a large number of scattering, resulting in a higher probability that Lyα photons are absorbed by dust. Consequently, we may underestimate the Lyα EW_0 and miss a large fraction of LAEs around absorbers. On the other hand, as we show in Section 2.5.1, we find a possible overdensity of LAEs around a DLA with the highest $N_{\rm HI}$ in the target field while no overdensity is found around absorbers with smaller $N_{\rm HI}$. At a glance, this situation looks inconsistent with the scenario described above. However, we may explain both of the existence of LAE overdensity around the DLA with the highest $N_{\rm HI}$ and the lack of the number excess of LAEs around absorbers with lower $N_{\rm HI}$ as follows: (1) around high $N_{\rm HI}$ absorber, there are enough number of LAEs to detect the overdensity even though the effect of the resonant scattering is serious, and (2) around lower $N_{\rm HI}$, although there are intrinsic number excess of LAEs, it is not enough to defeat the effect of resonant scattering. To examine this scenario,

further Hα observations are required since it is basically free from the resonant scattering (e.g., Garn & Best, 2010). If this scenario is the case, we will find the number excess of Hα emitters (HAEs) around absorbers.

An alternative idea is that there are not so many galaxies in the target field even though there are many neutral gas. H I gas is not converted stars directly but goes through the molecular clouds. Thus, a large fraction of H I gas may not be converted to stars. To discuss the star-formation process in the absorber-concentrated region, observations of molecular gas are required as well as H I gas and galaxies.

Furthermore, if we follow the idea that the origin of absorbers is the disk of galaxies, gas may not extend so widely. In this case, an absorber corresponds just to a galaxy and thus the absorber-concentrated region may not be a gas-rich region. Although the fact that BGQSOs (A and B) near absorber No.2 do not have absorbers at $z \sim 2.3$ may support this idea, BGQSO-A is at $z = 2.275$ and thought to be a member of $z \sim 2.3$ objects and we cannot recognize absorbers $z \sim 2.3$ on the spectra of BGQSO-B. Therefore, we cannot discuss this possibility only with our current data. To examine this idea, the surface number density of the BGQSOs is still low. When the data of future deep spectroscopic surveys such as the extend BOSS (eBOSS; Dawson et al., 2016) and the Subaru Prime Focus Spectrograph (PFS) survey (Takada et al., 2014) will be available, the surface number density of BGQSOs will increase significantly and accordingly we can tackle this problem. Alternatively, DLAs whose background sources are galaxies (gal-DLAs) are newly found by Cooke & O'Meara (2015) and Mawatari et al. (2016). Since the surface density of galaxies is much higher than that of quasars, we can investigate the spatial distribution of neutral gas by focusing on gal-DLAs. Future 30-m class telescopes enable us to solve this problem.

2.6 Concluding remarks

Based on the BOSS strong Lyα absorber catalog, we have searched for absorber-concentrated regions and obtained the following results.

1. We find 6 concentrated region of strong Lyα absorbers $N_{\rm HI} > 10^{20.0}{\rm cm}^{-2}$ from the absorber catalog based on the BOSS, i.e., three or more absorbers distribute within the cubic region of (50 Mpc)^3 with the comoving scale in the redshift range of $2.255 < z < 2.330$.

2. Among 6 absorber concentrated regions, we found a rare and interesting region, J1230+34 field, where 4 absorbers (2 DLAs and 2 sub-DLAs) distribute within the cuboidal space with 50 Mpc $\times$ 50 Mpc $\times$ 53.5 Mpc.

3. Through a wide and deep Suprime-Cam search for LAEs with the *NB*400 filter toward the J1230+34 field, 149 LAEs are detected.

4. We find no difference in the Lyα LF in the target field relative to those in blank fields at similar redshift.

5. The frequency distribution of the Lyα EW_0 of the LAEs in the entire J1230+34 field is similar to those in a overdensity region and blank field at $z \sim 2$.

6. When we focus on the region close to absorber, we find a possible number excess of LAEs around a DLA with the highest H I column density ($\log N_{\rm HI} = 21.08$ cm^{-2}) in the target field.

The target field, the J1230+34 field is an important region to understand the early phase of galaxy evolution. Further observations in the different wavelength range, such as Hα emission, are expected to investigate the properties of galaxies around absorbers. Unfortunately, it is still challenging to investigate the extent of the H I gas due to too low number density of BGQSO even by using BOSS data. When the surface number density of background sources increase (not only quasars but also galaxies), the J1230+34 field is one of the most interesting field to investigate the relation of gas and galaxies.

CHAPTER 3

GENERAL CONCLUSION

In this dissertation, we study the early phase of the galaxy evolution by focusing on DLAs. We specifically focus on concentrated regions of strong Lyα absorbers in order to investigate the physical relationship between absorbers and young galaxies. Here we define the absorber-concentrated regions as the regions three or more absorbers distribute within the cubic region of (50 Mpc)^3 in the comoving scale based on the typical size of protoclusters at high-z. From the BOSS DLA sample, we found 6 absorber-concentrated regions at $2.255 < z < 2.330$. Among them we focus on the J1230+34 field, where 2 DLAs and 2 sub-DLAs distribute and conducted NB observations to search for LAEs using custom-made NB filter, *NB*400, with Subaru/Suprim-Cam. Our observations yield a sample of 149 LAEs in the J1230+34 field. Main results of this study about the relationship between absorbers and LAEs are as follows.

1. We search for candidates of DLA counterparts from our LAE sample within 100 kpc from the quasar sightline. We find a LAE at $\sim$87 kpc from the sightline to a quasar, the SDSS J122942.74+342202.1. The SFR of this LAE is 0.7 $M_\odot$ yr^{-1} and it is a bit lower than other DLA counterparts reported by previous studies. On the other hand, we find no optical counterparts for remaining 3 absorbers. Galaxy counterparts of these absorbers may not emit or emit only weak Lyα emission.

2. We derive the Lyα LF using all 149 LAE sample in the J1230+34 field and comparing the obtained LF and those in blank fields at similar redshifts. We found no significant difference between the Lyα LF in the J1230+34 fields and those in blank fields.

3. We investigate the frequency distribution of Lyα EW_0 of all LAE sample in the J1230+34 field. We fit the Lyα EW_0 by an analytic formula, $N = C\times^{-EW_0/\omega_0}$ and obtain the scale length of $w_0 = 53.5 \pm 4.7$ Å. This result is consistent with those in an overdensity region and a blank field at similar redshift.

4. In the small scale of $\sim$ 10 Mpc in the comoving scale, we found a possible overdensity of LAEs around a DLA No.2 with the highest column density ($\log N_{\rm HI} = 21.08$ cm^{-2}) in the J1230+34 field.

5. Using the 29 LAE sample within 10 Mpc in the comoving scale from the absorber No.2, we investigate the frequency distribution of Lyα EW_0 in the 10 comoving Mpc scale. We then obtain $w_0 = 34.4 \pm 10.1$ Å. Due to the large error, this value is consistent with that in the entire field within 2σ.

The study for the absorber-concentrated regions show a possible close relation between DLAs and LAEs. Although we have found no number excess of LAEs around three of four absorbers, it may be due to the resonant scattering and dust attenuations in the neutral gas-rich regions around absorbers. Recently the evidence for suppression of Lyα emission in the cluster environment has been found (e.g., Toshikawa et al., 2016; Lemaux et al., 2017; Shimakawa et al., 2017a). Absorber-concentrated regions may correspond to such cluster regions with particularly large amount of the gas. Although LAEs are important population as a population of galaxies in the early phase of the galaxy evolution, it may not be a good way to investigate galaxies around DLAs by only focusing on LAEs for studying the relationship between DLAs and galaxies or searching for DLA counterparts. Further investigations without relying on the Lyα emission line are expected.

Now there are number of ongoing and planned large surveys. These wide and deep surveys enable us to work on the studies revealing the nature of DLAs where we could not explore by past surveys. For example, large spectroscopic surveys such as ongoing eBOSS and coming survey with Subaru/PFS will increase the number density of background sources. Then we can effectively search for the absorber-concentrated regions. By focusing on absorber-concentrated regions, we can approach the process that the gas is converted to stars in the very early phase of the galaxy evolution. Absorber-concentrated regions should be investigated systematically for understanding to understand the complete picture of the galaxy evolution. Our study paves the way for future investigations for the galaxy evolution by focusing on DLAs.

Appendix A

IMAGES OF DETECTED LAEs

Here, we show *NB*400 and g'-band images of all 149 LAEs we found in the J1230+34 field. These images are useful for checking the morphology of detected LAEs. IDs for images correspond to those in Table 2.8. The FoV of each image is $\sim 18'' \times 18''$. Note that since these images are taken with the position angle of 180° and we have not rotated images, south is up and east is right in each image. We show the green circle with a diameter of $2''$ in each image, which corresponds to the aperture diameter for the photometry.

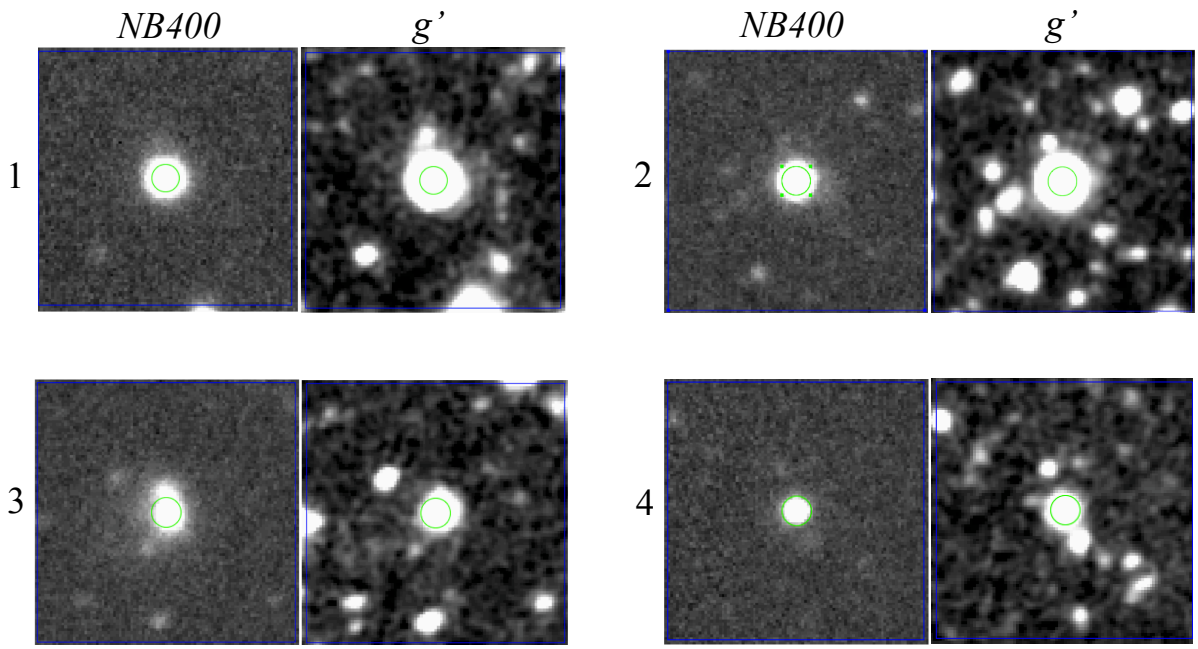

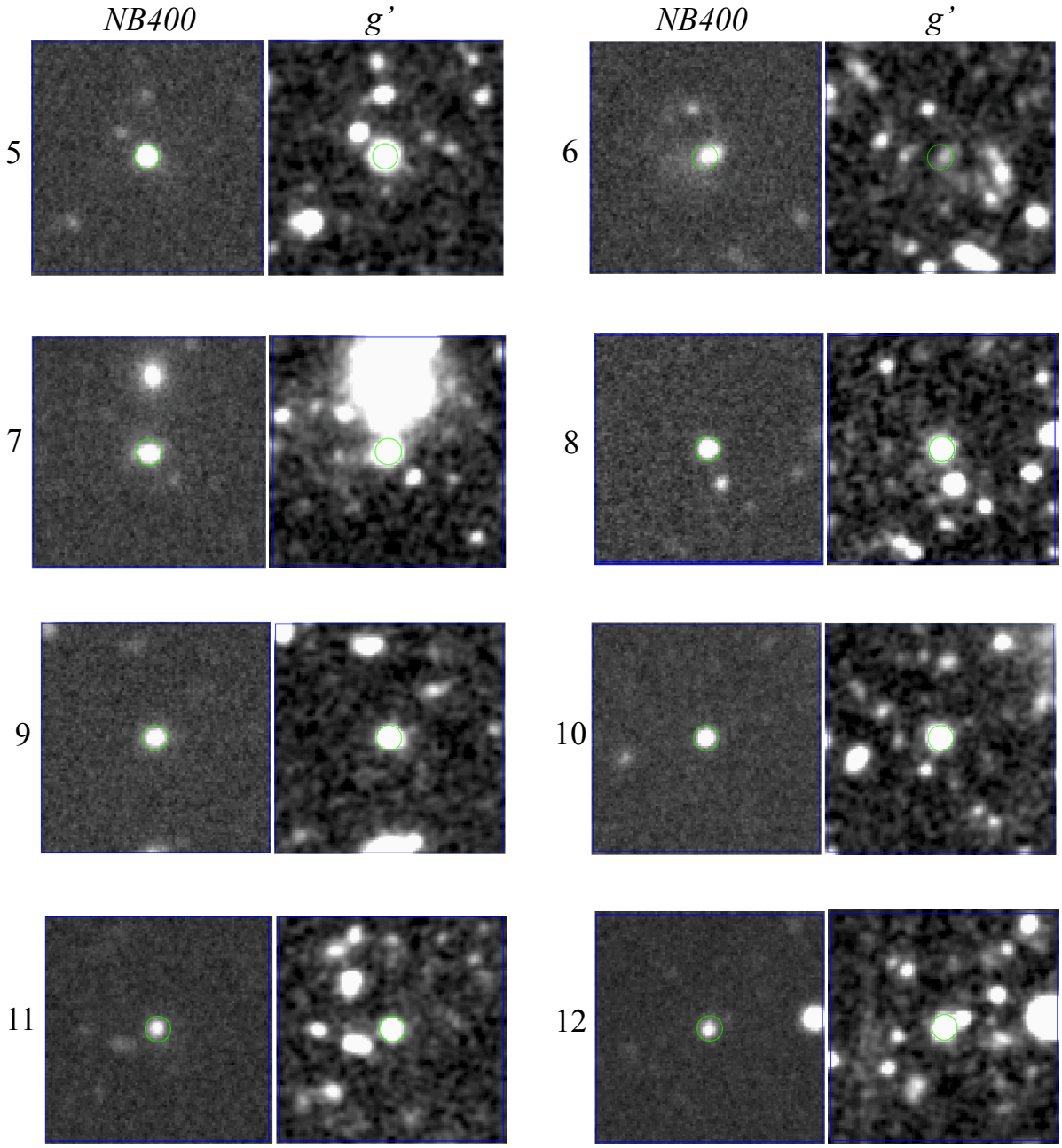
NB400
g'
NB400
g'
5
6
7
8
9
10
11
12

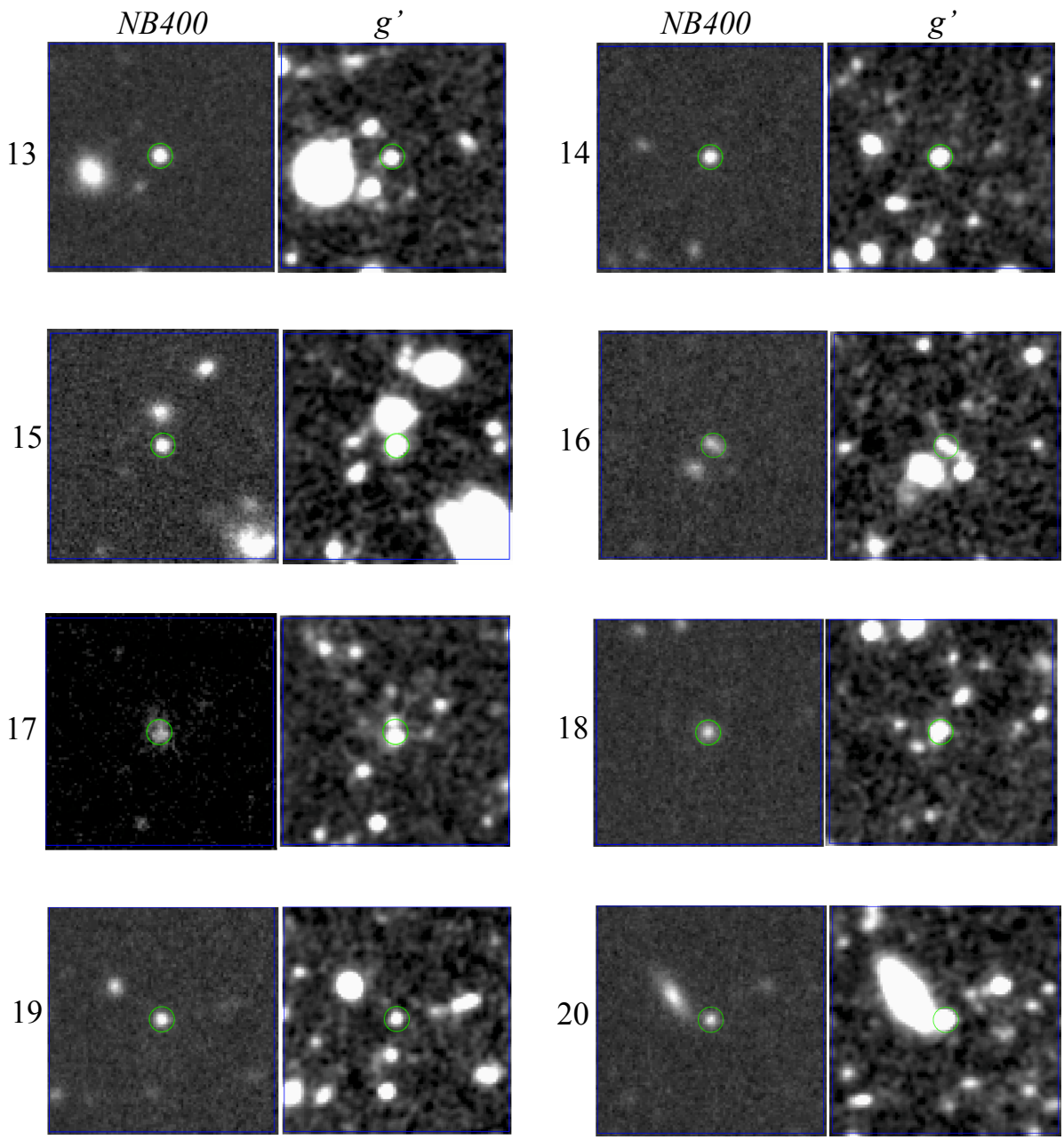
NB400
g'
NB400
g'
13
14
15
16
17
18
19
20

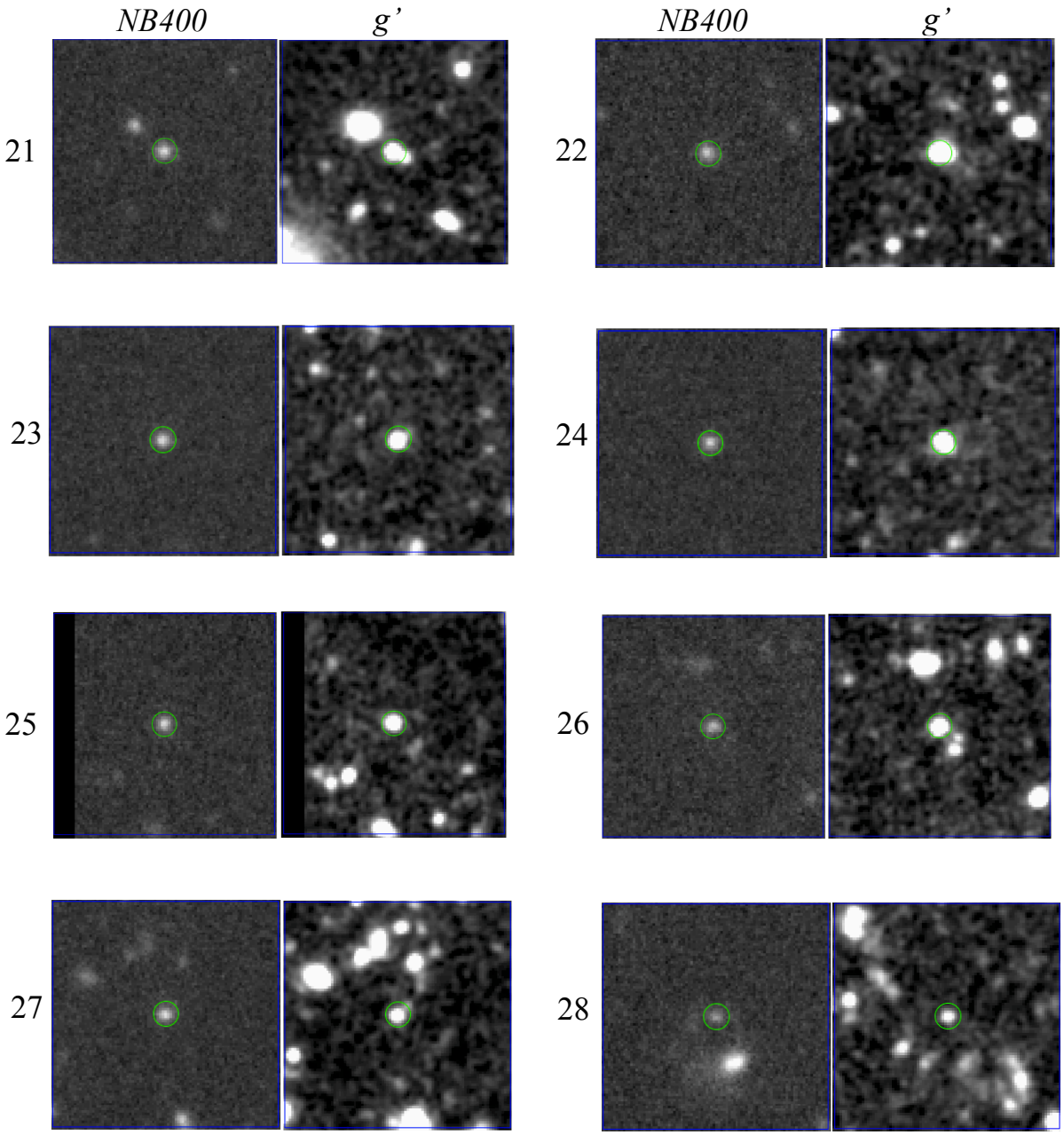
NB400
g'
NB400
g'
21
22
23
24
25
26
27
28

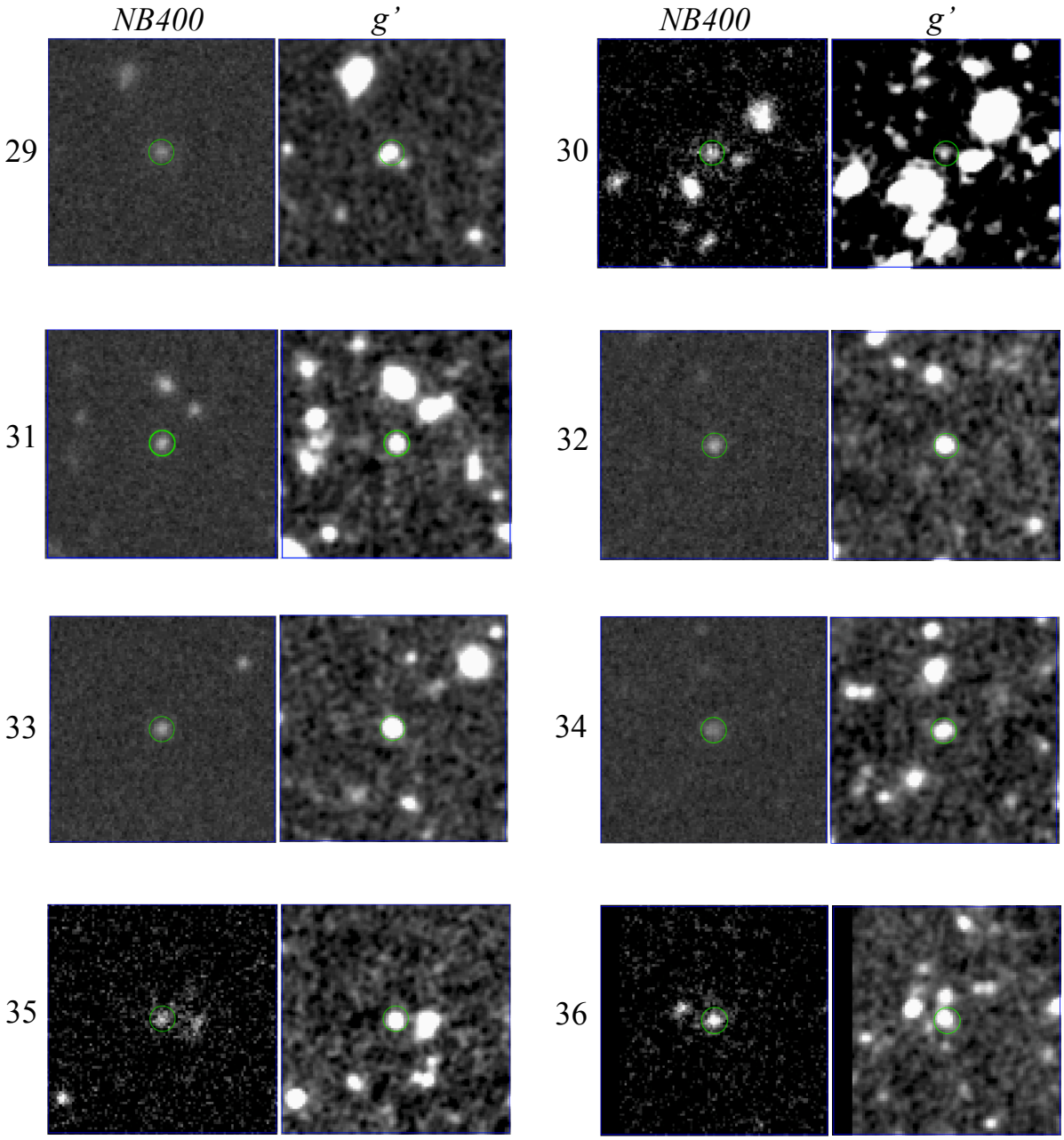
NB400
g'
NB400
g'
29
30
31
32
33
34
35
36

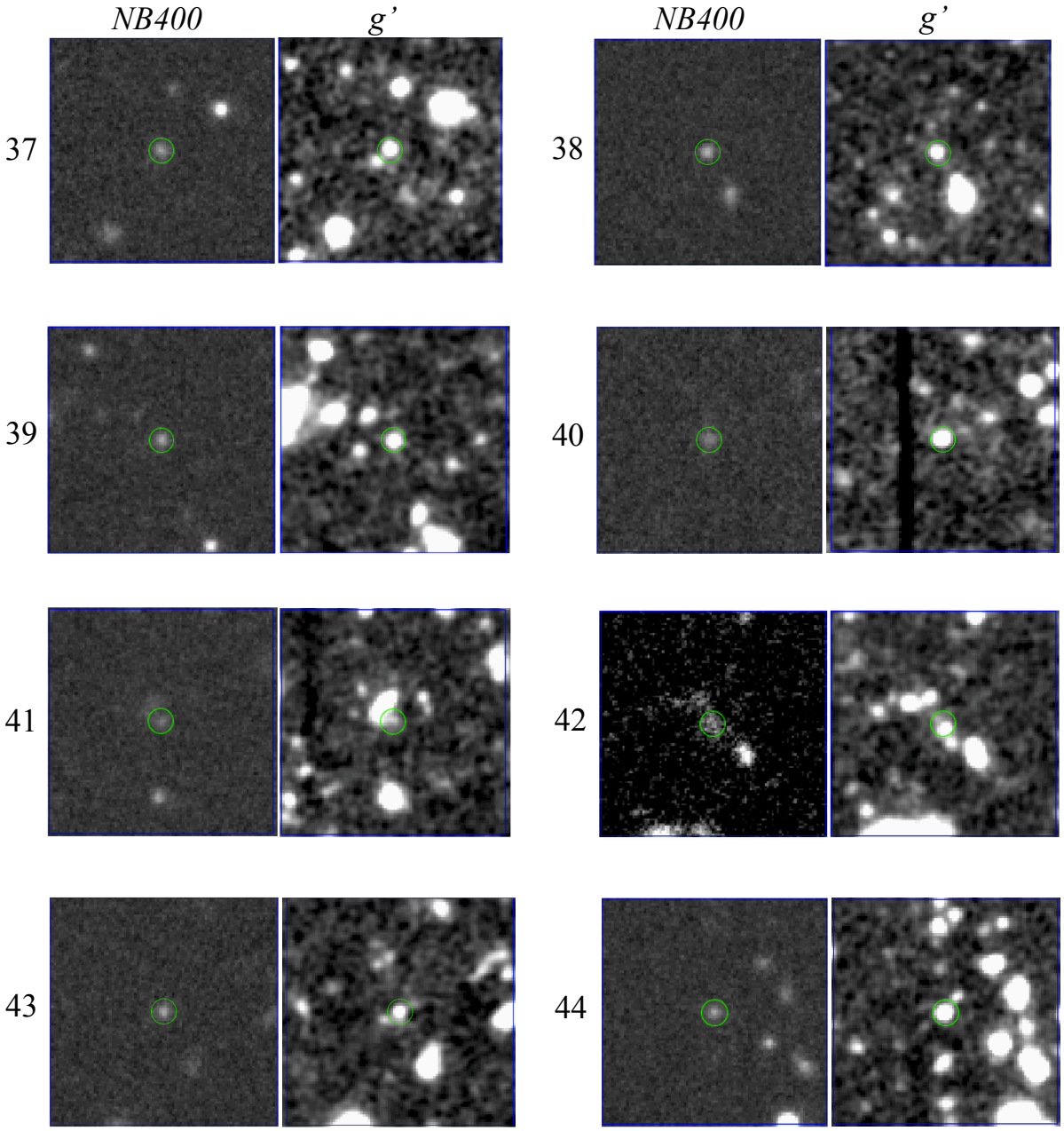
NB400
g'
NB400
g'
37
38
39
40
41
42
43
44

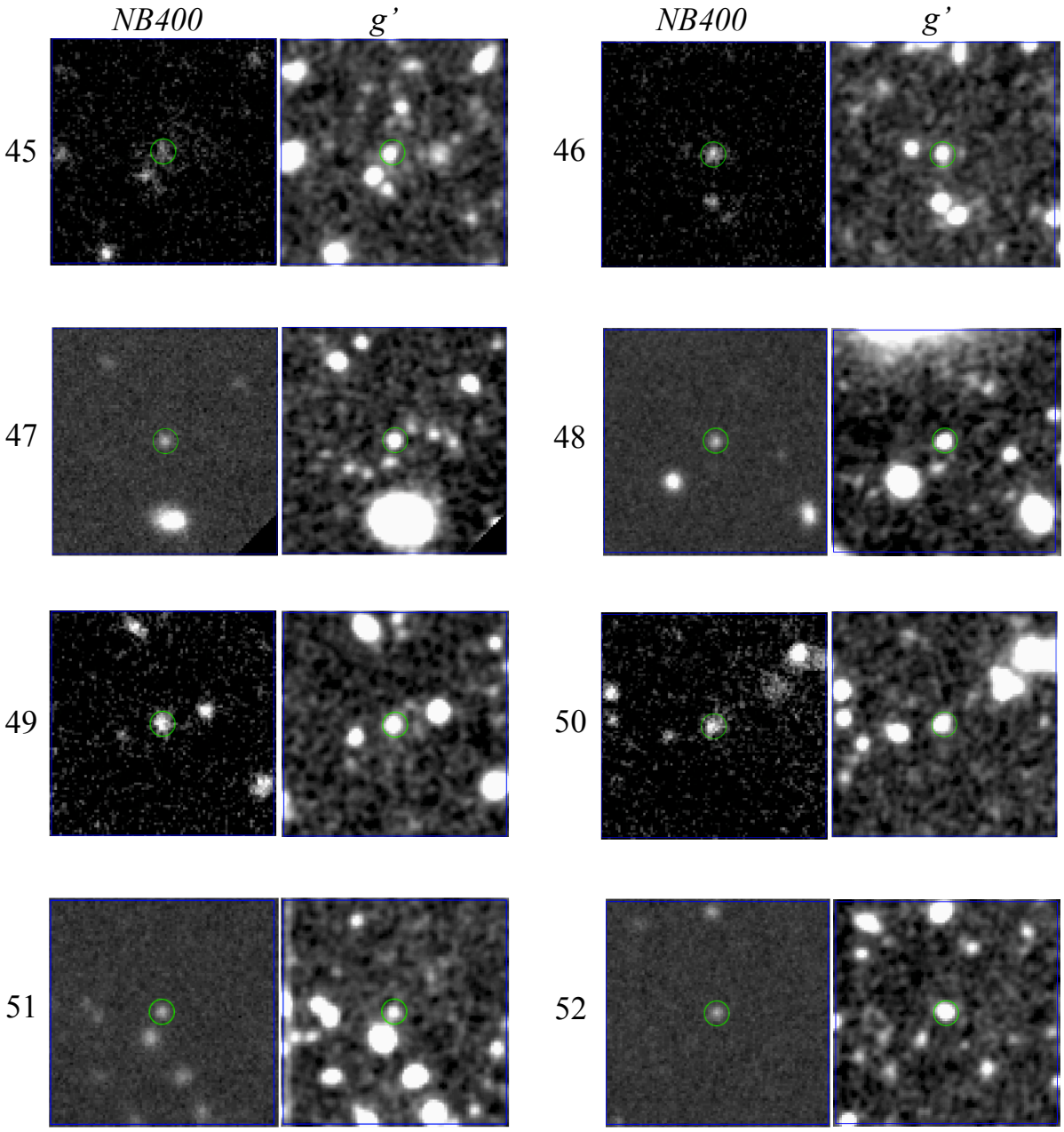
NB400
g'
NB400
g'
45
46
47
48
49
50
51
52

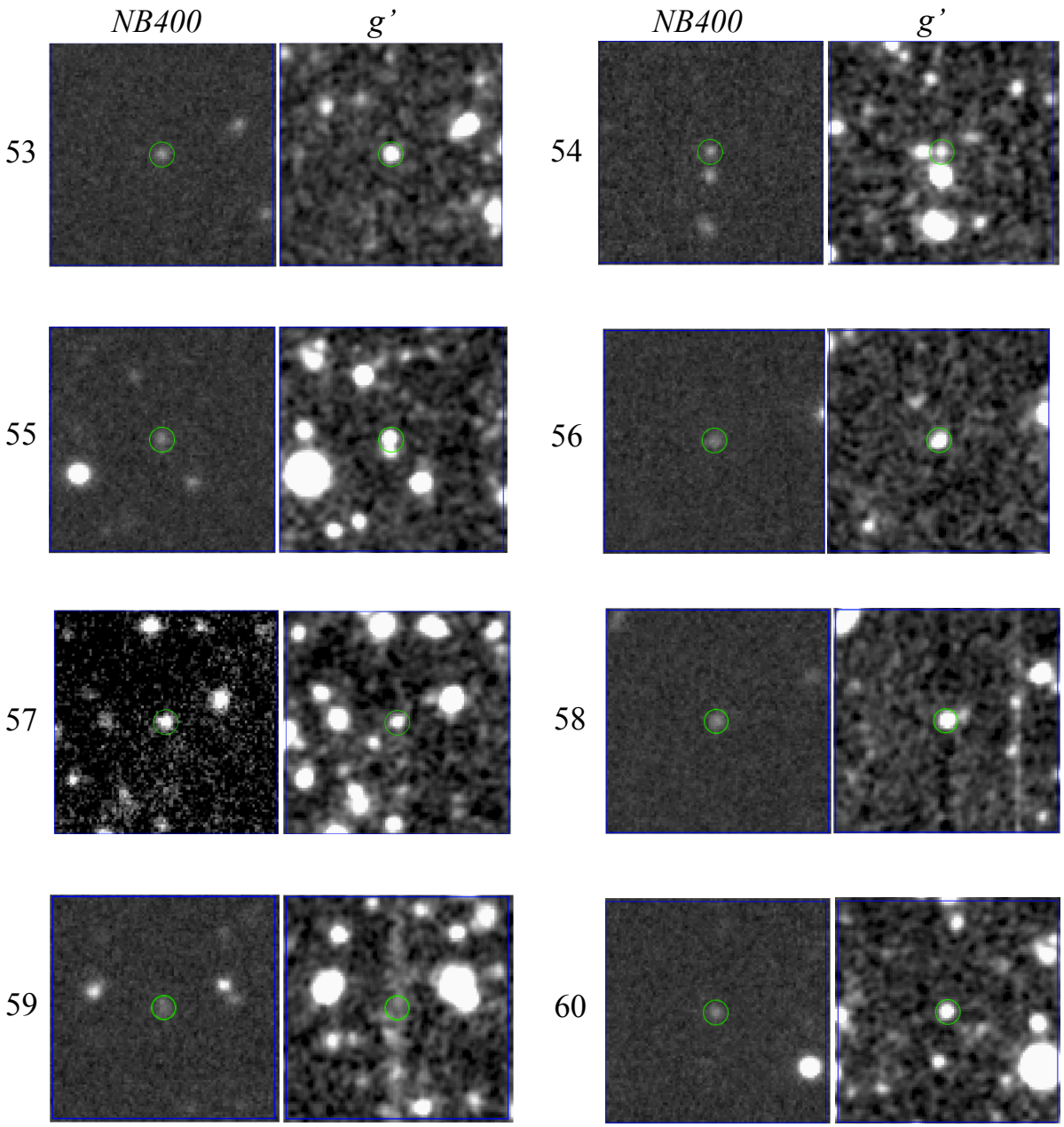
NB400
g'
NB400
g'
53
54
55
56
57
58
59
60

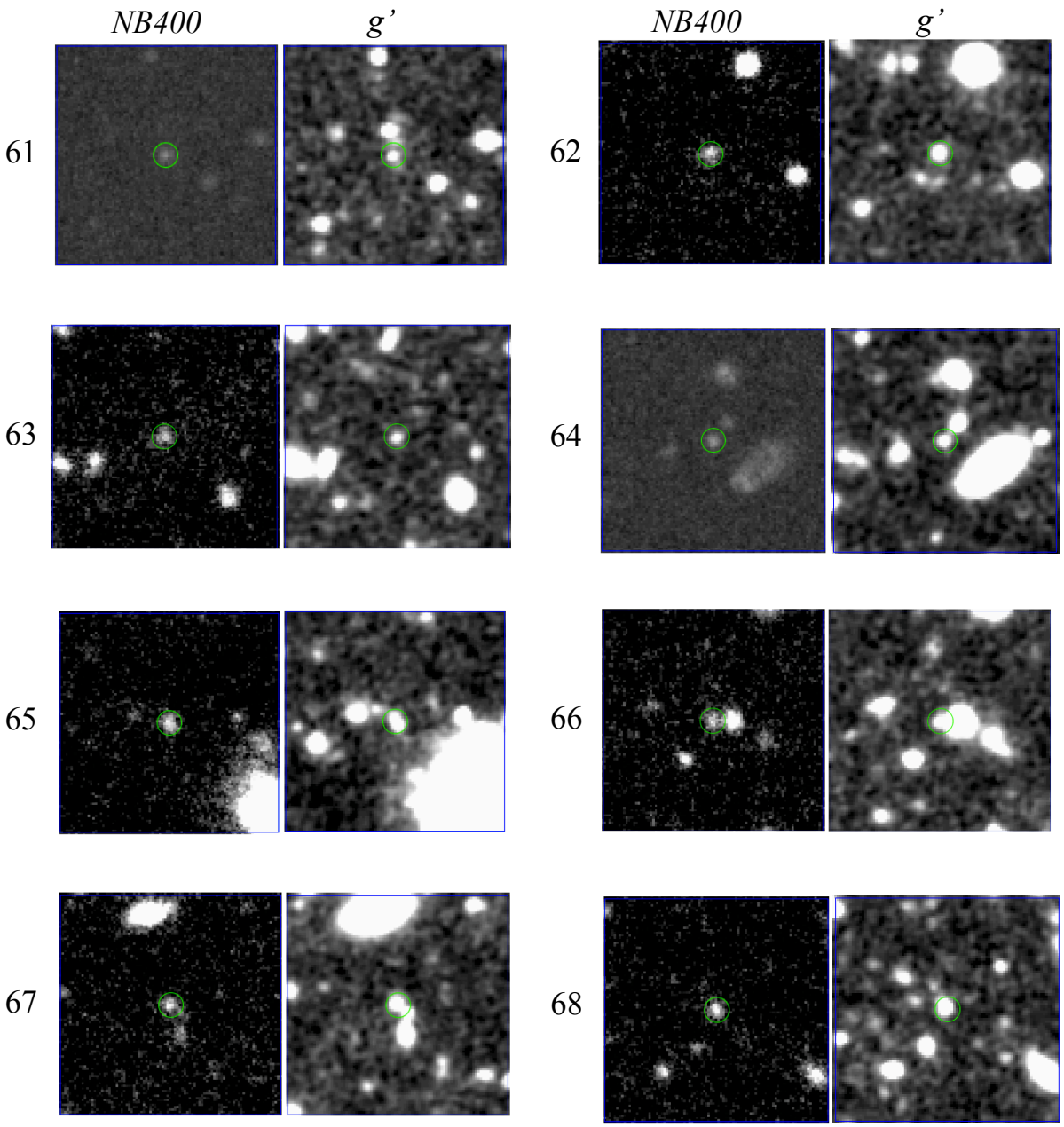
NB400
g'
NB400
g'
61
62
63
64
65
66
67
68

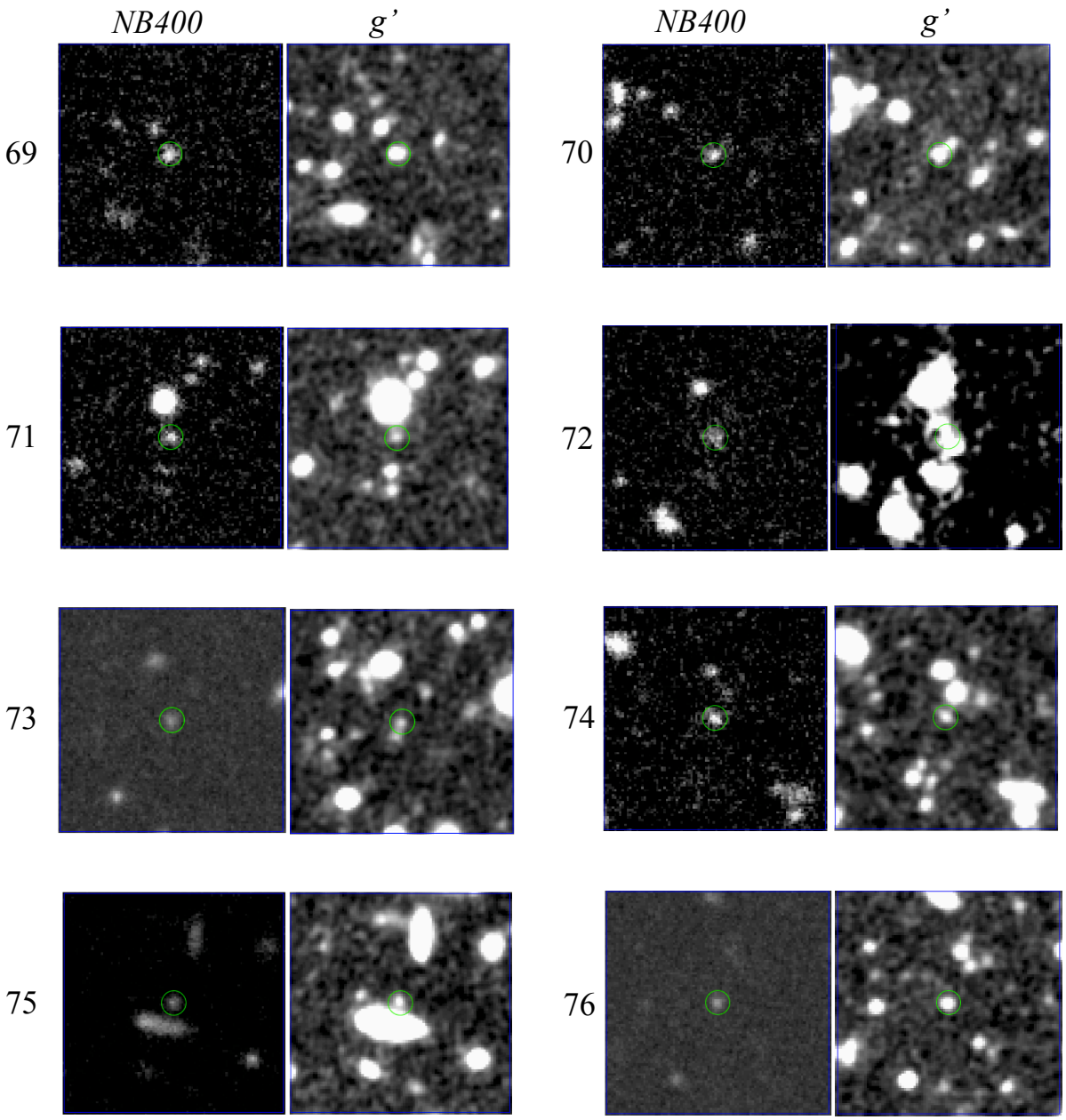
NB400
g'
NB400
g'
69
70
71
72
73
74
75
76

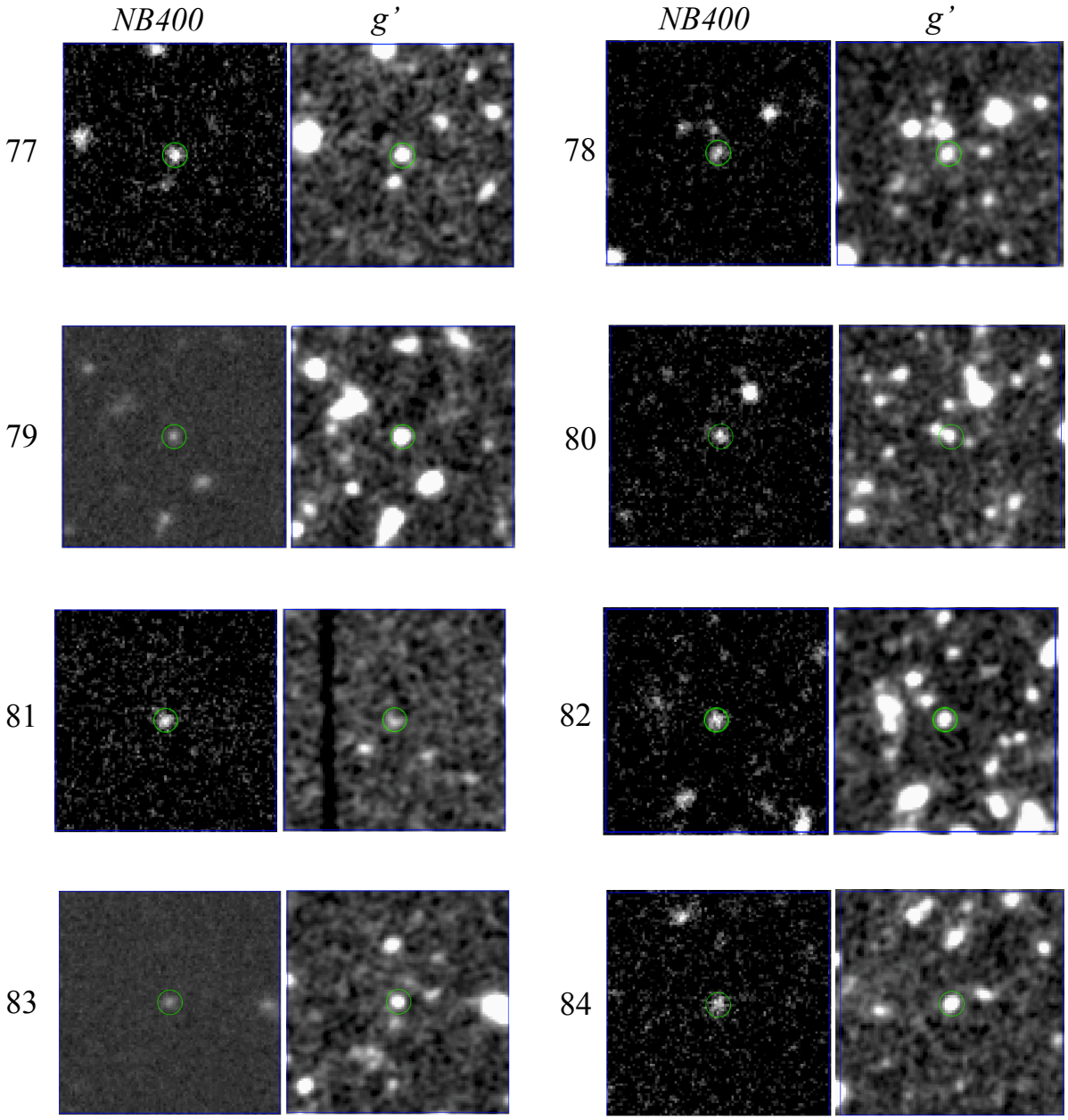
NB400
g'
NB400
g'
77
78
79
80
81
82
83
84

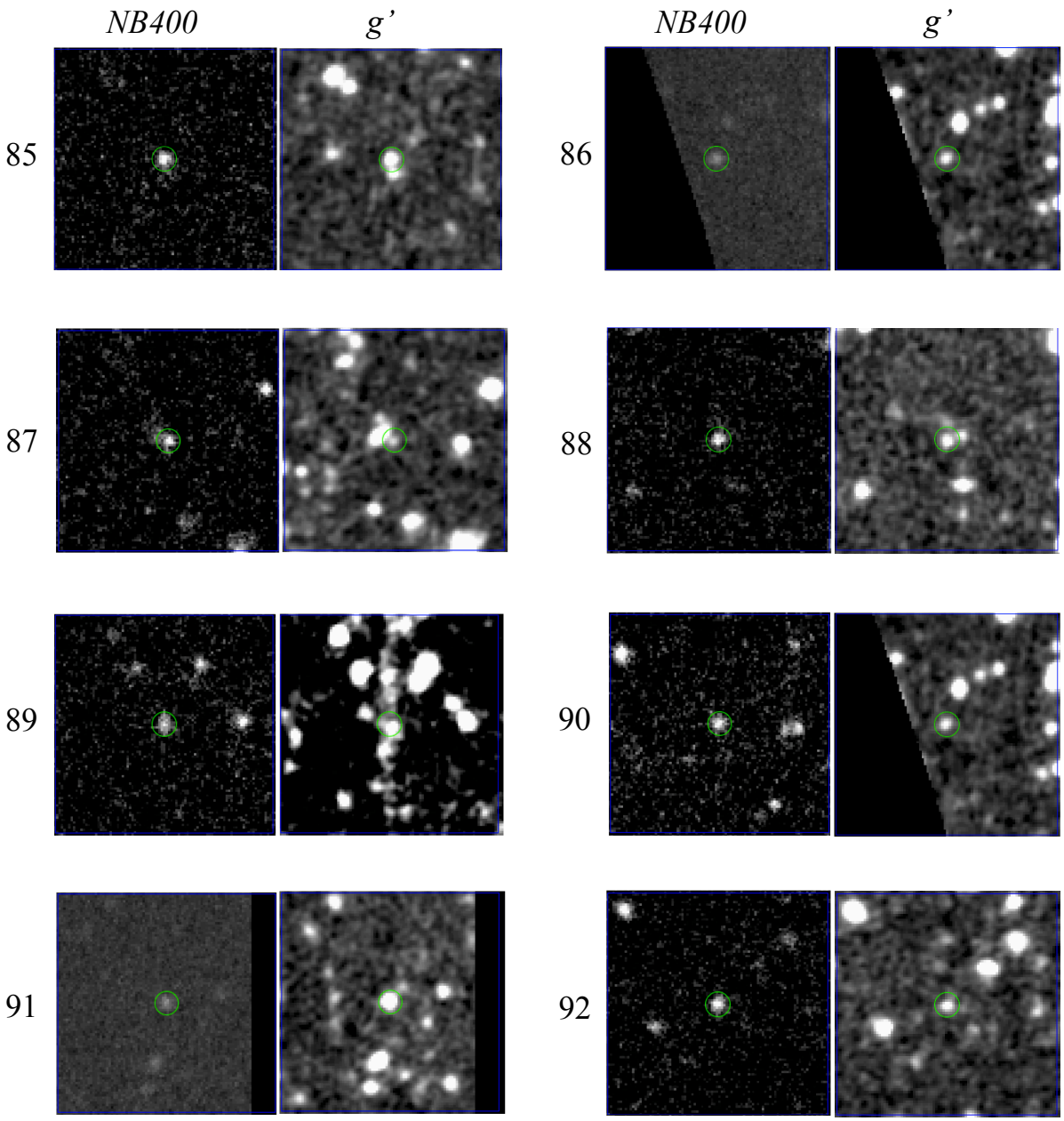
NB400
g'
NB400
g'
85
86
87
88
89
90
91
92

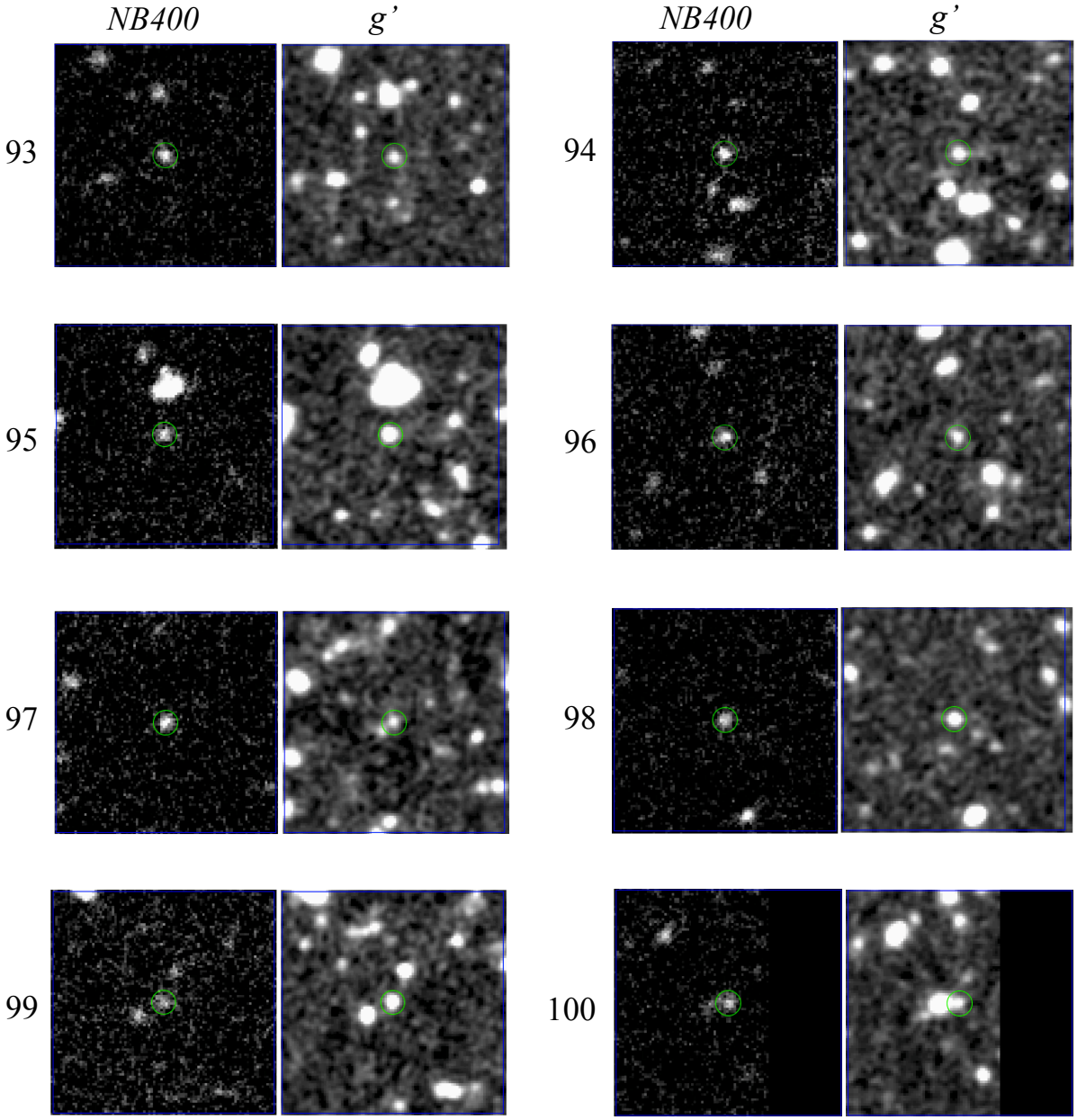
NB400
g'
NB400
g'
93
94
95
96
97
98
99
100

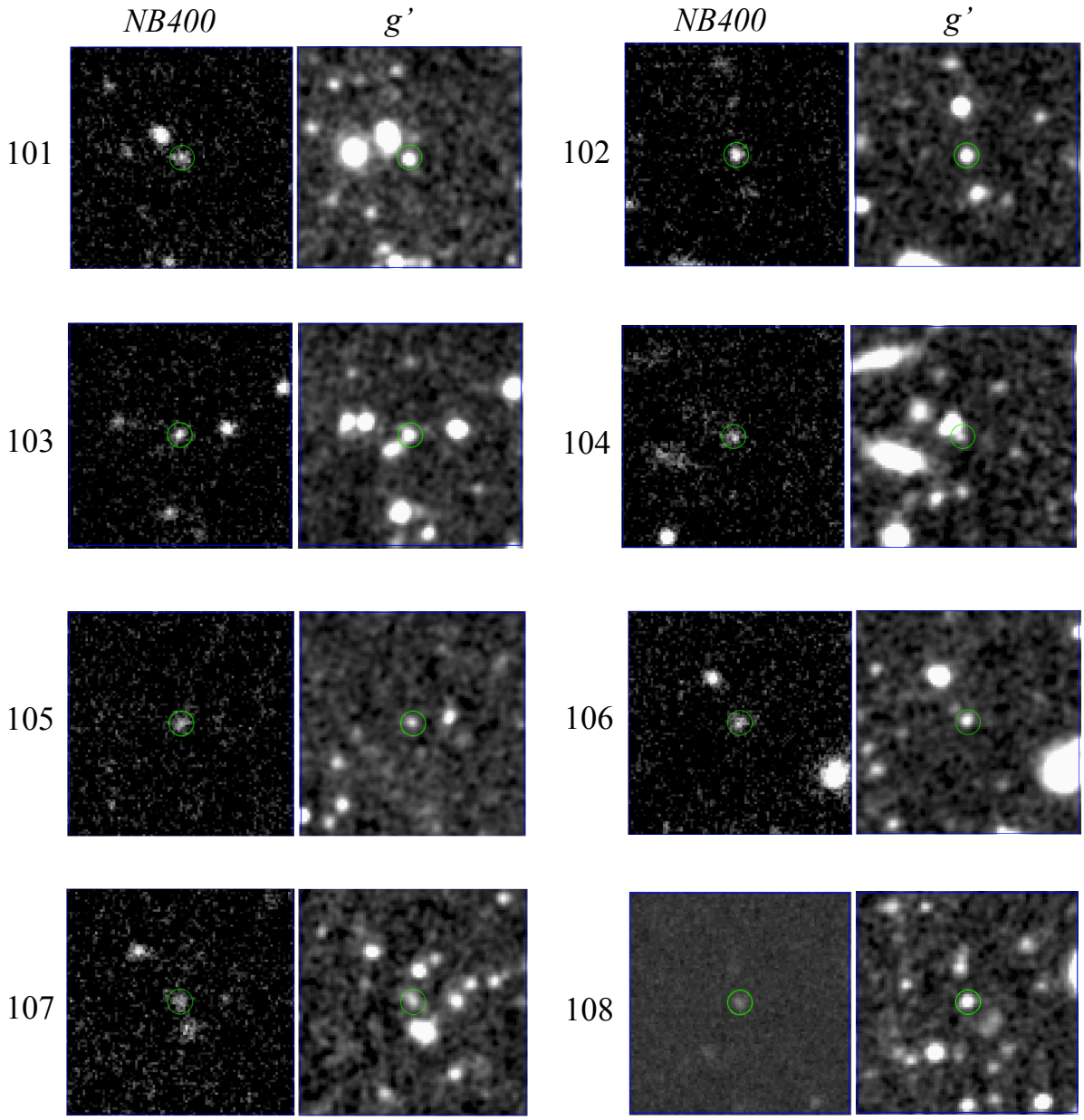
NB400
g'
NB400
g'
101
102
103
104
105
106
107
108

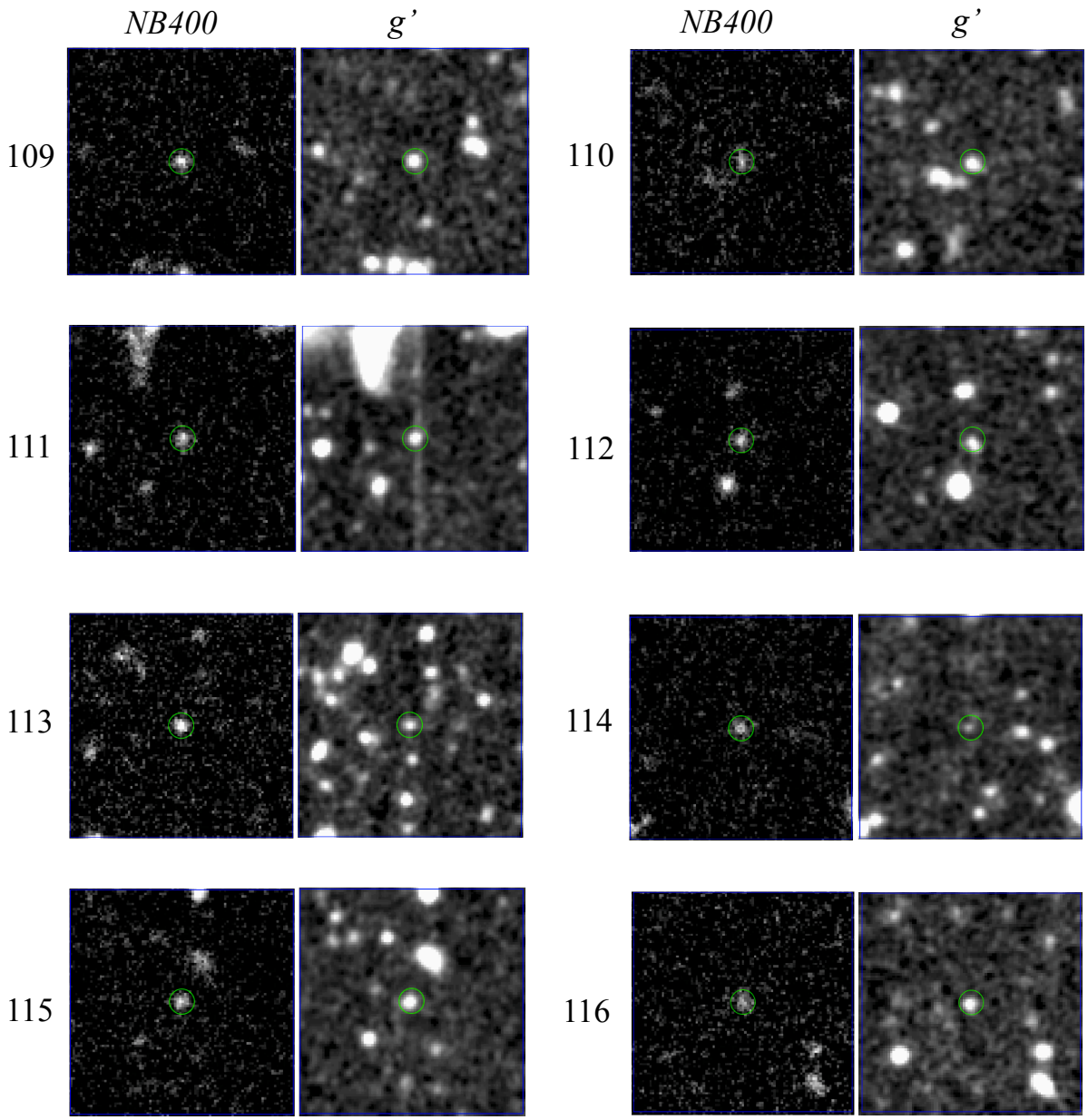
NB400
g'
NB400
g'
109
110
111
112
113
114
115
116

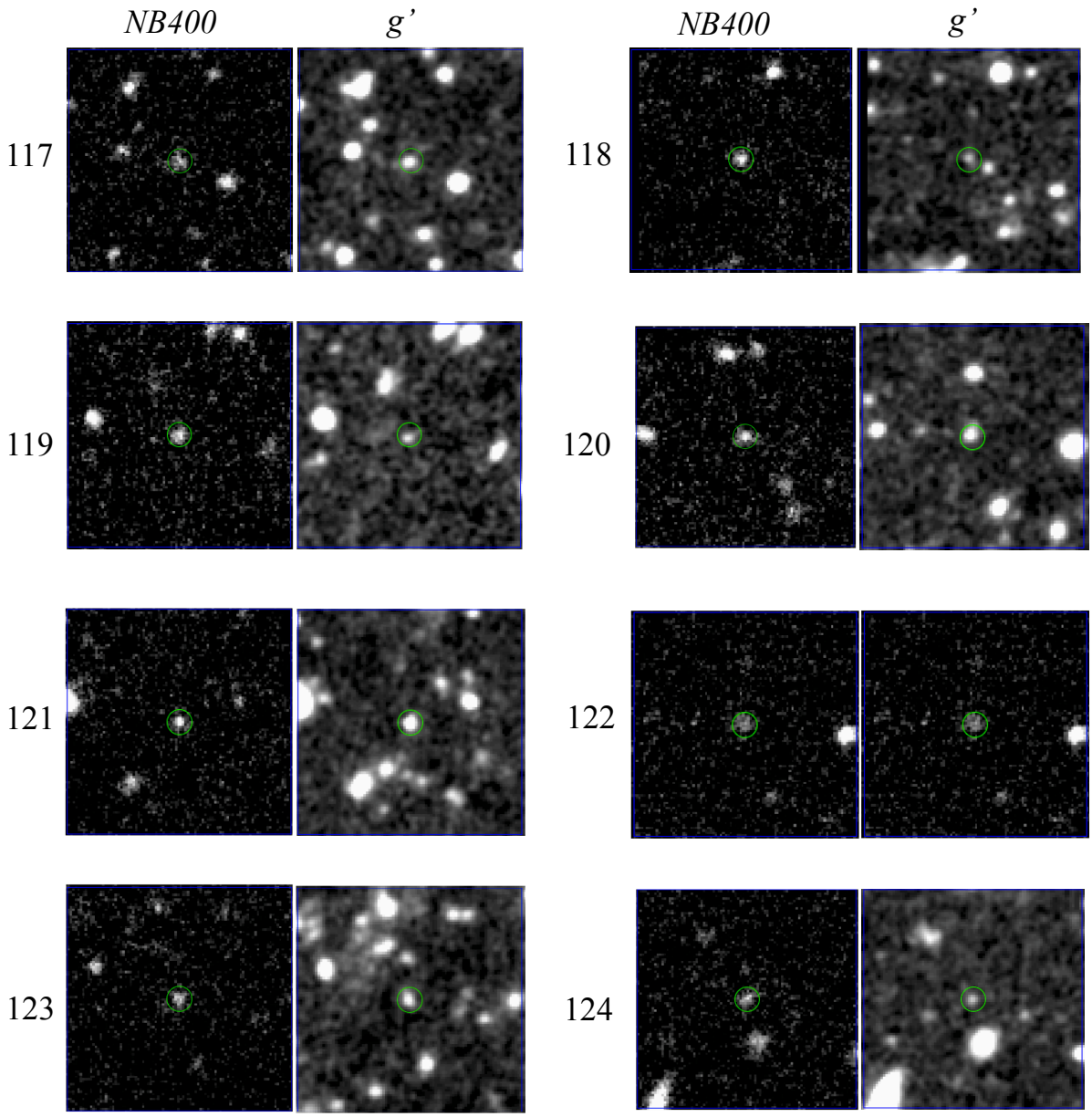
NB400
g'
NB400
g'
117
118
119
120
121
122
123
124

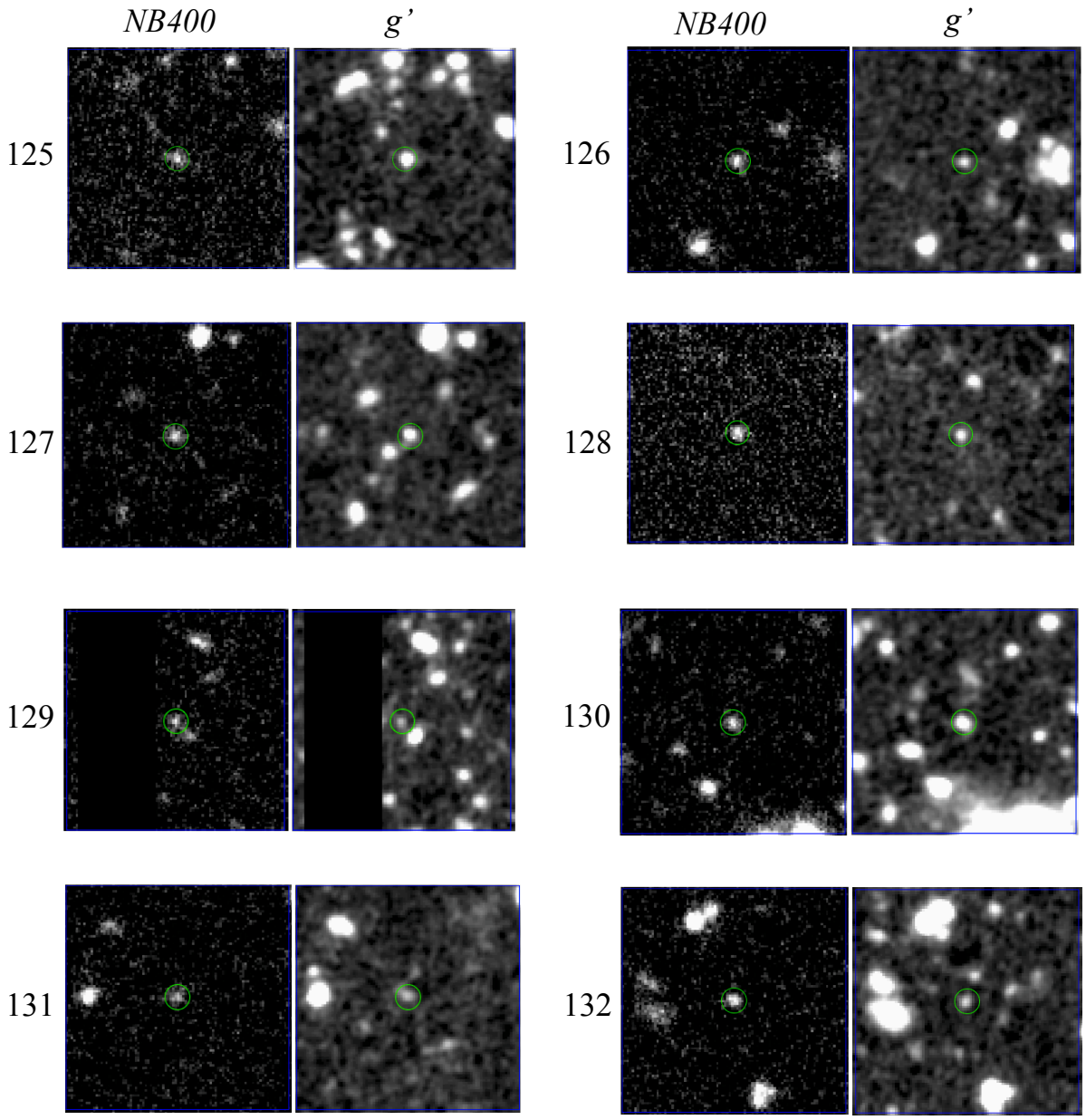
NB400
g'
NB400
g'
125
126
127
128
129
130
131
132

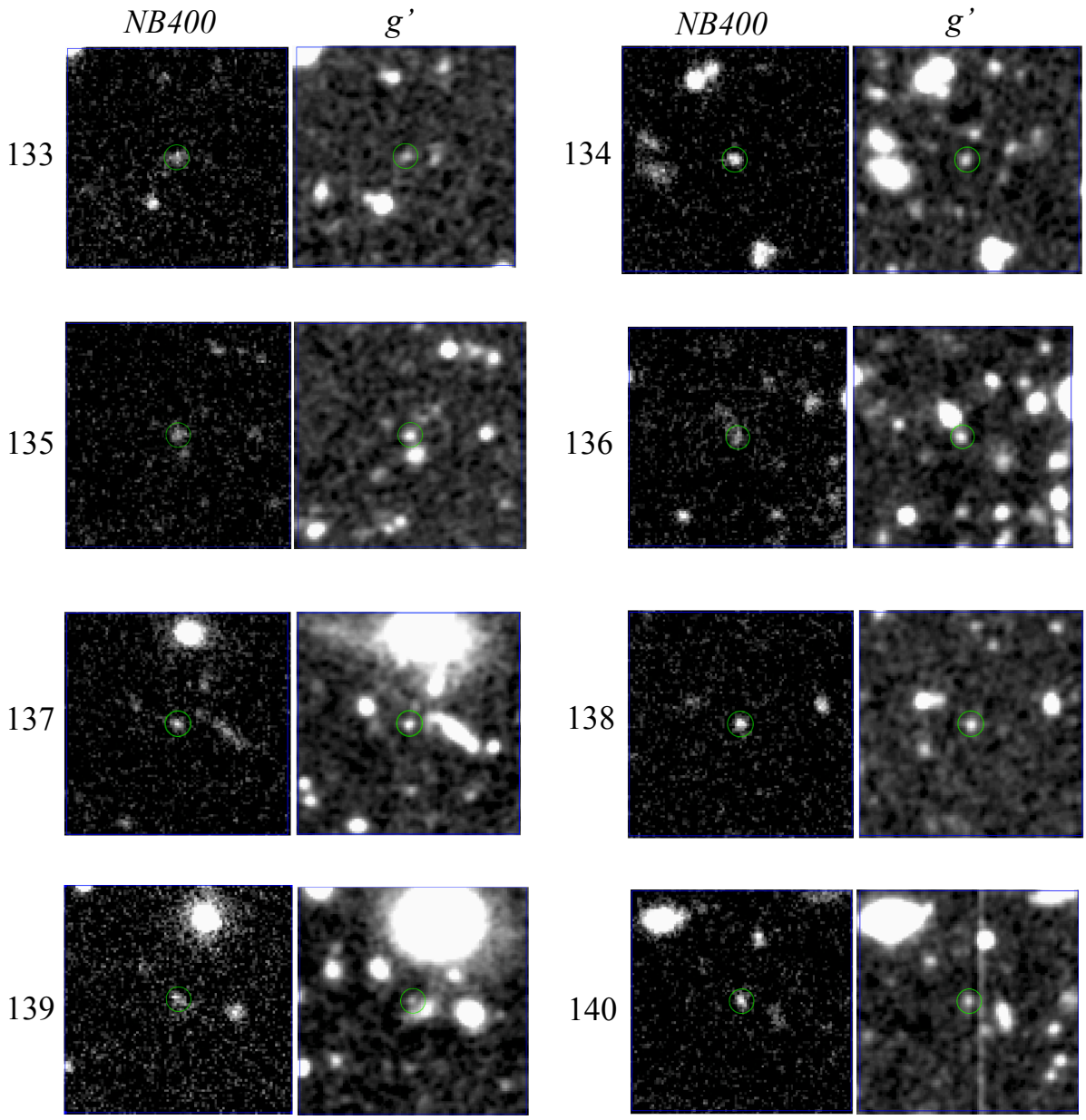
NB400
g'
NB400
g'
133
134
135
136
137
138
139
140

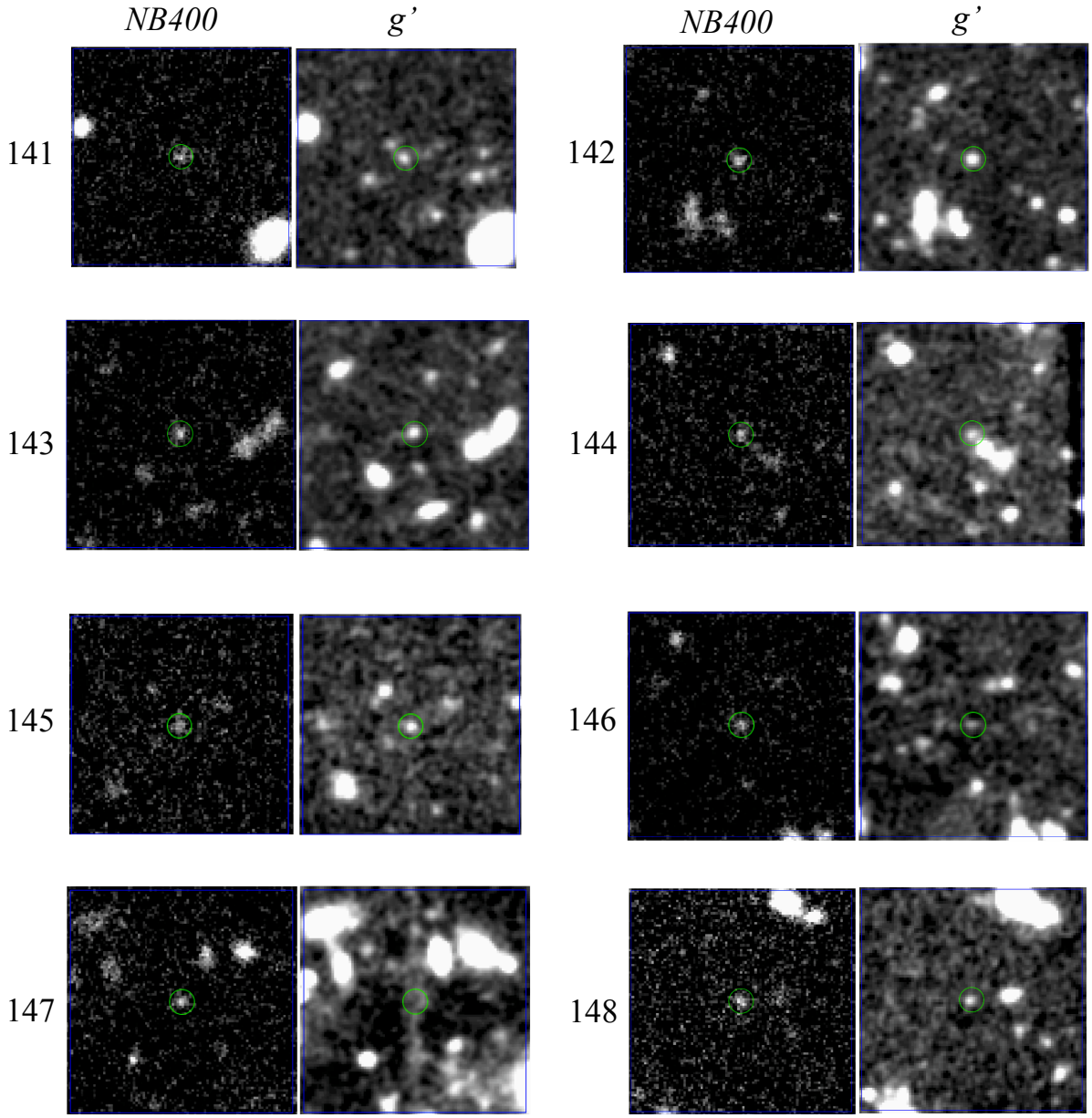
NB400
g'
NB400
g'
141
142
143
144
145
146
147
148

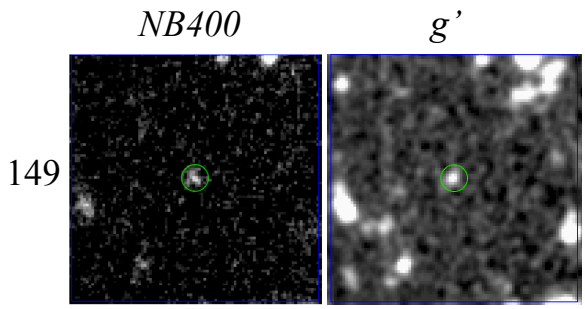
NB400
g'
149

Appendix B

TOWARD SYSTEMATIC EXPLORATIONS FOR HIGH-z DLA COUNTERPARTS WITH OPTICAL WIDE AND DEEP SURVEYS

To understand the early phase of the galaxy evolution, it is important to identify optical counterparts of high-z DLAs since they are thought to be a major gas reservoir for the star-formation. However, there are some scenarios for the origin of DLAs and we are still unable to discriminate them because only limited number of high-z DLA counterparts have been identified so far. To increase the identified high-z DLA counterparts, wide-field deep surveys are required. Recently, there are many completed, ongoing, and near-future wide-field deep optical imaging surveys. The combination of such surveys and a large sample of DLAs enables us to carry out systematic explorations for counterparts of high-z DLAs. Since the redshift distribution of BOSS DLAs peaks at $z \sim 2-2.5$ where the cosmic SFRD also shows its peak, $z \sim$2 is the most interesting redshift to study the early phase of the baryonic evolution of galaxies in which gas is being converted to stars. Among a number of wide-field surveys, we mainly focus on the survey with Subaru/Hyper Suprime-Cam (HSC) under the Subaru Strategic Program (HSC-SSP; Aihara et al., 2017a) because of the depth ($r = 26.1$, 5σ limit) of this survey over a wide area ($\sim$1,400 deg^2). To search for DLA counterparts, we have to select galaxies at the same redshift as DLAs. Although the photometric redshift technique is useful to derive redshifts based only on the photometric dataset, samples of $z \sim 2$ galaxies selected through the photometric redshift technique sometimes suffer from lower-redshift galaxies as contaminations. Also a complete selection of $z \sim 2$ galaxies is not always secured in the photometric redshift technique, though a high completeness is required for studies on high-redshift DLA counterparts. Therefore we have to consider a reliable selection method of galaxies at $z \sim 2$, not only the photometric redshift. Possible strategies to select galaxies at $z \sim 2$ are adopting the BMBX (with U, G, and R-bands) or BzK color selections. However these methods are not useful for the study with the HSC-SSP data because U-band data is not taken in the most part of the HSC-Wide fields and depths of public NIR surveys such as UKIDSS and VIKING are too shallow to select faint galaxies which could be counterparts of high-z DLAs.

Therefore, in this Appendix, we study the selection method of galaxies at $z \sim 2$ only with optical photometric data of HSC-SSP without relaying on U-band and NIR data. We then test

the reliability of our selection method by using the combination of the photometric redshift catalog of HSC-SSP and spectroscopic catalogs obtained by various surveys. Based on this examination, we show that the $(g-r)$ vs. $(r-y)$ diagram can recover a large fraction of $z \sim 2$ objects which are not completely selected in the photometric redshift.

B.1 Data

First we describe a brief summary of the data used in this Appendix. Recently, there are a number of completed, ongoing, and planned surveys, such as the Canada–France–Hawaii Telescope Legacy Survey (CFHTLS[1]; e.g., Gwyn, 2012), the Kilo-Degree Survey (KiDS[2]; de Jong et al., 2013), the Dark Energy Survey (DES[3]; Flaugher, 2005; Flaugher et al., 2015), the Panoramic Survey Telescope and Rapid Response System (Pan-STARRS[4]; Chambers et al., 2016), the survey with Hyper Suprime-Cam (HSC; Miyazaki et al., 2012) under the Subaru Strategic Program (HSC-SSP[5]; Aihara et al., 2017b), the Large Synoptic Survey Telescope (LSST[6]; Ivezic et al., 2008) project, and so on. The combination of these optical imaging surveys and the BOSS DLA enables us to search for high-z DLA counterparts systematically. In Table B.1, we show the information of the completed, ongoing, and future major optical surveys with a high sensitivity and wide area. Figure B.1 shows the diagram comparing the depth (5σ limiting magnitude in the r-band) and the area of each survey.

Toward the systematic identification of high-z DLA counterparts, we focus on the HSC-SSP dataset because of the depth and wideness of this survey. Based on the previous identifications of optical counterparts of DLAs at high-z, now it is known that they show relatively low SFRs (down to $\sim 1\ M_{\odot}\ \mathrm{yr}^{-1}$; Fumagalli et al., 2010; Péroux et al., 2012; Bouché et al., 2013; Fynbo et al., 2013; Krogager et al., 2013; Srianand et al., 2016). Since $SFR \sim 1\ M_{\odot}\ \mathrm{yr}^{-1}$ at $z \sim 2$ corresponds to $r \sim 26$, wide-field imaging surveys with a limiting depth of $r \sim 26$ or deeper are required to identify high-z DLA counterparts. As shown in Table B.1 and Figure B.1, the area of surveys whose limiting magnitude is deeper than ~ 26 is limited to $\sim 10\ \mathrm{deg}^2$ or less. On the other hand, the HSC-SSP survey reaches down to $r \sim 26$ in the HSC-Wide fields over $\sim$1,400 deg^2 and thus this survey is very powerful for high-z DLA studies.

The HSC-SSP photometric data

Here we describe the details of the HSC-SSP survey. Observations with Subaru/HSC under the SSP have started in March 2014. 300 nights over ~ 5 years are allocated for the HSC-SSP observations. Here it should be noted that HSC is a successor of Suprime-Cam, the former

[1] http://www.cfht.hawaii.edu/Science/CFHTLS/
[2] http://kids.strw.leidenuniv.nl/index.php
[3] https://www.darkenergysurvey.org/
[4] https://panstarrs.stsci.edu/
[5] http://hsc.mtk.nao.ac.jp/ssp/
[6] https://www.lsst.org/

Table B.1: The information of major imaging surveys.

Survey	Depth (5σ in r)	Area (deg^2)	Status
HSC-Wide	26.1	1400	Ongoing
HSC-Deep	27.1	15	Ongoing
HSC-UltraDeep	27.7	2	Ongoing
SDSS	23.0	14500	Completed
CFHTLS Wide	24.8	170	Completed
CFHTLS Deep	26.6	4	Completed
COSMOS	26.7	2	Completed
Pan-STARRS1 3π	23.5	30000	Ongoing
Pan-STARRS1 Medium-Deep	25.7	70	Ongoing
SkyMapper	23.4	20000	Ongoing
KiDS	25.2	1500	Ongoing
DES	25.0	5000	Ongoing
LSST	26.9	20000	Future

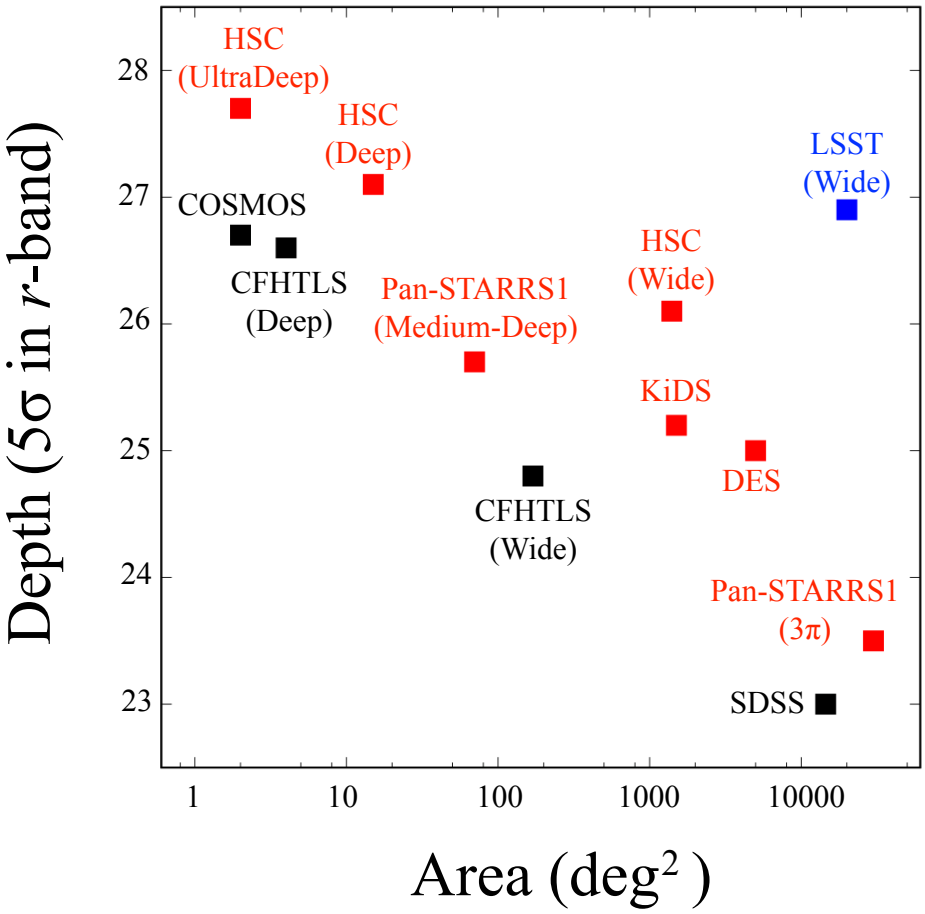

Fig. B.1: The diagram comparing the depth versus area of major imaging surveys. The depth is 5σ limiting magnitude in the r-band. Black, red, and blue filled squares show the completed, ongoing, and future surveys, respectively.

wide-field optical imager of the Subaru telescope. The field-of-view of HSC ($\sim$1.8 deg^2) is $\sim$7 times wider than that of Suprime-Cam ($\sim$0.25 deg^2). Table B.2 shows the general information of HSC. Survey fields for the HSC-SSP are chosen to overlap with SDSS and Pan-STARRS1 survey (Chambers et al., 2016) for the accurate calibration. There are three layers in the HSC-SSP survey; i.e., Wide, Deep, and UltraDeep. We show the fields of these 3 layers of the HSC-SSP survey in Figure B.2, with the sky distribution of the BOSS DLAs. The total survey areas of the Wide, Deep, UltraDeep fields as of the completion of the HSC-SSP survey are $\sim$1400 deg^2, $\sim$27 deg^2, and $\sim$3.5 deg^2, respectively. Table B.3 shows the summary of the HSC fields. In the HSC-SSP observations, 5 broad-band (BB) filters (g, r, i, z and y) and 4 NB filters ($NB387$, $NB816$, $NB921$, and $NB101$) are used. Figure B.3 shows the filter response curves of the HSC filters used for the HSC-SSP survey. All five BB filters are used in all HSC fields, while NB filters are used only in the Deep and/or UltraDeep fields. Table B.4 shows the filters used in each HSC layer and the expected depth of observations. Although the observations are now ongoing, a part of the data has already been released (Aihara et al., 2017a). The survey will continue until 2019.

HSC-SSP photometric redshift sample

The photometric redshift technique is useful to search for candidates of DLA counterparts. Based on 5-band photometric data obtained by HSC-SSP, some photometric catalogs made in different ways independently are available. HSC-SSP photometric redshifts are most accurate at $0.2 \lesssim z \lesssim 1.5$ since Balmer/4000 Å break of galaxies at this redshift range is located at optical wavelength range. More specifically, at $0.2 \lesssim z \lesssim 1.5$, $\sigma(\Delta z_{\rm ph}/(1+z_{\rm ph})) \sim 0.05$. In the HSC-SSP, the photometric redshift is calculated by some codes by using template fitting, empirical fitting, and machine-learning techniques. In this study, we specifically focus on the photometric redshift calculated by template fitting-code Mizuki (Tanaka, 2015; Tanaka et al., 2017). The template fitting technique is useful for studies on detailed properties of galaxies since physical properties (e.g., SFR, stellar mass, and so on) for each galaxy are derived straightforwardly.

BOSS DLAs in the HSC fields

As for the DLA sample, we use the catalog of DLAs provided by Noterdaeme et al. (2012a). This catalog is based on the quasar catalog of BOSS (Pâris et al., 2012) based on the SDSS DR9 (Ahn et al., 2012). The BOSS DR9 quasar catalog includes 87,822 quasars over $\sim$3,275 deg^2. From this sample Noterdaeme et al. (2012a) found 12,801 Lyα absorbers with $N_{\rm HI} > 10^{20}$ cm^{-2}. Note that this sample includes not only DLAs (absorbers with $N_{\rm HI} \geq 2 \times 10^{20}$ cm^{-2}) but also sub-DLAs ($10^{19} < N_{\rm HI} < 2 \times 10^{20}$ cm^{-2}). Since Péroux et al. (2003) show that sub-DLAs also contribute to a large fraction of the neutral gas content in the high-z Universe, we do not remove sub-DLAs from the sample.

From 12,801 DLAs in the BOSS DLA catalog, 3,577 DLAs will be covered by the HSC-SSP observations when the HSC-SSP survey is completed. Note that there are some quasar

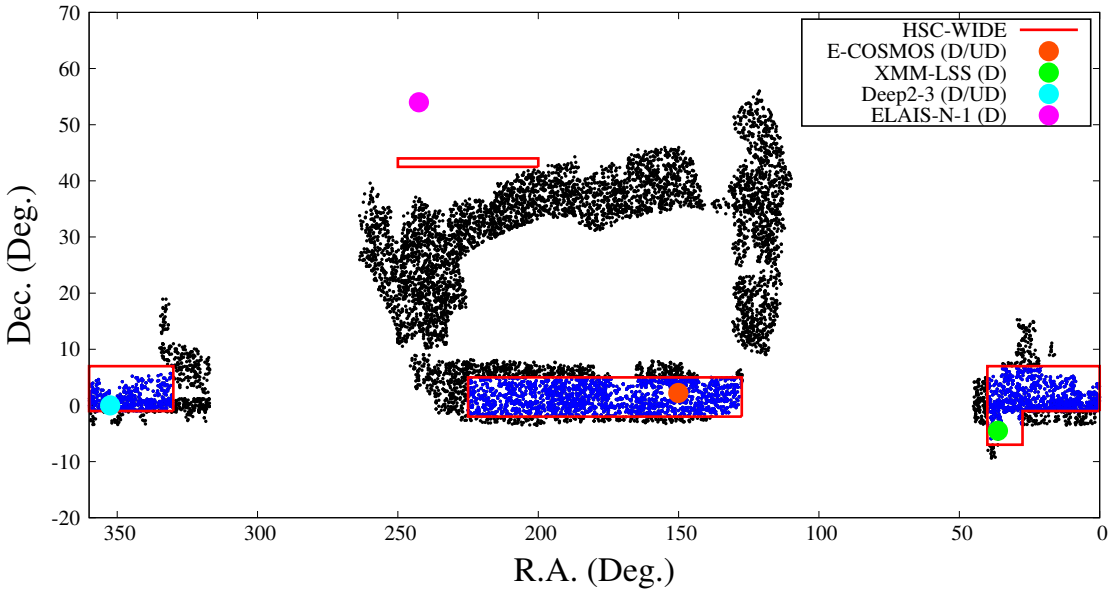

Fig. B.2: The spatial distribution of the BOSS DR9 quasars and the HSC fields. Black and blue dots show BOSS DLAs and those covered by the HSC-SSP observations, respectively. The HSC-Wide fields are denoted with red solid lines. Filled colored circles show Deep (D) and Ultra Deep (UD) fields.

Table B.2: General information of Subaru/HSC

Detectors	Hamamatsu Photonics KK 2048×4096 (S10892-02)
Number of CCDs	104 for science
Pixel size	15 μm
Pixel scale	$0.168''$
Field-of-view	~ 1.8 deg^2 (1.5 degree diameter)

Table B.3: Survey fields of HSC-SSP

Layer	Field	Area (deg^2)	(RA, Dec)
Wide	North field	∼90	13:20<RA<16:40 & 42<Dec<44.5 deg.
	Spring equatorial field	∼680	09:00<RA<15:30 & –2<Dec<5 deg.
	Fall equatorial field	∼630	22:00<RA<02:40 & –1<Dec<7 deg.
Deep	XMM-LSS	∼5.4	(02:23:15:33, –05:18:30:67)
			(02:22:22.43, –04:03:44.48)
			(02:27:19.86, –04:27:47.42)
	E-COSMOS	∼7.2	(02:23:15:33, –05:18:30:67)
			(09:57:28.60, +02:57:21.00)
			(10:03:28.60, +02:57:21.00)
			(09:57:28.60, +01:27:21.00)
			(10:03:28.60, +01:27:21.00)
	ELAIN-N1	∼7.2	(02:23:15:33, –05:18:30:67)
			(16:11:00.81, +53:56:30.71)
			(16:15:46.66, +54:59:17.74)
			(16:10:54.07, +56:02:49.65)
			(16:06:16.19, +54:59:16.91)
	Deep2-3	∼7.2	(02:23:15:33, –05:18:30:67)
			(23:32:08.46, +00:16:49.43)
			(23:27:02.16, +00:16:49.41)
			(23:29:26.53, –00:50:38.94)
			(23:24:12.60, –00:49:46.61)
UltraDeep	SXDS	∼1.8	(02:18:15.60, –04:51:00.00)
	COSMOS	∼1.8	(10:00:28.60, +02:12:21.00)

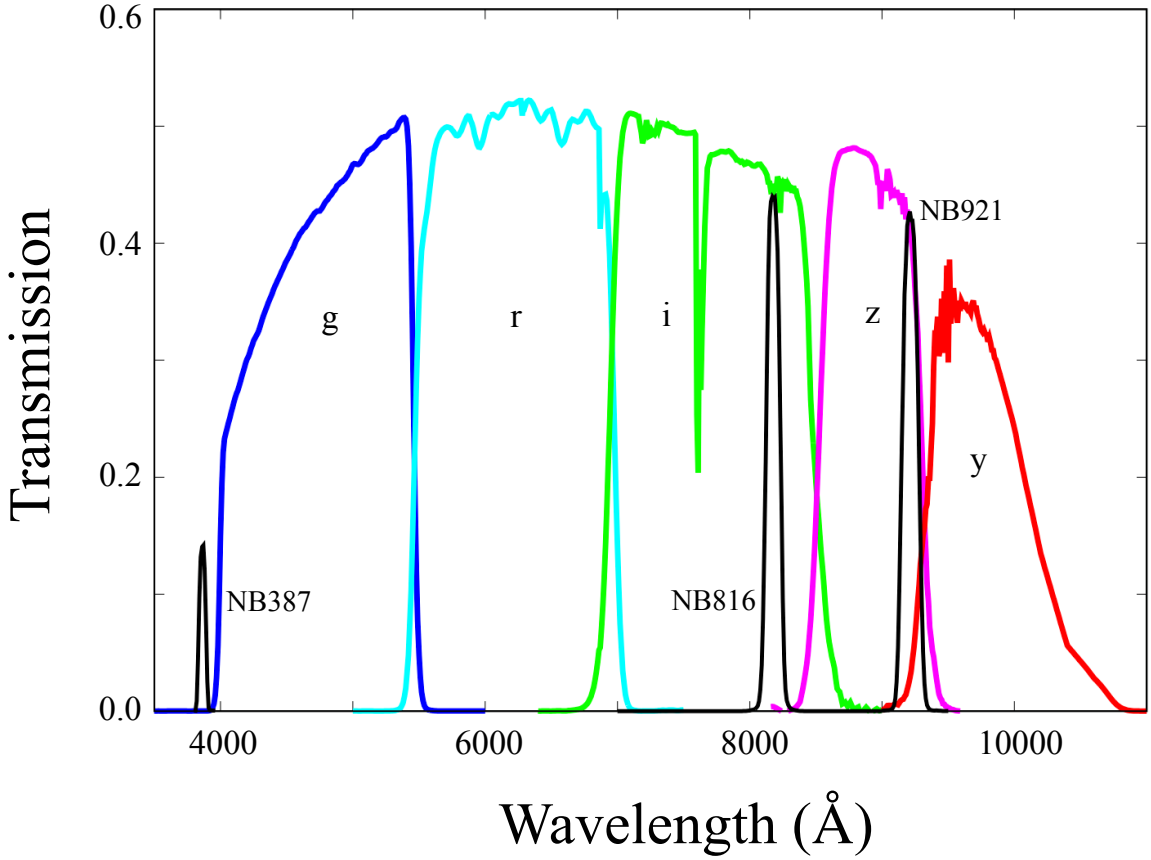

Fig. B.3: The response curve of the HSC filters. Colored curves show the response curves of broad-band filters (g, r, i, z, and y-band, from left to right) while black curves show those of NB filters ($NB387$, $NB816$, and $NB921$, from left to right). Note that, the filter response curve of $NB101$ is not shown in this figure since it is not publicly available as of July 2017.

Table B.4: Filter used in each HSC field and the expected depth of observations

Layer	Filters	Depth
Wide	g, r, i, z, y	$r \sim 26$ (5σ limit)
Deep	$g, r, i, z, y, NB387, NB816, NB921$	$r \sim 27$ ($NB \sim 25-26$)
Ultra deep	$g, r, i, z, y, NB816, NB921, NB101$	$r \sim 28$ ($NB \sim 25-26.5$)

sightlines having multiple DLAs (the number of quasars whose spectrum shows more than 1 DLA is 2,820 in the HSC-SSP fields). Figure B.2 shows the sky distribution of DLAs in the HSC-SSP fields, and Figure B.4 shows the redshift distribution of the BOSS DLAs located in the HSC-SSP fields. Similar to the whole BOSS DLA sample (see Section 2.2), the redshift distribution of DLAs in the HSC-SSP fields shows its peak at $z \sim 2-2.5$. The average, median, and standard deviation of $z_{\rm abs}$ are 2.73, 2.61, and 0.54, respectively. Given these situations and also the deep sensitivity, the HSC-SSP is suitable for the systematic exploration for galaxy counterparts of DLAs at $z \sim 2$.

B.2 The completeness of the HSC-SSP photometric redshift for $z \sim 2$ galaxies

To identify DLA counterparts at high redshift, a complete selection of candidates is required. Although the photometric redshift technique is powerful to search for candidates of DLA counterparts, it sometimes derives a completely wrong redshift (so-called "catastrophic error"; e.g., Ilbert et al., 2006; Bernstein & Huterer, 2010). In particular, $z \sim 2$ galaxies show a similar SED to lower-z galaxies in the optical wavelength range, and thus we should carefully check the completeness of at $z \sim 2$ objects in the photometric redshift sample. We check the completeness of $z \sim 2$ objects selected through the photometric redshift, by comparing the photometric redshift with the spectroscopic information.

To examine the completeness of photometric redshift, we use a photometric redshift catalog in the HSC-Deep field made with the Mizuki code in the internal data release S16A (the catalog name is s16a_deep.photoz_mizuki). Although we plan to search for DLA counterparts in the HSC-Wide fields, the data in the HSC-Deep fields is more suitable for examining the completeness of the photometric redshift, since there are enough spectroscopic redshifts measured by various previous spectroscopic surveys. In the examination of the completeness, we only use objects whose SED is well-fitted by a template in the calculation of the photometric redshift, by adopting a selection criteria of "reduced_chisq ≤ 3" in the photometric redshift catalog (14,251,608 objects satisfy this criteria). As for the spectroscopic information, a catalog of spectroscopic redshift collected from the literature[7] is available in the HSC-SSP database (the catalog name is s16a_deep.specz; 142,289 objects are listed in this catalog), where the spectroscopic redshifts are linked to HSC objects though the object ID ("object_id" in the catalog). For indicating the confidence level of the spectroscopic redshift, each survey defines its own flags. In the spectroscopic redshift catalog in the HSC-SSP database, such flags are unified in the flag of "specz_flag_homogeneous". If specz_flag_homogeneous is TRUTH, the redshift is secure. We only use objects with "specz_flag_homogeneous = TRUTH" in the spectroscopic catalog (93,416 objects). For removing objects with uncertain spectroscopic redshift, further criterion

[7]Specifically, zCOSMOS DR3 (Lilly et al., 2009), UDSz (Bradshaw et al., 2013; McLure et al., 2013), 3D-HST (Skelton et al., 2014; Momcheva et al., 2016), FMOS-COSMOS (Silverman et al., 2015), VVDS (Le Fèvre et al., 2013), VIPERS PDR1 (Garilli et al., 2014), SDSS DR12 (Alam et al., 2015), GAMA DR2 (Liske et al., 2015), WiggleZ DR1 (Drinkwater et al., 2010), DEEP2 DR4 (Davis et al., 2003; Newman et al., 2013), and PRIMUS DR1 (Coil et al., 2011; Cool et al., 2013).

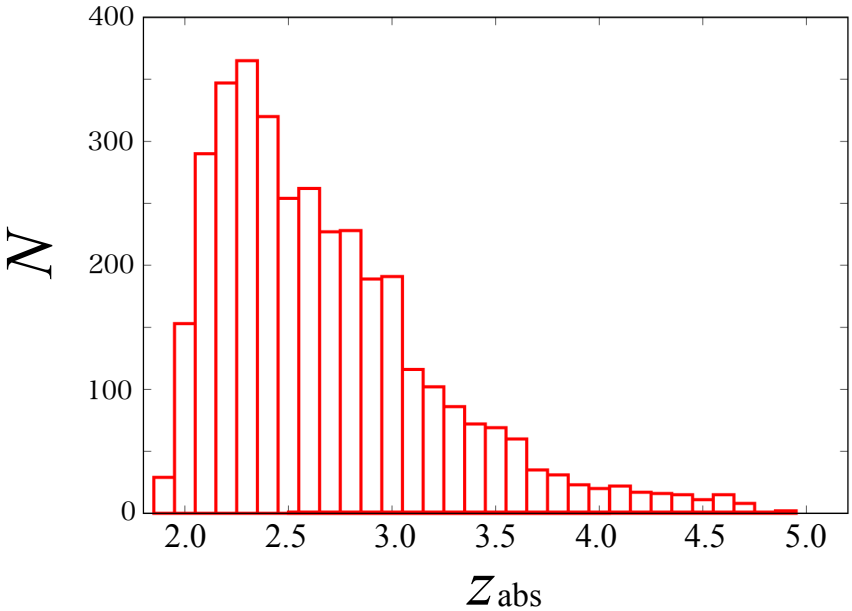

Fig. B.4: The redshift distribution of the BOSS DLAs covered by the HSC-SSP observations.

of "specz_redshift_err > 0" in the spectroscopic catalog was also adopted. After this selection, we achieved 37,397 objects with secure spectroscopic redshift. We then matched the photometric redshift catalog, the spectroscopic catalog, and the photometric catalog (s16a_deep.forced) by matching object_id, yielding 25,928 photometric redshift objects with a secure spectroscopic redshift. In some cases, the same objects are duplicated in multiple surveys with different spectroscopic redshifts. We removed such objects from the sample for the sake of simplicity. In the result, we obtained 25,822 objects as a final sample to examine the completeness of $z \sim 2$ objects in the HSC-SSP photometric redshift catalog.

Figure B.5 shows the diagram comparing the spectroscopic redshift ($z_{\rm sp}$) with the photometric redshift ($z_{\rm ph}$) of the sample described above. We show the frequency distribution of $z_{\rm ph}$ of the objects with $z_{\rm sp}$ of $2.0 \leq z_{\rm sp} \leq 2.5$ in Figure B.6. As seen in these figures, a large fraction of galaxies at $2.0 \leq z_{\rm sp} \leq 2.5$ are regarded as lower-z objects in the photometric redshift. Specifically, 219 ($\sim$44%) of 499 objects at $2.0 \leq z_{\rm sp} \leq 2.5$ have $z_{\rm ph}$ of $z_{\rm ph} \leq 1.5$. Therefore we miss significant fraction of $2.0 \leq z_{\rm sp} \leq 2.5$ objects if we rely only on the photometric redshift. A more complete selection method for galaxies at $2.0 \leq z_{\rm sp} \leq 2.5$ is required to search for DLA counterparts at $z \sim 2$.

B.3 Color selection of galaxies at $z \sim 2$

To select $z \sim 2$ galaxies, the BMBX (Steidel et al., 2004) and *BzK* (Daddi et al., 2004) selections are often used. The former requires the U, G, and R-bands while the latter needs the B, z, and K-bands. However, the U-band data are not always taken in wide-field deep surveys, since there are only few wide-field imagers with a high-sensitivity at U-band. Though there are some wide-field NIR surveys recently, such as UKIDSS (Lawrence et al., 2007) and VIKING (Arnaboldi et al., 2007), their depth is too shallow to select faint counterparts of high-z DLAs (with $SFR <$ a few $M_\odot$). Therefore we should develop a new selection method of galaxies at $z \sim 2$ without U-band nor NIR data. For selecting galaxies at $z \sim$2 without adopting the BMBX or *BzK* selections, we here investigate new selection methods only with optical photometric data. Figure B.7 shows the model SED of star-forming galaxies at various redshifts. In this figure, the model SED is made based on the model by Bruzual & Charlot (2003) assuming a constant-SFR model ($SFR = 1 M_\odot$ yr^{-1}) with the Salpeter IMF and the solar metallicity. As seen in Figure B.7, star-forming galaxies at $z = 2$ show a flat continuum over a wide optical wavelength range. By focusing on this flat continuum, we may be able to select star-forming galaxies at $z \sim$2 only with optical photometric data. Specifically, the magnitude difference (in the AB magnitude system) between each optical band should be close to zero. This means that when we plot $z \sim$2 galaxies in a color-color diagram in optical, they should be concentrated around zero both in the vertical and horizontal axes (as long as the AB magnitude is used). On the other hand, since galaxies at other redshift show break features in the optical wavelength range, they show different colors from $z \sim 2$ galaxies. Therefore we investigate the color-color diagram of galaxies at various redshift. Note that, although passive galaxies at $z \sim$2 show redder colors than star-forming galaxies at $z \sim 2$ in the optical wavelength, we ignore

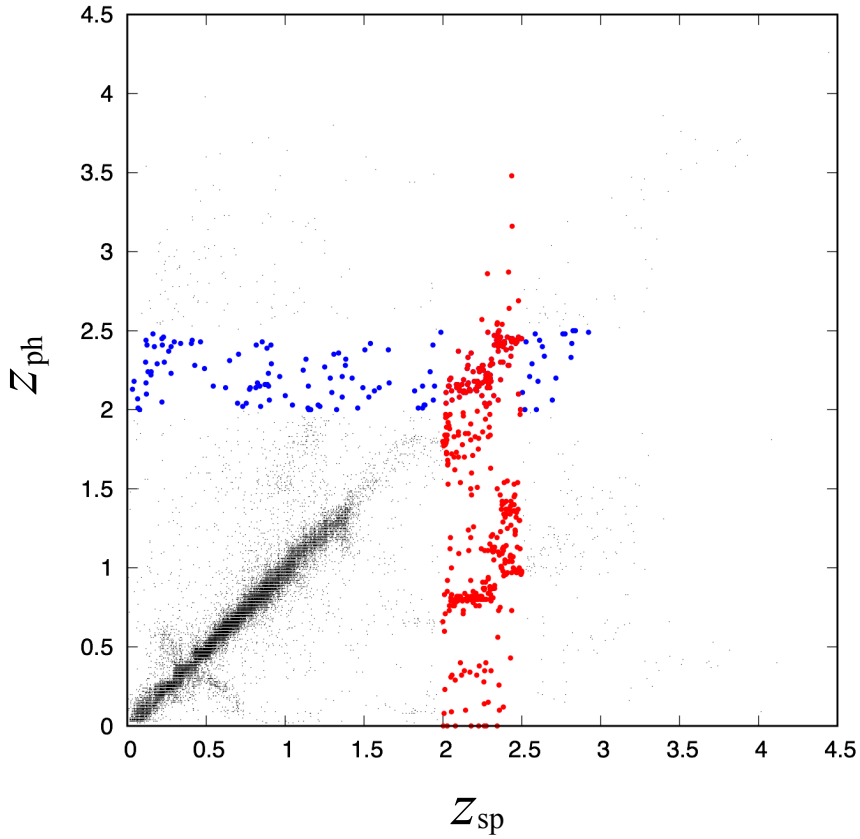

Fig. B.5: The photometric redshift ($z_{\rm ph}$) versus spectroscopic redshift ($z_{\rm sp}$). Red and blue dots show objects with $z_{\rm sp} = 2.0 - 2.5$ and $z_{\rm ph} = 2.0 - 2.5$, respectively.

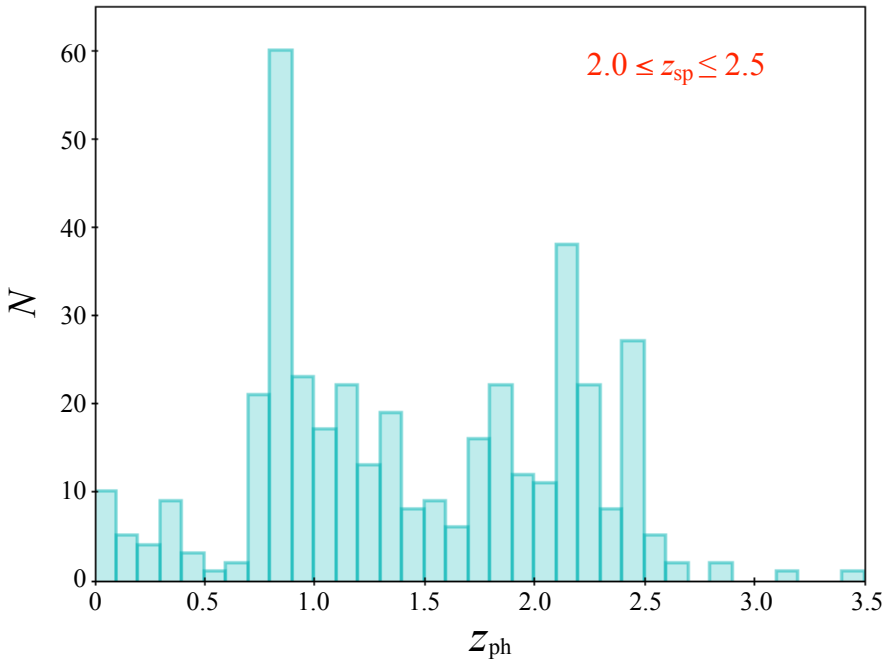

Fig. B.6: The frequency distribution of z_{ph} of objects with $z_{sp} = 2.0 - 2.5$.

such a population since galaxy counterparts of DLAs are thought to be young star-forming galaxies. Indeed, most of high-z DLA counterparts which have been identified so far show the Lyα emission (e.g., Møller et al., 2002, 2004; Fynbo et al., 2010; Noterdaeme et al., 2012b; Krogager et al., 2012; Kashikawa et al., 2014). A possible major contamination is galaxies at $z \sim 0$ because they also show nearly flat SED in the optical wavelength range. On the other hand, as seen in Figure B.7, $z = 0$ galaxies show a slightly redder SED in the longer wavelength range ($\lambda \gtrsim 8000$ Å) compared to the galaxy at $z = 2$. Therefore, to eliminate $z \sim 0$ galaxies, we should utilize photometric bands in a wide optical wavelength range. HSC is useful for this purpose because its broad-band filters cover a wide optical wavelength range from ~4000 Å to ~11000 Å thanks to the high sensitivity even at the longest wavelength range in optical.

Considering the situation described above, we investigate the color of galaxies at various redshifts based on the model SED of the star-forming galaxies, by using the same model as adopted in Figure B.7. Figure B.8 shows the HSC $(g-r)$ versus $(r-y)$ diagram with color tracks of star-forming galaxies (note that passive galaxies are not shown as described above). Star-forming galaxies at $z \sim 2$ are located around zero both in the HSC $(g-r)$ and $(r-y)$ colors, as we expected from their SED. Specifically, galaxies at $1.9 \leq z \leq 3.0$ are distributed at $0 < g-r < 0.1$ and $-0.1 < r-y < 0$. The $(r-y)$ color difference between $z \sim 2$ and $z \sim 1$ galaxies is greater than 0.6 due to Balmer/4000 Å break. Galaxies at $z \sim 0$, that are expected to be the most serious source of the contamination, show similar $(g-r)$ color with $z \sim 2$ galaxies. On the other hand, they show redder $(r-y)$ color (~ 0.2) than galaxies at $z \sim 2$ with the color difference of $\Delta(r-y) \sim 0.3$. Since the typical photometric error in the HSC-SSP Wide field is ~0.06 mag at i ~25.5 (Aihara et al., 2017a), it seems to be possible to distinguish $z \sim 2$ galaxies from $z \sim 0$ galaxies by utilizing the $g-r$ versus $r-y$ diagram.

B.4 Examining the galaxy selection by using a color-color diagram

We further examine the color selection of $z \sim 2$ galaxies with the HSC $(g-r)$ versus $(r-y)$ diagram, by using the photometric redshift sample and spectroscopic sample in the HSC-Deep field. Figure B.9 shows the color-color diagram with the HSC-Deep data of the galaxy sample described in B.3. As seen in this diagram, objects with $2.0 \leq z_{\rm sp} \leq 2.5$ (red dots in Figure B.9) are distributed at a region with $0 \lesssim g-r \lesssim 0.5$ and $0 \lesssim r-y \lesssim 0.8$. Based on this, we determine the selection criteria for selecting most galaxies at $2.0 < z_{\rm sp} < 2.5$ (see Figure B.10). Since our purpose is identifying DLA counterparts, it is important to make the selection completeness as high as possible. Though such a selection results in a somewhat large number of contaminations, it is not a serious problem because we only focus on very narrow regions (~ 100 kpc, corresponding to $\sim 12''$ at $z \sim 2$, from DLAs) around DLAs to search for candidates of counterparts (see Section 2.4.2) and thus the expected number of contaminations in such a narrow region is small. Taking all of the considerations given above into account, we determine the selection criteria for $z \sim 2$ galaxies as follows:

1. $-0.15 \leq g-r \leq 0.50$

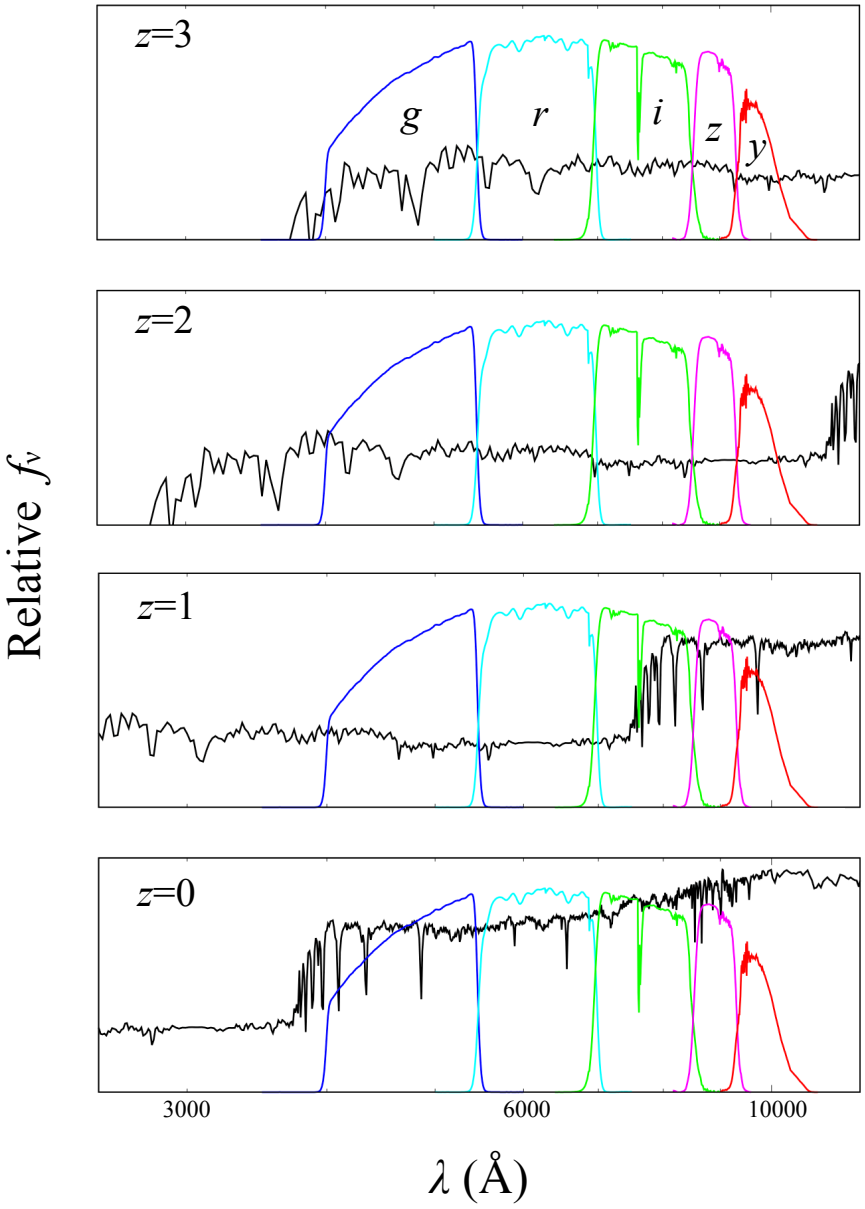

Fig. B.7: Model SEDs of galaxies at various redshifts. The model SED was calculated with the code of Bruzual & Charlot (2003) assuming a constant-SFR model with the Salpeter IMF, $SFR = 1\ \mathrm{M}_\odot\ \mathrm{yr}^{-1}$ and the solar metallicity. Colored lines show the response curves of the HSC filters (g, r, i, z, and y from left to right).

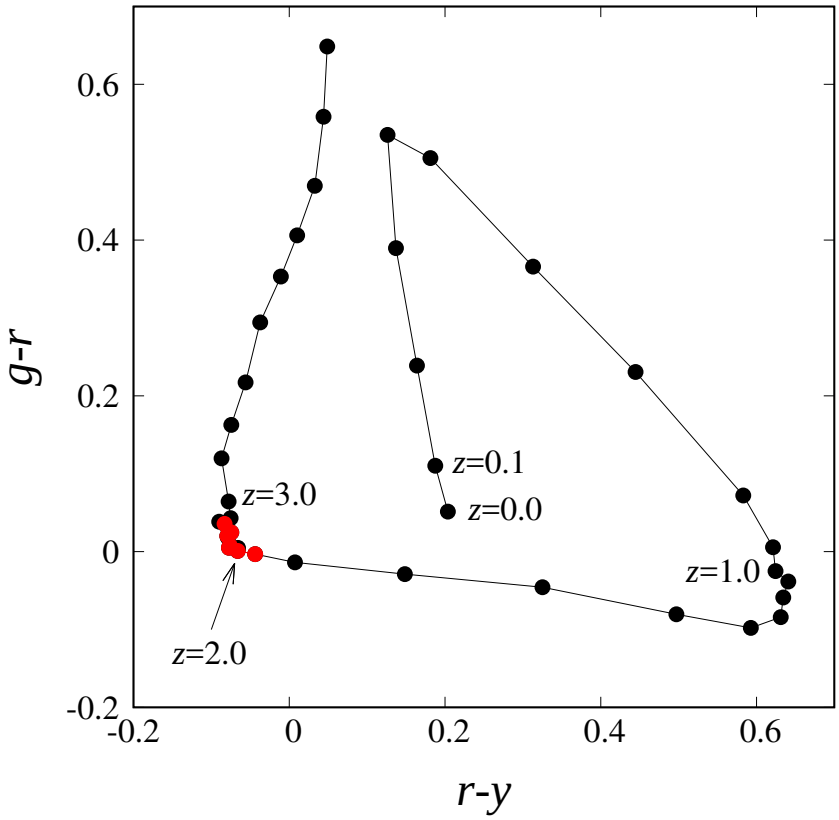

Fig. B.8: The HSC $(g-r)$ versus $(r-y)$ color-color diagram with a color track of star-forming galaxies. Colors are plotted with an interval of $\Delta z = 0.1$ from $z = 0$ to $z = 4.0$. Red filled circles denote star-forming galaxies at $1.9 \leq z \leq 2.5$. Colors are calculated by the same model as Figure B.7.

2. $-0.30 \leq r - y \leq 0.75$

We then apply the defined criteria to the sample of the HSC-SSP galaxies. We summarize the number of galaxies selected through these criteria in Table B.5. Among the total 25,822 objects, 3,197 objects satisfy the selection criteria. Although the fraction of the contamination by low-z ($z_{\rm sp} < 2.0$) objects is still large ($\sim$83%), the contamination is much improved by the selection ($\sim$ 90% of galaxies with $z_{\rm sp} < 2.0$ can be eliminated). Our selection achieves a high completeness of $2.0 \leq z_{\rm sp} \leq 2.5$; more specifically, 347 ($\sim$ 90%) out of 399 objects at $2.0 < z_{\rm sp} \leq 2.5$ are selected. Objects at $2.0 \leq z_{\rm sp} \leq 2.5$ with $2.0 \leq z_{\rm ph} \leq 2.5$, 105 ($\sim$98%) among 107 objects are selected. As for the objects at $2.0 \leq z_{\rm sp} \leq 2.5$ but with $z_{\rm ph} < 2.0$, 233 among 282 objects are selected by our selection criteria. This means that we can recover most part ($\sim$83%) of $2.0 \leq z_{\rm sp} \leq 2.5$ objects that are regarded as lower-z objects in the photometric redshift catalog.

Based on these results, we conclude that the *gry* color selection is powerful and effective to make complete samples of galaxies at $z \sim 2$, that are candidates of DLA counterparts. The selected photometric candidates for DLA counterparts are good targets for follow-up spectroscopic observations.

B.5 The stellar contamination

In addition to lower-z galaxies, early-type stars could also be a possible contamination since they show a flat SED in the optical wavelength, that is similar to star-forming galaxies at $z \sim 2$. In the brighter magnitude range ($i < 24.0$), we can distinguish galaxies from stars by focusing on the morphology of objects (Akiyama et al., 2017). However, in the fainter magnitude range ($i > 24.0$) it is difficult to distinguish extended sources (i.e., galaxies) from stellar objects. Since DLA counterparts are thought to be faint objects, the morphology is not useful for eliminating stellar contamination in our study.

We examine how serious the stellar contamination is, by focusing on the magnitude range of $24.0 \leq i \leq 25.0$, that is the most interesting magnitude range for investigating DLA counterparts. To estimate the number of stars in the HSC-Deep fields, we used a simulation code for estimating the number and photometric properties of Galactic stars as functions of the Galactic coordinate, TRILEGAL (TRIdimensional modeL of thE GALaxy) ver1.6[8] (Girardi et al., 2012). For the sake of simplicity, we examined the central 1 deg^2 region of each HSC-DEEP field. As for the Galactic dust extinction, we adopted the value of A_V estimated by using the extinction map[9] provided by Schlafly & Finkbeiner (2011). We adopted default values in the TRILEGAL for other parameters, such as initial mass function (the Chabrier lognormal IMF), solar position, and the Galactic geometry, that are calibrated by Girardi et al. (2005). Since the TRILEGAL code does not provide the HSC photometric magnitude, we first derived the

[8] `http://stev.oapd.inaf.it/cgi-bin/trilegal`
[9] `http://irsa.ipac.caltech.edu/applications/DUST/`

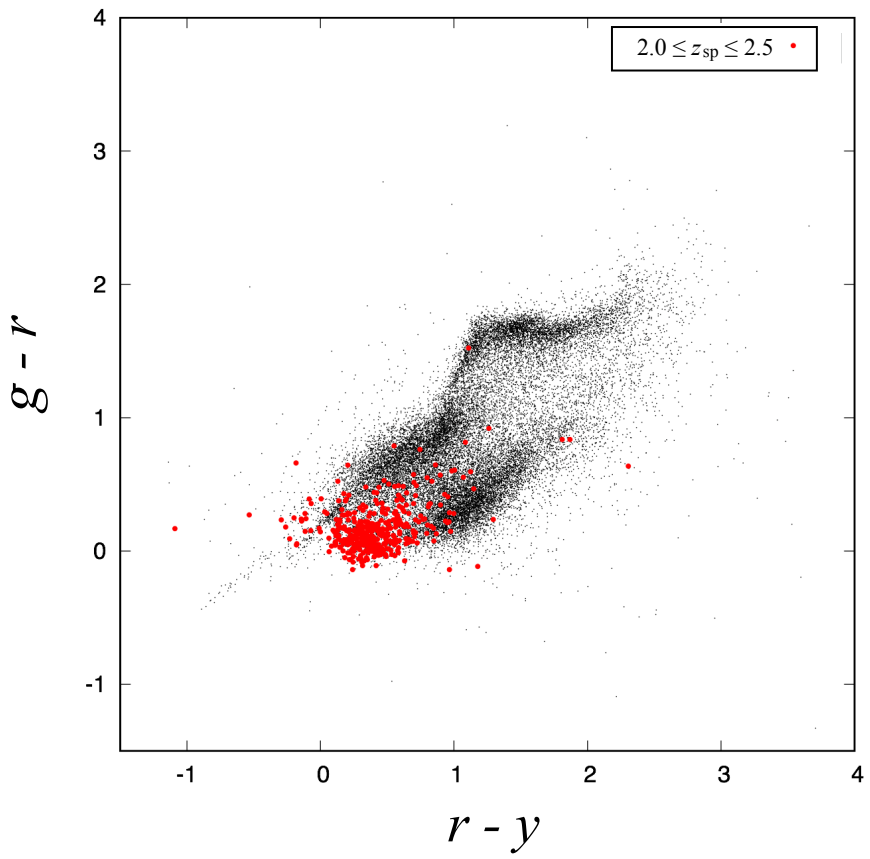

Fig. B.9: The $(g-r)$ vs. $(r-y)$ diagram of the HSC-SSP photometric redshift sample. Red dots show objects with $2.0 \leq z_{\rm sp} \leq 2.5$.

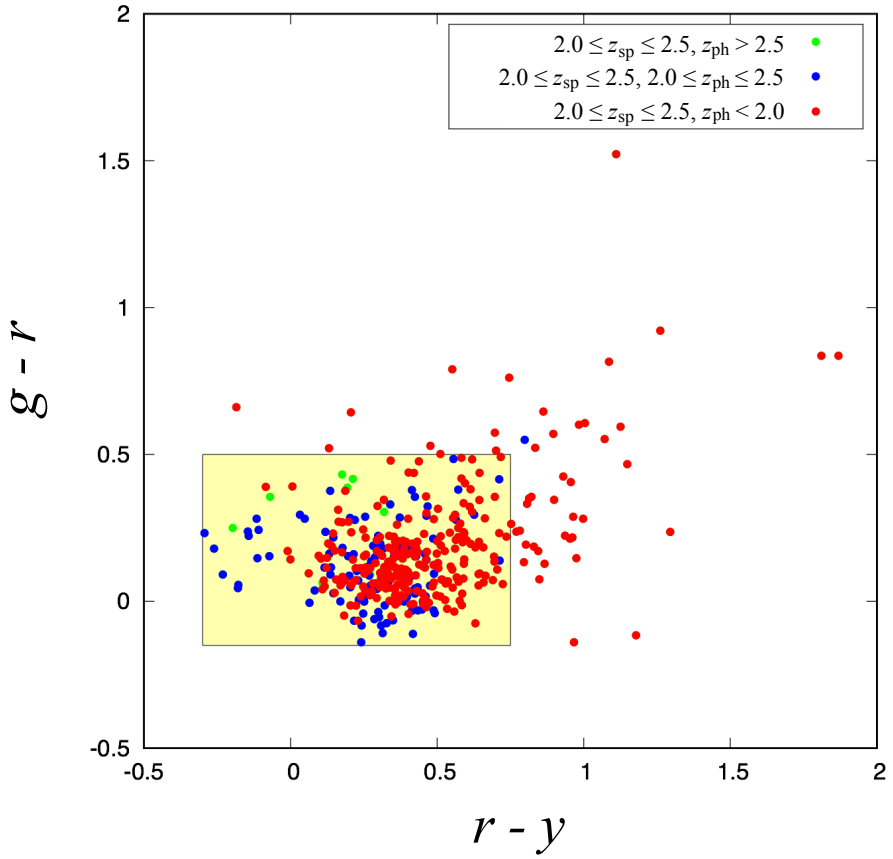

Fig. B.10: The $(g-r)$ vs. $(r-y)$ diagram of the HSC-SSP photometric redshift sample. Same as Figure B.9, red and blue dots show objects with $2.0 \leq z_{ph} \leq 2.5$ and $z_{sp} \leq 1.5$, respectively. The yellow shadowed region indicate the current selection window for $z = 2.0-2.5$ objects.

Table B.5: Number of galaxies selected from the HSC-SSP photo-z sample

z	$N_{\rm obj}$	$N_{\rm selected}$
$z_{\rm sp} < 2.0$	25,126	2,650
$2.0 \leq z_{\rm sp} \leq 2.5$	399	347
$z_{\rm sp} > 2.5$	297	200
Total	25,822	3,197
$2.0 \leq z_{\rm sp} \leq 2.5$ & $2.0 \leq z_{\rm ph} \leq 2.5$	107	105
$2.0 \leq z_{\rm sp} \leq 2.5$ & $z_{\rm ph} < 2.0$	282	233

Notes. $N_{\rm selected}$ is the number of objects satisfying $-0.15 \leq g-r \leq 0.50$ and $-0.30 \leq r-y \leq 0.75$, while $N_{\rm obj}$ is the number of HSC-SSP objects in each redshift range before adopting the color selections.

Pan-STARRS photometry and then converted them to HSC magnitudes by using the color-term provided in the HSC-SSP data release page[10].

Figures B.11 to B.14 show the $(g-r)$ versus $(r-y)$ diagrams in each HSC-Deep field with the simulated stars calculated with TRILEGAL down to $m_{AB} = 26$. Although there are many stars in the selection window for $z \sim 2$, most of them are brighter than $i = 24.0$ which can be distinguished from galaxies by their morphology. Table B.6 summarizes the results of the TRILEGAL simulation for the stellar contamination. Numbers of stars with $24.0 \leq i \leq 25.0$ satisfying the selection criteria for $z \sim 2$ galaxies are less than $\sim$50 (deg^{-2}) in each field. Based on the LF of star-forming galaxies reported by Oesch et al. (2010), the expected number of $2.0 \leq z <\leq 2.5$ galaxies with $24.0 \leq i \leq 25.0$ in the HSC-Deep field is $\sim$1,000 per deg^2, significantly greater than the expected number of contaminating stars in the same magnitude range. Therefore, we conclude that the stellar contamination is negligible.

B.6 Conclusion

To search for galaxy counterparts of high-z DLAs based on wide-field optical photometric surveys, we study selection methods for $z \sim 2$ galaxies with the HSC-SSP optical photometric data. We summarize the results of this study as follows.

1. Among various wide-field surveys, we focus on the HSC-SSP wide-layer survey because of the depth ($r \sim 26.1$, 5σ limit) and the wideness ($\sim$1400 deg^{-2}) of this survey.

2. There are 3,577 BOSS DLAs in the HSC-SSP survey fields and their redshift distribution peaks at $z \sim 2-2.5$. Since the cosmic SFRD also peaks at similar redshift, it is interesting to investigate the galaxy counterpart of DLAs at $z \sim 2$ for understanding the early phase of galaxy evolution.

3. Although the photometric redshift is potentially useful to investigate candidates of DLA counterparts, significant fraction of $z \sim 2$ galaxies are misclassified as lower-z objects in the photometric redshift.

4. We investigate the color track of galaxies at various redshifts and find that the $(g-r)$ versus $(r-y)$ color-color diagram is useful to select galaxies at $z \sim 2$ more completely than photometric redshift techniques.

5. By utilizing the $(g-r)$ versus $(r-y)$ diagram, we can select most of $z \sim 2$ objects that are missed by photometric redshift.

6. We estimate the number of early-type stars that are a possible contamination for star-forming galaxies at $z \sim 2$, and find that the stellar contamination is negligible.

[10] `https://hsc-release.mtk.nao.ac.jp/doc/index.php/data/#color-terms`

Table B.6: Number of stars in each HSC-Deep field estimated by TRILEGAL

Field	$N_{\rm obj}$ (deg^{-2})	$N_{\rm selected}$ (deg^{-2})	$N_{\rm sel,24<i<25}$ (deg^{-2})
XMM-LSS	8,316	612	25
E-COSMOS	13,198	1,029	44
ELAIS-N1	17,641	1,304	54
Deep2-3	12,927	919	33

Notes. $N_{\rm obj}$ is the number of simulated stars per 1 deg^2 in each HSC-Deep field before adopting the color selections. $N_{\rm selected}$ is the number of simulated stars satisfying $-0.15 \leq g-r \leq 0.50$ and $-0.30 \leq r-y \leq 0.75$, while $N_{\rm sel,24<i<25}$ is that of simulated stars selected by the photometric criteria in the magnitude range of $24.0 \leq i \leq 25.0$.

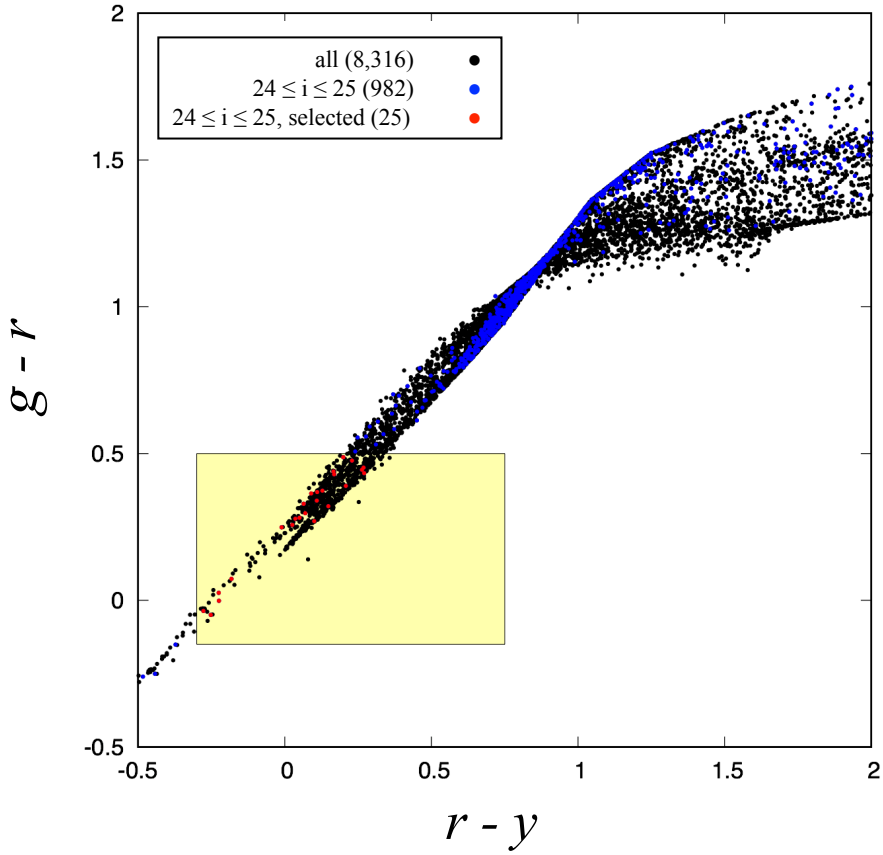

Fig. B.11: The $(g-r)$ vs. $(r-y)$ diagram of stars in the XMM-LSS field, simulated by TRILEGAL. Black, blue, and red dots show all stars, stars with $24.0 \leq i \leq 25.0$, and stars with $24.0 \leq i \leq 25.0$ satisfying the selection criteria for $z \sim 2$ galaxies. Yellow shadowed box shows the selection window for $z \sim 2$ galaxies.

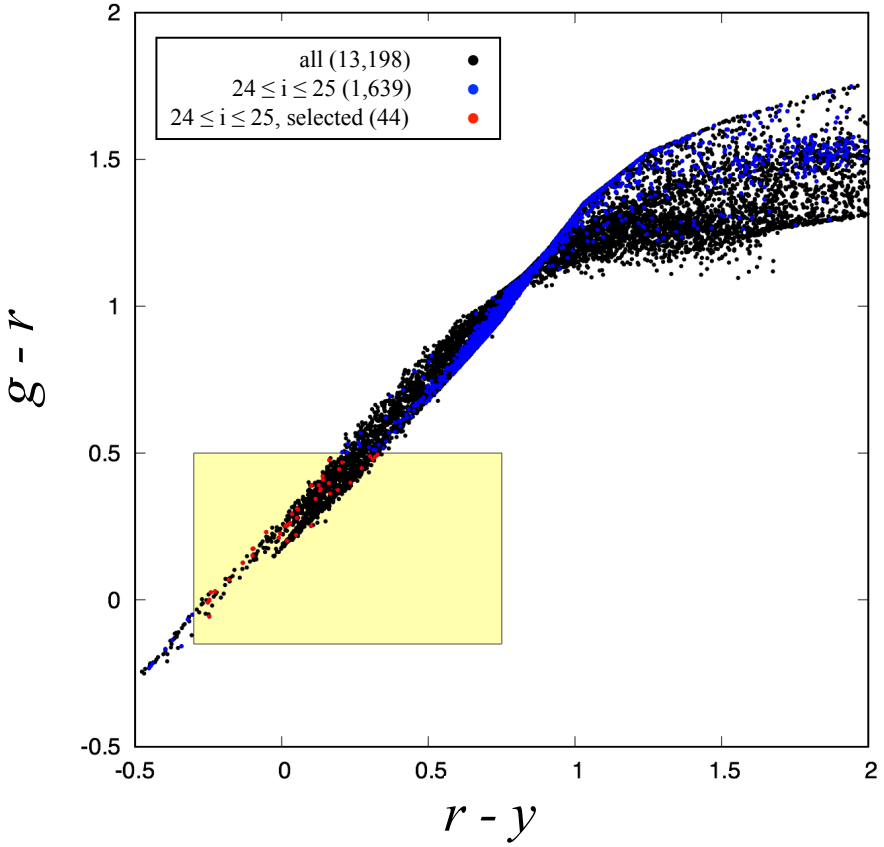

Fig. B.12: The $(g-r)$ vs. $(r-y)$ diagram of stars in the E-COSMOS field, simulated by TRILEGAL. Black, blue, and red dots show all stars, stars with $24.0 \leq i \leq 25.0$, and stars with $24.0 \leq i \leq 25.0$ satisfying the selection criteria for $z \sim 2$ galaxies. Yellow shadowed box shows the selection window for $z \sim 2$ galaxies.

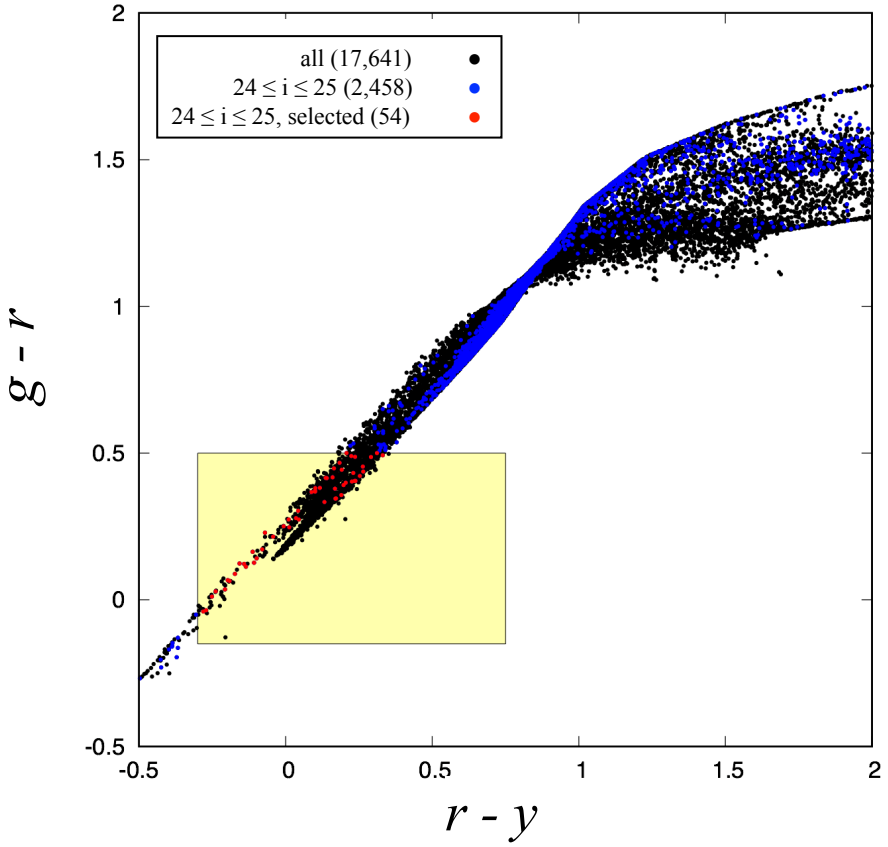

Fig. B.13: The $(g-r)$ vs. $(r-y)$ diagram of stars in the ELAIS-N1 field, simulated by TRILEGAL. Black, blue, and red dots show all stars, stars with $24.0 \leq i \leq 25.0$, and stars with $24.0 \leq i \leq 25.0$ satisfying the selection criteria for $z \sim 2$ galaxies. Yellow shadowed box shows the selection window for $z \sim 2$ galaxies.

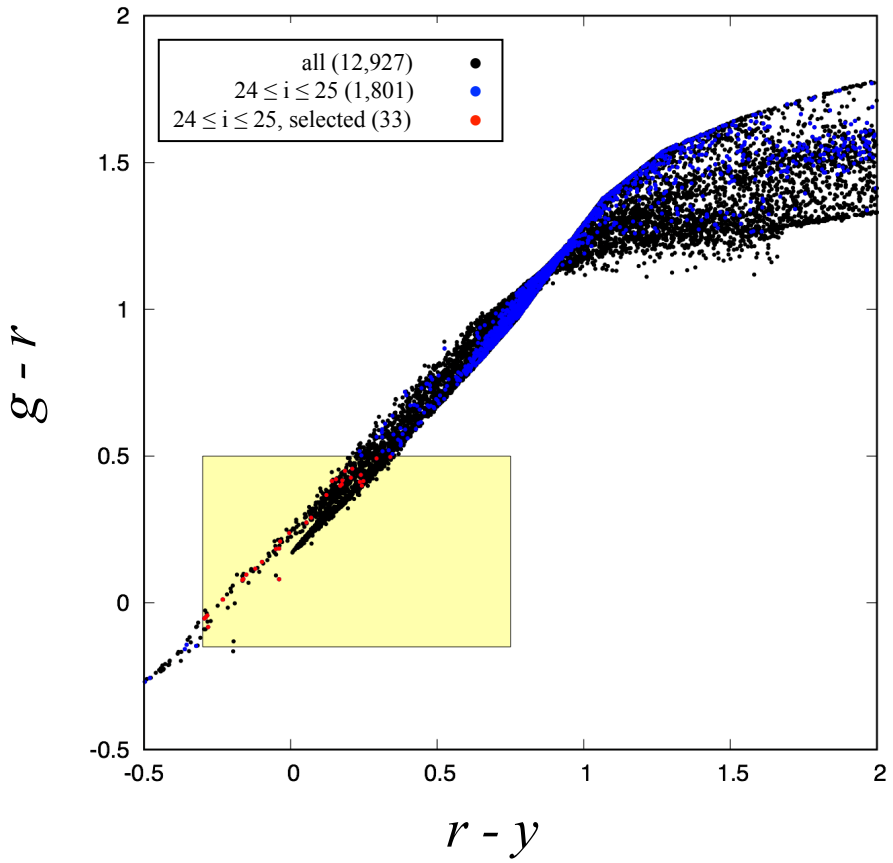

Fig. B.14: The $(g-r)$ vs. $(r-y)$ diagram of stars in the Deep2-3 field, simulated by TRILEGAL. Black, blue, and red dots show all stars, stars with $24.0 \leq i \leq 25.0$, and stars with $24.0 \leq i \leq 25.0$ satisfying selection the criteria for $z \sim 2$ galaxies. Yellow shadowed box shows the selection window for $z \sim 2$ galaxies.

Even though the contamination rate is still high after adopting the color selection, it is important not to miss objects at target redshift for identifying DLA counterparts. Because spectroscopic follow-up observations are required to confirm DLA counterparts in any case, the purpose of photometric surveys is to narrow down "candidates" of counterparts. In this context, our selection method will improve the efficiency of explorations for DLA counterparts. Based on the HSC-SSP dataset, we will construct a large sample of DLA counterpart candidates. The candidates should be confirmed as actual counterparts by spectroscopic follow-up observations with coming 30 m class telescopes, such as Thirty Meter Telescope (TMT), European Extremely Large Telescope (EELT), and Giant Magellan Telescope (GMT). Furthermore, as we described above, since the SFRD peaks at $z \sim 2$ and this redshift is interesting to investigate the galaxy evolution, our selection method is useful in various science as well as explorations for DLA counterparts.

BIBLIOGRAPHY

Adams, S. M., Martini, P., Croxall, K. V., Overzier, R. A., & Silverman, J. D. 2015, MNRAS, 448, 1335

Adelberger, K. L., Steidel, C. C., Pettini, M., et al. 2005, ApJ, 619, 697

Ahn, C. P., Alexandroff, R., Allende Prieto, C., et al. 2012, ApJS, 203, 21

Aihara, H., Armstrong, R., Bickerton, S., et al. 2017a, ArXiv e-prints, arXiv:1702.08449

Aihara, H., Arimoto, N., Armstrong, R., et al. 2017b, ArXiv e-prints, arXiv:1704.05858

Ajiki, M., Taniguchi, Y., Fujita, S. S., et al. 2003, AJ, 126, 2091

Akiyama, M., He, W., Ikeda, H., et al. 2017, ArXiv e-prints, arXiv:1704.05996

Alam, S., Albareti, F. D., Allende Prieto, C., et al. 2015, ApJS, 219, 12

Amara, A., Lilly, S., Kovač, K., et al. 2012, MNRAS, 424, 553

Arnaboldi, M., Neeser, M. J., Parker, L. C., et al. 2007, The Messenger, 127

Bañados, E., Venemans, B., Walter, F., et al. 2013, ApJ, 773, 178

Balogh, M. L., Schade, D., Morris, S. L., et al. 1998, ApJ, 504, L75

Barkana, R., & Loeb, A. 1999, ApJ, 523, 54

Battisti, A. J., Meiring, J. D., Tripp, T. M., et al. 2012, ApJ, 744, 93

Bernstein, G., & Huterer, D. 2010, MNRAS, 401, 1399

Bertin, E., & Arnouts, S. 1996, A&AS, 117, 393

Beutler, F., Blake, C., Colless, M., et al. 2013, MNRAS, 429, 3604

Bolatto, A. D., Wolfire, M., & Leroy, A. K. 2013, ARA&A, 51, 207

Bouché, N., Murphy, M. T., Kacprzak, G. G., et al. 2013, Science, 341, 50

Bouwens, R. J., Illingworth, G. D., Oesch, P. A., et al. 2011, ApJ, 737, 90

—. 2015, ApJ, 803, 34

Boylan-Kolchin, M., Springel, V., White, S. D. M., Jenkins, A., & Lemson, G. 2009, MNRAS, 398, 1150

Bradshaw, E. J., Almaini, O., Hartley, W. G., et al. 2013, MNRAS, 433, 194

Brodwin, M., Stanford, S. A., Gonzalez, A. H., et al. 2013, ApJ, 779, 138

Bruzual, G., & Charlot, S. 2003, MNRAS, 344, 1000

Butcher, H., & Oemler, Jr., A. 1984, ApJ, 285, 426

Carilli, C. L., & Walter, F. 2013, ARA&A, 51, 105

Chambers, K. C., Magnier, E. A., Metcalfe, N., et al. 2016, ArXiv e-prints, arXiv:1612.05560

Chiang, Y.-K., Overzier, R., & Gebhardt, K. 2013, ApJ, 779, 127

Churchill, C. W., Mellon, R. R., Charlton, J. C., et al. 2000, ApJ, 543, 577

Ciardullo, R., Gronwall, C., Wolf, C., et al. 2012, ApJ, 744, 110

Ciardullo, R., Gronwall, C., Adams, J. J., et al. 2013, ApJ, 769, 83

Coil, A. L., Blanton, M. R., Burles, S. M., et al. 2011, ApJ, 741, 8

Cooke, J., & O'Meara, J. M. 2015, ApJ, 812, L27

Cool, R. J., Moustakas, J., Blanton, M. R., et al. 2013, ApJ, 767, 118

Cowie, L. L., Barger, A. J., & Hu, E. M. 2010, ApJ, 711, 928

—. 2011, ApJ, 738, 136

Cowie, L. L., & Hu, E. M. 1998, AJ, 115, 1319

Daddi, E., Cimatti, A., Renzini, A., et al. 2004, ApJ, 617, 746

Daddi, E., Bournaud, F., Walter, F., et al. 2010, ApJ, 713, 686

Davis, M., Faber, S. M., Newman, J., et al. 2003, in Proc. SPIE, Vol. 4834, Discoveries and Research Prospects from 6- to 10-Meter-Class Telescopes II, ed. P. Guhathakurta, 161–172

Dawson, K. S., Schlegel, D. J., Ahn, C. P., et al. 2013, AJ, 145, 10

Dawson, K. S., Kneib, J.-P., Percival, W. J., et al. 2016, AJ, 151, 44

de Jong, J. T. A., Kuijken, K., Applegate, D., et al. 2013, The Messenger, 154, 44

de Lapparent, V., Geller, M. J., & Huchra, J. P. 1986, ApJ, 302, L1

Djorgovski, S. G., Pahre, M. A., Bechtold, J., & Elston, R. 1996, Nature, 382, 234

Dressler, A. 1980, ApJ, 236, 351

Drinkwater, M. J., Jurek, R. J., Blake, C., et al. 2010, MNRAS, 401, 1429

Eisenstein, D. J., Zehavi, I., Hogg, D. W., et al. 2005, ApJ, 633, 560

Eisenstein, D. J., Weinberg, D. H., Agol, E., et al. 2011, AJ, 142, 72

Flaugher, B. 2005, International Journal of Modern Physics A, 20, 3121

Flaugher, B., Diehl, H. T., Honscheid, K., et al. 2015, AJ, 150, 150

Franck, J. R., & McGaugh, S. S. 2016a, ApJ, 833, 15

—. 2016b, ApJ, 817, 158

Frenk, C. S., & White, S. D. M. 2012, Annalen der Physik, 524, 507

Fumagalli, M., O'Meara, J. M., Prochaska, J. X., & Kanekar, N. 2010, MNRAS, 408, 362

Fynbo, J. P. U., Krogager, J.-K., Venemans, B., et al. 2013, ApJS, 204, 6

Fynbo, J. P. U., Laursen, P., Ledoux, C., et al. 2010, MNRAS, 408, 2128

Fynbo, J. P. U., Ledoux, C., Noterdaeme, P., et al. 2011, MNRAS, 413, 2481

Gao, L., White, S. D. M., Jenkins, A., Frenk, C. S., & Springel, V. 2005, MNRAS, 363, 379

Garilli, B., Guzzo, L., Scodeggio, M., et al. 2014, A&A, 562, A23

Garn, T., & Best, P. N. 2010, MNRAS, 409, 421

Gawiser, E., van Dokkum, P. G., Gronwall, C., et al. 2006, ApJ, 642, L13

Gawiser, E., Francke, H., Lai, K., et al. 2007, ApJ, 671, 278

Geach, J. E., Smail, I., Moran, S. M., et al. 2011, ApJ, 730, L19

Giavalisco, M., Dickinson, M., Ferguson, H. C., et al. 2004, ApJ, 600, L103

Girardi, L., Groenewegen, M. A. T., Hatziminaoglou, E., & da Costa, L. 2005, A&A, 436, 895

Girardi, L., Barbieri, M., Groenewegen, M. A. T., et al. 2012, Astrophysics and Space Science Proceedings, 26, 165

Gronwall, C., Ciardullo, R., Hickey, T., et al. 2007, ApJ, 667, 79

Gwyn, S. D. J. 2012, AJ, 143, 38

Haehnelt, M. G., Steinmetz, M., & Rauch, M. 1998, ApJ, 495, 647

Hawkins, E., Maddox, S., Cole, S., et al. 2003, MNRAS, 346, 78

Hayashino, T., Matsuda, Y., Tamura, H., et al. 2004, AJ, 128, 2073

Hayes, M. 2015, PASA, 32, e027

Hayes, M., Östlin, G., Schaerer, D., et al. 2010, Nature, 464, 562

Hayes, M., Östlin, G., Duval, F., et al. 2014, ApJ, 782, 6

Hennawi, J. F., Prochaska, J. X., Cantalupo, S., & Arrigoni-Battaia, F. 2015, Science, 348, 779

Hjorth, J., Møller, P., Gorosabel, J., et al. 2003, ApJ, 597, 699

Hopkins, A. M., & Beacom, J. F. 2006, ApJ, 651, 142

Hu, E. M., Cowie, L. L., Barger, A. J., et al. 2010, ApJ, 725, 394

Hu, E. M., Cowie, L. L., Capak, P., et al. 2004, AJ, 127, 563

Ichikawa, T., Suzuki, R., Tokoku, C., et al. 2006, in Proc. SPIE, Vol. 6269, Society of Photo-Optical Instrumentation Engineers (SPIE) Conference Series, 626916

Ilbert, O., Arnouts, S., McCracken, H. J., et al. 2006, A&A, 457, 841

Im, M., Griffiths, R. E., & Ratnatunga, K. U. 1997, ApJ, 475, 457

Impey, C., & Bothun, G. 1989, ApJ, 341, 89

Ishiyama, T., Enoki, M., Kobayashi, M. A. R., et al. 2015, PASJ, 67, 61

Ivezic, Z., Tyson, J. A., Abel, B., et al. 2008, ArXiv e-prints, arXiv:0805.2366

Iwata, I., Inoue, A. K., Matsuda, Y., et al. 2009, ApJ, 692, 1287

Jakobsson, P., Hjorth, J., Fynbo, J. P. U., et al. 2004, A&A, 427, 785

Jensen, B. L., Fynbo, J. U., Gorosabel, J., et al. 2001, A&A, 370, 909

Jimenez, R., Bowen, D. V., & Matteucci, F. 1999, ApJ, 514, L83

Jimenez, R., Padoan, P., Matteucci, F., & Heavens, A. F. 1998, MNRAS, 299, 123

Kacprzak, G. G., Murphy, M. T., & Churchill, C. W. 2010, MNRAS, 406, 445

Kashikawa, N., Kitayama, T., Doi, M., et al. 2007, ApJ, 663, 765

Kashikawa, N., Misawa, T., Minowa, Y., et al. 2014, ApJ, 780, 116

Kashikawa, N., Inata, M., Iye, M., et al. 2000, in Proc. SPIE, Vol. 4008, Optical and IR Telescope Instrumentation and Detectors, ed. M. Iye & A. F. Moorwood, 104–113

Kashikawa, N., Shimasaku, K., Malkan, M. A., et al. 2006, ApJ, 648, 7

Kashikawa, N., Shimasaku, K., Matsuda, Y., et al. 2011, ApJ, 734, 119

Kauffmann, G., White, S. D. M., Heckman, T. M., et al. 2004, MNRAS, 353, 713

Kennicutt, R. C., & Evans, N. J. 2012, ARA&A, 50, 531

Kennicutt, Jr., R. C. 1998, ARA&A, 36, 189

Konno, A., Ouchi, M., Nakajima, K., et al. 2016, ApJ, 823, 20

Konno, A., Ouchi, M., Ono, Y., et al. 2014, ApJ, 797, 16

Krogager, J.-K., Fynbo, J. P. U., Møller, P., et al. 2012, MNRAS, 424, L1

Krogager, J.-K., Fynbo, J. P. U., Ledoux, C., et al. 2013, MNRAS, 433, 3091

Kuiper, E., Hatch, N. A., Venemans, B. P., et al. 2011, MNRAS, 417, 1088

Kurk, J. D., Röttgering, H. J. A., Pentericci, L., et al. 2000, A&A, 358, L1

Lanfranchi, G. A., & Friaça, A. C. S. 2003, MNRAS, 343, 481

Lawrence, A., Warren, S. J., Almaini, O., et al. 2007, MNRAS, 379, 1599

Le Fèvre, O., Cassata, P., Cucciati, O., et al. 2013, A&A, 559, A14

Lee, K.-S., Dey, A., Hong, S., et al. 2014, ApJ, 796, 126

Lemaux, B. C., Lubin, L. M., Sawicki, M., et al. 2009, ApJ, 700, 20

Lemaux, B. C., Le Fèvre, O., Cucciati, O., et al. 2017, ArXiv e-prints, arXiv:1703.10170

Lilly, S. J., Le Brun, V., Maier, C., et al. 2009, ApJS, 184, 218

Liske, J., Baldry, I. K., Driver, S. P., et al. 2015, MNRAS, 452, 2087

Madau, P., & Dickinson, M. 2014, ARA&A, 52, 415

Madau, P., Ferguson, H. C., Dickinson, M. E., et al. 1996, MNRAS, 283, 1388

Magdis, G. E., Daddi, E., Sargent, M., et al. 2012, ApJ, 758, L9

Magnelli, B., Saintonge, A., Lutz, D., et al. 2012, A&A, 548, A22

Malhotra, S., & Rhoads, J. E. 2002, ApJ, 565, L71

—. 2004, ApJ, 617, L5

Massey, R., Rhodes, J., Ellis, R., et al. 2007, Nature, 445, 286

Matteucci, F., Molaro, P., & Vladilo, G. 1997, A&A, 321, 45

Matthee, J., Sobral, D., Santos, S., et al. 2015, MNRAS, 451, 400

Mawatari, K., Inoue, A. K., Kousai, K., et al. 2016, ApJ, 817, 161

Mawatari, K., Yamada, T., Nakamura, Y., Hayashino, T., & Matsuda, Y. 2012, ApJ, 759, 133

Mazzucchelli, C., Bañados, E., Decarli, R., et al. 2017, ApJ, 834, 83

McLure, R. J., Pearce, H. J., Dunlop, J. S., et al. 2013, MNRAS, 428, 1088

Mihalas, D. 1978, Stellar atmospheres /2nd edition/

Miley, G. K., Overzier, R. A., Tsvetanov, Z. I., et al. 2004, Nature, 427, 47

Mink, D. J. 2002, in Astronomical Society of the Pacific Conference Series, Vol. 281, Astronomical Data Analysis Software and Systems XI, ed. D. A. Bohlender, D. Durand, & T. H. Handley, 169

Miyazaki, S., Komiyama, Y., Sekiguchi, M., et al. 2002, PASJ, 54, 833

Miyazaki, S., Komiyama, Y., Nakaya, H., et al. 2012, in Proc. SPIE, Vol. 8446, Ground-based and Airborne Instrumentation for Astronomy IV, 84460Z

Møller, P., Fynbo, J. P. U., & Fall, S. M. 2004, A&A, 422, L33

Møller, P., Fynbo, J. P. U., Hjorth, J., et al. 2002, A&A, 396, L21

Momcheva, I. G., Brammer, G. B., van Dokkum, P. G., et al. 2016, ApJS, 225, 27

Monet, D. G., Levine, S. E., Canzian, B., et al. 2003, AJ, 125, 984

Muldrew, S. I., Hatch, N. A., & Cooke, E. A. 2015, MNRAS, 452, 2528

Nagao, T., Murayama, T., Maiolino, R., et al. 2007, A&A, 468, 877

Nakajima, K., Ouchi, M., Shimasaku, K., et al. 2012, ApJ, 745, 12

Natarajan, P., Chadayammuri, U., Jauzac, M., et al. 2017, MNRAS, 468, 1962

Neeleman, M., Kanekar, N., Prochaska, J. X., et al. 2017, Science, 355, 1285

Newman, J. A., Cooper, M. C., Davis, M., et al. 2013, ApJS, 208, 5

Nilsson, K. K., Orsi, A., Lacey, C. G., Baugh, C. M., & Thommes, E. 2007, A&A, 474, 385

Nilsson, K. K., Tapken, C., Møller, P., et al. 2009, A&A, 498, 13

Noterdaeme, P., Petitjean, P., Ledoux, C., & Srianand, R. 2009, A&A, 505, 1087

Noterdaeme, P., Petitjean, P., Carithers, W. C., et al. 2012a, A&A, 547, L1

Noterdaeme, P., Laursen, P., Petitjean, P., et al. 2012b, A&A, 540, A63

Oesch, P. A., Bouwens, R. J., Carollo, C. M., et al. 2010, ApJ, 725, L150

Ogura, K., Nagao, T., Imanishi, M., et al. 2017, PASJ, 69, 51

O'Meara, J. M., Prochaska, J. X., Burles, S., et al. 2007, ApJ, 656, 666

Ono, Y., Ouchi, M., Shimasaku, K., et al. 2010a, ApJ, 724, 1524

—. 2010b, MNRAS, 402, 1580

Ono, Y., Ouchi, M., Mobasher, B., et al. 2012, ApJ, 744, 83

Onoue, M., Kashikawa, N., Uchiyama, H., et al. 2017, ArXiv e-prints, arXiv:1704.06051

Ostriker, J. P., & Steinhardt, P. J. 1995, Nature, 377, 600

Ouchi, M., Shimasaku, K., Furusawa, H., et al. 2003, ApJ, 582, 60

Ouchi, M., Shimasaku, K., Okamura, S., et al. 2004, ApJ, 611, 660

Ouchi, M., Hamana, T., Shimasaku, K., et al. 2005, ApJ, 635, L117

Ouchi, M., Shimasaku, K., Akiyama, M., et al. 2008, ApJS, 176, 301

Ouchi, M., Shimasaku, K., Furusawa, H., et al. 2010, ApJ, 723, 869

Overzier, R. A. 2016, A&ARv, 24, 14

Overzier, R. A., Miley, G. K., Bouwens, R. J., et al. 2006, ApJ, 637, 58

Pâris, I., Petitjean, P., Aubourg, É., et al. 2012, A&A, 548, A66

Peebles, P. J. E. 1980, in Annals of the New York Academy of Sciences, Vol. 336, Ninth Texas Symposium on Relativistic Astrophysics, ed. J. Ehlers, J. J. Perry, & M. Walker, 161–171

Perlmutter, S., Aldering, G., Goldhaber, G., et al. 1999, ApJ, 517, 565

Péroux, C., Bouché, N., Kulkarni, V. P., York, D. G., & Vladilo, G. 2011, MNRAS, 410, 2237

—. 2012, MNRAS, 419, 3060

Péroux, C., McMahon, R. G., Storrie-Lombardi, L. J., & Irwin, M. J. 2003, MNRAS, 346, 1103

Pettini, M., Ellison, S. L., Steidel, C. C., & Bowen, D. V. 1999, ApJ, 510, 576

Popesso, P., Rodighiero, G., Saintonge, A., et al. 2011, A&A, 532, A145

Popping, G., Caputi, K. I., Somerville, R. S., & Trager, S. C. 2012, MNRAS, 425, 2386

Popping, G., Caputi, K. I., Trager, S. C., et al. 2015, MNRAS, 454, 2258

Prescott, M. K. M., Kashikawa, N., Dey, A., & Matsuda, Y. 2008, ApJ, 678, L77

Prochaska, J. X., Hennawi, J. F., & Herbert-Fort, S. 2008, ApJ, 675, 1002

Prochaska, J. X., & Wolfe, A. M. 1996, ApJ, 470, 403

—. 1997, ApJ, 487, 73

—. 1998, ApJ, 507, 113

Rao, S. M., Belfort-Mihalyi, M., Turnshek, D. A., et al. 2011, MNRAS, 416, 1215

Rao, S. M., & Turnshek, D. A. 2000, ApJS, 130, 1

Rao, S. M., Turnshek, D. A., & Briggs, F. H. 1995, ApJ, 449, 488

Rao, S. M., Turnshek, D. A., & Nestor, D. B. 2006, ApJ, 636, 610

Rhoads, J. E., & Malhotra, S. 2001, ApJ, 563, L5

Rhoads, J. E., Malhotra, S., Dey, A., et al. 2000, ApJ, 545, L85

Riechers, D. A., Carilli, C. L., Walter, F., & Momjian, E. 2010, ApJ, 724, L153

Schechter, P. 1976, ApJ, 203, 297

Schlafly, E. F., & Finkbeiner, D. P. 2011, ApJ, 737, 103

Schmidt, B. P., Suntzeff, N. B., Phillips, M. M., et al. 1998, ApJ, 507, 46

Shibuya, T., Ouchi, M., Konno, A., et al. 2017, ArXiv e-prints, arXiv:1704.08140

Shimakawa, R., Kodama, T., Hayashi, M., et al. 2017a, MNRAS, 468, L21

Shimakawa, R., Kodama, T., Shibuya, T., et al. 2017b, MNRAS, 468, 1123

Shimasaku, K., Ouchi, M., Okamura, S., et al. 2003, ApJ, 586, L111

Shioya, Y., Taniguchi, Y., Sasaki, S. S., et al. 2008, ApJS, 175, 128

Silverman, J. D., Kashino, D., Sanders, D., et al. 2015, ApJS, 220, 12

Simon, P., Taylor, A. N., & Hartlap, J. 2009, MNRAS, 399, 48

Skelton, R. E., Whitaker, K. E., Momcheva, I. G., et al. 2014, ApJS, 214, 24

Sołtan, A. M., & Chodorowski, M. J. 2015, MNRAS, 453, 1013

Sommer-Larsen, J., & Fynbo, J. P. U. 2017, MNRAS, 464, 2441

Springel, V. 2005, MNRAS, 364, 1105

Springel, V., Frenk, C. S., & White, S. D. M. 2006, Nature, 440, 1137

Springel, V., White, S. D. M., Jenkins, A., et al. 2005, Nature, 435, 629

Srianand, R., Hussain, T., Noterdaeme, P., et al. 2016, MNRAS, 460, 634

Steidel, C. C., Adelberger, K. L., Dickinson, M., et al. 1998, ApJ, 492, 428

Steidel, C. C., Adelberger, K. L., Shapley, A. E., et al. 2003, ApJ, 592, 728

Steidel, C. C., & Hamilton, D. 1992, AJ, 104, 941

Steidel, C. C., Pettini, M., & Hamilton, D. 1995, AJ, 110, 2519

Steidel, C. C., Shapley, A. E., Pettini, M., et al. 2004, ApJ, 604, 534

Storrie-Lombardi, L. J., & Wolfe, A. M. 2000, ApJ, 543, 552

Straka, L. A., Johnson, S., York, D. G., et al. 2016, MNRAS, 458, 3760

Suzuki, R., Tokoku, C., Ichikawa, T., et al. 2008, PASJ, 60, 1347

Tacconi, L. J., Genzel, R., Neri, R., et al. 2010, Nature, 463, 781

Takada, M., Ellis, R. S., Chiba, M., et al. 2014, PASJ, 66, R1

Tanaka, M. 2015, ApJ, 801, 20

Tanaka, M., Coupon, J., Hsieh, B.-C., et al. 2017, ArXiv e-prints, arXiv:1704.05988

Taniguchi, Y., & Shioya, Y. 2000, ApJ, 532, L13

—. 2001, ApJ, 547, 146

Taniguchi, Y., Ajiki, M., Nagao, T., et al. 2005, PASJ, 57, 165

Taniguchi, Y., Kajisawa, M., Kobayashi, M. A. R., et al. 2015, ApJ, 809, L7

Toshikawa, J., Kashikawa, N., Ota, K., et al. 2012, ApJ, 750, 137

Toshikawa, J., Kashikawa, N., Overzier, R., et al. 2016, ApJ, 826, 114

Totsuji, H., & Kihara, T. 1969, PASJ, 21, 221

Toy, V. L., Cucchiara, A., Veilleux, S., et al. 2016, ApJ, 832, 175

Tran, K.-V. H., Papovich, C., Saintonge, A., et al. 2010, ApJ, 719, L126

Troncoso, P., Maiolino, R., Sommariva, V., et al. 2014, A&A, 563, A58

Turnshek, D. A., Monier, E. M., Rao, S. M., et al. 2015, MNRAS, 449, 1536

Uchiyama, H., Toshikawa, J., Kashikawa, N., et al. 2017, ArXiv e-prints, arXiv:1704.06050

Utsumi, Y., Goto, T., Kashikawa, N., et al. 2010, ApJ, 721, 1680

van Dokkum, P. G. 2001, PASP, 113, 1420

Van Waerbeke, L., Benjamin, J., Erben, T., et al. 2013, MNRAS, 433, 3373

Venemans, B. P., Röttgering, H. J. A., Miley, G. K., et al. 2007, A&A, 461, 823

Viegas, S. M., & Friaca, A. C. S. 1995, MNRAS, 272, L35

Vreeswijk, P. M., Ellison, S. L., Ledoux, C., et al. 2004, A&A, 419, 927

Watson, D., Fynbo, J. P. U., Ledoux, C., et al. 2006, ApJ, 652, 1011

Weymann, R. J., Morris, S. L., Foltz, C. B., & Hewett, P. C. 1991, ApJ, 373, 23

Wolfe, A. M., Gawiser, E., & Prochaska, J. X. 2005, ARA&A, 43, 861

Wolfe, A. M., Turnshek, D. A., Smith, H. E., & Cohen, R. D. 1986, ApJS, 61, 249

Wolfire, M. G., McKee, C. F., Hollenbach, D., & Tielens, A. G. G. M. 2003, ApJ, 587, 278

Wylezalek, D., Galametz, A., Stern, D., et al. 2013, ApJ, 769, 79

York, D. G., Adelman, J., Anderson, Jr., J. E., et al. 2000, AJ, 120, 1579

Yoshida, M., Shimizu, Y., Sasaki, T., et al. 2000, in Proc. SPIE, Vol. 4009, Advanced Telescope and Instrumentation Control Software, ed. H. Lewis, 240–249

Zehavi, I., Zheng, Z., Weinberg, D. H., et al. 2011, ApJ, 736, 59

Zheng, Z.-Y., Wang, J.-X., Malhotra, S., et al. 2014, MNRAS, 439, 1101

Zheng, Z.-Y., Finkelstein, S. L., Finkelstein, K., et al. 2013, MNRAS, 431, 3589

ACKNOWLEDGMENTS

My heartfelt appreciation goes to my supervisor, Prof. Tohru Nagao, for great supports and instructions. Without his instruction and persistent support, I would not have been completed this dissertation. When I entranced into the Ph.D. course at Ehime University, I changed my study theme from the theoretical study of black hole to the observational study of the galaxy evolution. He guided me the ABC of the observational study. Thanks to his great supports, my first proposal for observations with the Subaru telescope had been accepted. I am pleased to complete this dissertation based on our first data obtained by our Subaru observations. I deeply appreciate Assistant Prof. Masatoshi Imanishi at National Astronomical Observatory of Japan (NAOJ). Even though he was in Hawaii, he gave many advises for our research through the teleconferences almost every weeks. Discussions with him made me being interested in the DLA. He instructed me many things about DLA studies and triggered me to start this dissertation work. I would like to thank Prof. Yoshiaki Taniguchi at the Open University of Japan, who is the previous director of Research Center for Space and Cosmic Evolution at Ehime University for his advices and discussions. Especially, I learned from him how to write scientific documents such as papers, proposals for observations, and so on. Associate Prof. Nobunari Kashikawa at NAOJ gave many advices for interpreting the results. In particular, when I stayed at Mitaka campus of NAOJ to work on the data analysis, he instructed me what I should check to resolve problems in the analyzing process. I would like to appreciate him deeply. When I had different time for the data analysis or writing the paper, Associate Prof. Masaru Kajisawa always guided me the accurate way to improve the situation. His kind instructions were so easy to understand. I am deeply grateful to him. I would like thank the dissertation referee committee, Prof. Tohru Nagao, Prof. Hisamitsu Awaki, and Associate Prof. Yoshiki Matsuoka for many useful comments and fruitful discussions to improve this dissertation. I appreciate Associate Prof. Masakazu Kobayashi at National Institute of Technology, Kure College, who is a previous post-doctoral researcher in our institute. He taught me various things about astronomical researches. Even after leaving our institute, they continue to support me, especially writhing papers and this dissertation support me, especially writing papers and this dissertation. Dr. Yoshiki Toba at Academia Sinica Institute of Astronomy and Astrophysics is also a previous post-doctoral researcher in our institute and instructed me many things about researches. Since he is so good at giving presentations, he is a good example for preparing presentations. I thank him so much. I also appreciate Dr. Yasuhiro Shioya who is former researcher in our institute. He gave me many instruction and advices for the basic of galaxy studies. In particular, he

gave me very useful templates of galaxy spectrum which I used many part of thesis works. His supports were invaluable. I would like to thank Associate Prof. Yoshiki Matsuoka. He moved to our institute from NAOJ in January 2017. Even for not so long period, he gives me insightful comments and suggestions. I thank Dr. Junichi Baba, Dr. Takuji Yamashita for discussions and advices. They give me various comments for my study through meetings of our groups. Dr. Kyoko Onishi helped me to prepare the presentation for the dissertation defense. She gave me many useful comments to improve my presentation. I appreciate her great supports. Dr. Ichi Tanaka at NAOJ and Dr. Ken Mawatari at Osaka Sangyo University gave many fruitful comments and suggestions. Based on their comments, we could improve our paper about absorber concentrated-regions. I really thank them. I also thank to the students in our institute for many discussions through seminars, meetings, and so on. Surrounded by many nice colleagues I could really enjoy the life in the institute.

This paper is based on observations with the Subaru Telescope operated by NAOJ. I thank the Subaru staffs, Dr. Tajitsu Akito and Dr. Michael Lemmen, for their support during the observations. For the data reduction and analysis, Dr. Fumiaki Nakata and Dr. Tsuyoshi Terai gave me great supports and advices. I am deeply graceful to them.

I was supported by grants from Japan Society for the Promotion of Science (JSPS) through the JSPS Research Fellowship for Young Scientists (16J02689), NAOJ Visiting Fellow Program supported by NAOJ, and the Hayakawa Satio awarded by the Astronomical Society of Japan. This dissertation is partly supported by JSPS KAKENHI (grant nos. 23244031, 25707010, 15K05030, 16H01101, 16H02166, and 16H03958) and by the JGCS Scholarship Foundation. I use the IRAF in the part of data reduction process. The IRAF is distributed by the National Optical Astronomy Observatories, operated by the Association of Universities of Research in Astronomy, Inc., under contract to the National Science Foundation of the United States.

Funding for SDSS-III has been provided by the Alfred P. Sloan Foundation, the Participating Institutions, the National Science Foundation, and the U.S. Department of Energy Office of Science. The SDSS-III web site is `http://www.sdss3.org/`. SDSS-III is managed by the Astrophysical Research Consortium for the Participating Institutions of the SDSS-III Collaboration including the University of Arizona, the Brazilian Participation Group, Brookhaven National Laboratory, Carnegie Mellon University, University of Florida, the French Participation Group, the German Participation Group, Harvard University, the Instituto de Astrofisica de Canarias, the Michigan State/Notre Dame/JINA Participation Group, Johns Hopkins University, Lawrence Berkeley National Laboratory, Max Planck Institute for Astrophysics, Max Planck Institute for Extraterrestrial Physics, New Mexico State University, New York University, Ohio State University, Pennsylvania State University, University of Portsmouth, Princeton University, the Spanish Participation Group, University of Tokyo, University of Utah, Vanderbilt University, University of Virginia, University of Washington, and Yale University.